

Diss. ETH No. 19256

**SOLAR THERMAL CRACKING OF  
NATURAL GAS - EXPERIMENTATION,  
MODELING, AND SCALE-UP**

A dissertation submitted to  
ETH ZURICH

for the degree of  
Doctor of Sciences

presented by  
GILLES MAAG  
Dipl. Masch.-Ing. ETH  
born September 16, 1981  
citizen of Herrliberg (ZH)

accepted on the recommendation of  
Prof. Dr. Aldo Steinfeld, examiner  
Dr. Gilles Flamant, co-examiner

2011







# Abstract

As an intermediate step towards sustainable energy systems, the solar thermal decarbonization of methane for co-producing hydrogen and carbon black is investigated. The calorific value of the initial reactant is upgraded, storing thus solar energy under chemical form. The produced carbon particles can be sequestered or used as material commodity under less severe CO<sub>2</sub> restraints.

A transient heat transfer model is developed for a reacting flow of CH<sub>4</sub> laden with carbon particles directly exposed to concentrated radiation (either solar or emitted by hot reactor walls), undergoing thermal decomposition into carbon and hydrogen. The unsteady mass and energy conservation equations, coupling convective heat and mass transfer, radiative heat transfer, and chemical kinetics for a two-phase solid-gas flow, are formulated and solved numerically for both phases by Monte Carlo and finite volume methods using the explicit Euler time integration scheme. A parametric study is performed with respect to the initial particle diameter, volume fraction, gas composition, and velocity. Smaller particles and/or high volume fractions increase the optical thickness of the medium, its radiative absorption and extinction coefficients, and lead to higher steady-state temperatures, reaction rates, and consequently, higher extents of chemical conversion.

An experimental investigation of the process was carried out using an improved version of a 5 kW particle-flow solar chemical reactor. It featured a continuous flow of CH<sub>4</sub> laden with μm-sized carbon particles, confined to a cavity receiver and directly exposed to concentrated radiation up to 1,720 suns. The reactor was tested both in a solar simulator and a solar furnace in the 1,100-1,600 K range. Its performance was examined for varying operational parameters, namely solar power input, seed particle

volume fraction and type, as well as gas volume flow rate and composition. Methane conversions and hydrogen yields exceeding 95 % were obtained at residence times of less than 2.0 s. A solar-to-chemical energy conversion efficiency of 16 % was experimentally reached, and a maximum value of 31 % was numerically predicted for a pure CH<sub>4</sub> flow. SEM images revealed the formation of filamentous agglomerations on the surface of the seed particles, reducing their active specific surface area.

To assess the performance of a commercial scale reactor, a complete reactor model is formulated by coupling radiation/convection/conduction heat transfer, including the above-mentioned numerical model, and chemical kinetics for the two-phase reacting flow within an array of tubular absorbers contained in a solar cavity-receiver. Experimental validation was accomplished by comparison with data obtained from a 10 kW prototype reactor tested in a solar furnace. Design optimization and performance analysis was carried out for a 10 MW commercial-scale reactor mounted on a solar tower system configuration. Complete chemical conversion is achieved for a maximum CH<sub>4</sub> mass flow rate of 0.75 kg s<sup>-1</sup> and a desired outlet temperature of 1,870 K, yielding a solar-to-chemical energy conversion efficiency of 42 %.

The same model is then applied to the steam-gasification process of carbonaceous material. Experimental validation, accomplished for biochar gasification with a 3 kW prototype reactor subjected to high-flux thermal irradiation, proved the versatility of the developed modeling approach. Application to the 10 MW industrial-scale reactor yielded a solar-to-chemical energy efficiency of 32 % for a desired output temperature of 1,500 K and an inlet concentration of 1,500 suns. It is shown that for an optimized reactor geometry a solar-to-chemical energy conversion of 37 % can be obtained under the same conditions.

The radiative heat transfer model for the cavity-receiver is used to study the influence of the window material on reactor performance by comparing quartz and sapphire. Due to its relatively high reflectance in the visible spectrum, the sapphire window requires higher solar inlet radiative flux than that for the quartz window to obtain the same reactor temperature and energy efficiency.

This thesis contributes to the development of the solar reactor technol-

ogy for producing clean, sustainable fuels.





# Sintesi

Quale passo intermedio verso un sistema energetico sostenibile, è investigato il processo termosolare di decarbonizzazione del metano per la coproduzione di idrogeno e nero di carbone. Il contenuto calorifico del reagente è aumentato, immagazzinando quindi energia solare sotto forma chimica. Il particolato carbonioso prodotto può essere sequestrato oppure utilizzato come merce industriale sotto restrizioni meno severe per ciò che riguarda il CO<sub>2</sub>.

Un modello transiente di trasmissione calorica è stato sviluppato per un flusso reagente di CH<sub>4</sub> carico di particelle carboniose, direttamente esposto a radiazione concentrata (sia solare sia emessa dalla parete calda di un reattore), in decomposizione termica in carbone ed idrogeno. Le equazioni non-stazionarie di conservazione di massa e di energia, che uniscono trasporto convettivo di massa e calore, trasferimento radiativo e cinetica chimica, per un flusso solido-gas a due fasi, sono formulate e risolte numericamente per entrambe le fasi con i metodi Monte Carlo e dei Volumi Finiti, utilizzando il metodo di Eulero esplicito per l'integrazione in funzione del tempo. Uno studio di parametri è svolto riguardo al diametro iniziale delle particelle, la loro frazione volumetrica, la composizione iniziale del gas e la sua velocità. Particelle di diametro minore e/o frazioni volumetriche alte aumentano la densità ottica del mezzo, i suoi coefficienti di assorbimento e di estinzione radiativi e portano a temperature, velocità di reazione e, di conseguenza, conversioni chimiche più alte.

Un'investigazione sperimentale del processo è stata eseguita utilizzando una versione perfezionata di un reattore solarchimico a flusso di particolato da 5 kW che presenta un flusso continuo di CH<sub>4</sub> carico di particolato carbonioso di dimensioni micrometriche, confinato entro un ricevitore a cavità ed esposto direttamente ad un flusso concentrato di radiazione solare di

intensità fino a 1'720 soli. Il reattore è stato collaudato sia in un simulatore solare sia in una fornace solare a temperature tra i 1'100 ed i 1'600 K. Il suo rendimento è stato esaminato per parametri di operazione variabili quali la potenza solare introdotta, la frazione volumetrica ed il tipo di particolato iniettati oltre che la portata volumetrica e la composizione del gas. Conversioni di metano e rese di idrogeno superiori a 95 % sono state ottenute con tempi di residenza inferiori ai 2 s. Un rendimento energetico solare-chimico di 16 % è stato raggiunto sperimentalmente ed un valore massimo di 31 % prognosticato tramite una simulazione numerica per un flusso puro di CH<sub>4</sub>. Immagini di microscopia elettronica a scansione hanno rivelato la formazione di agglomerazioni filamentose sulla superficie del particolato iniettato ed una riduzione della sua superficie specifica attiva è stata constatata.

Per valutare il rendimento di un reattore in scala commerciale, un modello completo è formulato unendo trasferimento radiativo/convettivo/conduztivo, includendo il modello numerico sopraccitato, con la cinetica chimica per il flusso reagente a due fasi confinato in un sistema di assorbitori tubulari contenuti in un ricevitore solare a cavità. La validazione sperimentale è stata compiuta comparando i dati ottenuti con quelli registrati collaudando un prototipo di reattore da 10 kW in una fornace solare. L'ottimizzazione della costruzione e l'analisi del rendimento sono state eseguite per un reattore in scala commerciale da 10 MW montato su un sistema di concentrazione solare a torre. Conversione chimica completa è osservata per una portata massica di CH<sub>4</sub> massimale di 0.75 kg s<sup>-1</sup> ed una temperatura d'uscita desiderata di 1'870 K, risultando in un' efficienza di conversione energetica da solare a chimica del 42 %.

Lo stesso modello è in seguito applicato al processo di gassificazione con vapore di materiale carbonioso. La validazione sperimentale, compiuta per la gassificazione di carbone vegetale impiegando un prototipo di reattore da 3 kW soggetto ad irradiazione termica altamente concentrata, ha dimostrato la versatilità dell' approccio di modellatura sviluppato. Applicandolo ad un reattore in scala commerciale da 10 MW è stato calcolato un rendimento energetico solare-chimico del 32 % per una temperatura d'uscita desiderata di 1'500 K ed una concentrazione d'ingresso di 1'500 soli. E' mostrato che per una geometria del reattore ottimizzata è possibile

ottenere un rendimento solare-chimico del 37 % sotto le stesse condizioni.

Il modello di trasferimento radiativo per il ricevitore a cavità è inoltre utilizzato per studiare l'influsso del materiale della finestra sul rendimento del reattore, confrontando i due materiali quarzo e zaffiro. A causa della sua riflettanza più alta nello spettro visibile, la finestra di zaffiro richiede un flusso radiativo d'ingresso maggiore che quella di quarzo per ottenere uguale temperatura all'interno del reattore e rendimento energetico.

Questa tesi contribuisce allo sviluppo della tecnologia di reattori solari per la produzione di combustibili puliti e sostenibili.



# Acknowledgements

First of all I thank Prof. Aldo Steinfeld for giving me the opportunity to work in such a fascinating and challenging research field, for supervising my doctoral studies at the Professorship of Renewable Energy Carriers of ETH Zurich, and his support in my research activities. I thank Dr. Gilles Flamant for his helpful advice on my work, the critical review of this manuscript, and for acting as co-examiner. Particular thanks also go to Prof. Wojciech Lipiński for his advice and support during the writing of the basic simulation tool my entire thesis relies on.

The work presented in this thesis being one part of a joint effort of several research groups in the framework of the EU-funded SOLHYCARB project, it was dependent on many contributions by other participants. In particular I am indebted to Dr. Sylvain Rodat and Dr. Stéphane Abanades who carried out the experimental testing of the 10 and the 50 kW reactor prototypes at CNRS-PROMES collecting the experimental data I was able to validate my simulations with, Michael Wullenkord from DLR who provided the chemical kinetics of the reaction, Dr. Akiba Segal from WIS who designed the commercial-scale solar concentrating field. Moreover, I want to thank Dr. Giorgos Patrianakos and Dr. Cyril Caliot for interesting discussions and helpful suggestions regarding my numerical work.

Further, I thank all my present and former colleagues and members of the PRE group, Prof. Jörg Petrasch and Dr. Andreas Z'Graggen, for helpful advice on my modeling task, Dr. Peter Loutzenhiser, for his help during the experimental campaigns at PSI, Philipp Haueter, for the improved design of the SynMet reactor and his help during the experimental campaigns at ETH, Dr. Patrick Coray, Dr. Elena Gálvez, Dr. Sophia Haussener, Dr. Tom Melchior, Dr. Viktoria Nikulshyna, Dr. Nic Pi-  
atkowski, Dr. Matt Roesle, Dr. Lothar Schunk, Dr. Dominic Trommer,

Dr. Peter von Zedtwitz, Dr. Hyung Chul Yoon, Roman Bader, Christoph Gebald, Enrico Guglielmini, Ilias Hischer, Laurenz Schlumpf, Anastasia Stamatiou, Clemens Suter, Willy Villasmil, Jan Wurzbacher, and Emilie Zermatten, for providing an inspiring work environment. Thanks also go to our secretary Tina Daum for the administrative work.

During the two experimental campaigns carried out at the PSI solar furnace I could rely on the competent help of the Solar Technology Laboratory deputy head, Dr. Anton Meier, and staff members Kevin Cuche, Benjamin Jäggi, Peter Schaller, Samuel Wepf, and Daniel Wuillemin who ensured the smooth operation of the facility and the reactor, and assisted me during the experimental runs. My gratitude also goes to Dr. Francisco Javier Gutiérrez for his help during the experimental campaign and the characterization of the carbonaceous products, and Alwin Frei for the SEM images and his great helpfulness in keeping our gas analysis equipment working without problems.

Also, I want to thank my former bachelor and master students Henrik Wallimann and Dave Dunnett, for their simulation work, Claudio Forrer, Marco Zanini, Dominic Brunner, Marc Brühlhart, and Giw Zanganeh, for their experimental work at ETH or PSI.

Finally, the most special thanks go to my family: my sister Marie-Louise, my brother Philippe, and in particular to my parents Anita and Werner. The effort they put into transmitting me their high esteem for values such as education, knowledge, and culture, as well as their support during my studies were of fundamental importance for both my personal and academic growth.

# Contents

<b>Abstract</b>	<b>i</b>
<b>Sintesi</b>	<b>v</b>
<b>Acknowledgements</b>	<b>ix</b>
<b>Nomenclature</b>	<b>xv</b>
<b>1 Introduction</b>	<b>1</b>
1.1 Solar thermal cracking of natural gas . . . . .	1
1.2 Thesis outline . . . . .	3
<b>2 Radiation heat transfer model</b>	<b>5</b>
2.1 Introduction . . . . .	5
2.2 Problem statement . . . . .	6
2.3 Radiative heat transfer analysis . . . . .	8
2.4 Conservation equations . . . . .	10
2.4.1 Mass conservation . . . . .	10
2.4.2 Energy conservation . . . . .	11
2.5 Numerical results . . . . .	12
2.6 Summary . . . . .	20
<b>3 Experimental work</b>	<b>21</b>
3.1 Introduction . . . . .	21
3.2 Solar reactor configuration . . . . .	22
3.3 Experimental setup . . . . .	23
3.4 Experimental results . . . . .	27
3.4.1 Solar simulator . . . . .	27

---

3.4.2	Solar furnace . . . . .	31
3.5	Product characterization . . . . .	43
3.5.1	Active carbon . . . . .	43
3.5.2	Carbon black . . . . .	44
3.6	Summary . . . . .	45
<b>4</b>	<b>Scale-up reactor model</b>	<b>49</b>
4.1	Introduction . . . . .	49
4.2	Problem statement . . . . .	50
4.3	Heat transfer modeling . . . . .	50
4.3.1	Cavity receiver . . . . .	53
4.3.2	Absorber tubes . . . . .	54
4.4	Experimental validation . . . . .	58
4.5	Scale-up to 10 MW <sub>th</sub> . . . . .	60
4.6	Summary . . . . .	64
<b>5</b>	<b>Biochar gasification</b>	<b>69</b>
5.1	Introduction . . . . .	69
5.2	Problem statement . . . . .	72
5.3	Experimental validation . . . . .	76
5.4	Scale-up to 10 MW solar power input . . . . .	78
5.5	Summary . . . . .	80
<b>6</b>	<b>Conclusion</b>	<b>87</b>
6.1	Experimental work . . . . .	88
6.2	Modeling . . . . .	89
6.3	Outlook . . . . .	90
<b>A</b>	<b>Temperature of a quartz/sapphire window</b>	<b>93</b>
A.1	Introduction . . . . .	93
A.2	Analysis . . . . .	94
A.3	Results . . . . .	97
A.4	Summary . . . . .	100
<b>B</b>	<b>Optical properties of utilized materials</b>	<b>103</b>
B.1	Surfaces . . . . .	103



---

B.2 Gas . . . . .	103
<b>C Thermochemical properties of utilized materials</b>	<b>111</b>
C.1 Specific heat . . . . .	111
C.2 Specific enthalpy . . . . .	112
C.3 Thermal conductivity and viscosity . . . . .	112
<b>D Chemical reaction model</b>	<b>115</b>
<b>E Scale-up reactor design</b>	<b>117</b>
E.1 Introduction . . . . .	117
E.2 Heliostat field . . . . .	117
E.3 Reactor geometry . . . . .	119
E.3.1 Absorber tube diameter . . . . .	119
E.3.2 Reactor height . . . . .	119
E.3.3 Aperture design . . . . .	119
E.3.4 Single or multiple cavity . . . . .	120
E.3.5 Cavity width and number of absorber tubes . . . . .	121
E.4 Reactor performance . . . . .	121
E.5 Conclusions . . . . .	124
<b>Curriculum vitae</b>	<b>151</b>



# Nomenclature

## Latin characters

$A$	area, $\text{m}^2$
$A$	absorbed cumulative fraction of incident radiation
$Bi$	Biot number
$a$	polynomial coefficient, $\text{W m}^{-2} \text{K}^{-4}$
$b$	polynomial coefficient, $\text{W m}^{-2} \text{K}^{-4}$
$C$	solar concentration ratio
$c$	polynomial coefficient, $\text{W m}^{-2} \text{K}^{-4}$
$\bar{c}_p$	specific heat at constant pressure, $\text{J mol}^{-1} \text{K}^{-1}$
$\bar{c}_v$	specific heat at constant volume, $\text{J mol}^{-1} \text{K}^{-1}$
$D$	depth, $\text{m}$
$d$	diameter
$E$	emittance
$E$	efficiency factor
$E_a$	activation energy, $\text{J mol}^{-1}$
$e_\lambda$	Planck's spectral emissive power distribution, $\text{W m}^{-3}$
$F_d$	cumulative particle number distribution
$f$	particle number density, $\text{m}^{-4}$
$f_d$	particle number distribution probability density, $\text{m}^{-1}$
$f_V$	particle volume fraction
$g$	standard gravity ( $g = 9.81 \text{ m s}^{-2}$ )
$H$	height, $\text{m}$
$\bar{h}$	specific enthalpy, $\text{J mol}^{-1}$
$\Delta\bar{h}_R$	reaction enthalpy change, $\text{J mol}^{-1}$
$I$	direct solar irradiation, $\text{W m}^{-2}$
$I_\lambda$	spectral radiation intensity, $\text{W m}^{-3} \text{sr}^{-1}$

---

$k$	thermal conductivity, $\text{W m}^{-1} \text{K}^{-1}$
$k_0$	pre-exponential factor, $\text{s}^{-1}$
$k_B$	Boltzmann constant ( $k_B = 1.3807 \cdot 10^{-23} \text{ m}^2 \text{ kg s}^{-2} \text{ K}^{-1}$ )
$\hat{\mathbf{k}}$	unit vector of the $z$ -Cartesian coordinate
$L$	length, slab thickness, m
$m$	reaction order
$m_a$	atomic mass, kg
$\dot{m}$	mass flow rate, $\text{kg s}^{-1}$
$\bar{m}$	molar mass, $\text{kg mol}^{-1}$
$N$	number
$N_A$	Avogadro's number ( $N_A = 6.022 \cdot 10^{23} \text{ mol}^{-1}$ )
$n$	amount of substance, mol
$\dot{n}$	molar flow rate, $\text{mol s}^{-1}$
$\dot{n}''$	molar flux, $\text{mol s}^{-1} \text{ m}^{-2}$
$\bar{n}$	complex refractive index, $\bar{n} = n - ik$
Nu	Nusselt number
Pr	Prandtl number
$p$	pressure, Pa
$Q$	power, W
$q$	heat flux, $\text{W m}^{-2}$
$R$	reflectance
$\bar{R}$	universal gas constant ( $\bar{R} = 8.314 \text{ J mol}^{-1} \text{ K}^{-1}$ )
Ra	Rayleigh number
Re	Reynolds number
$r$	radius; cylindrical coordinate, m
$\mathbf{r}$	position vector, m
$\bar{r}$	reaction rate, $\text{mol m}^{-3} \text{ s}^{-1}$
$S_\lambda$	spectral radiation source function, $\text{W m}^{-3} \text{ sr}^{-1}$
$\mathbf{s}$	direction vector, m
$\hat{\mathbf{s}}$	unit vector into a given direction
$T$	temperature, K
$t$	time, s
$(UA)$	overall heat conductivity, $\text{W K}^{-1}$
$V$	volume, $\text{m}^3$
$V$	transmittance

$V_d$	cumulative particle volume distribution
$\dot{V}$	volume flow rate, $\text{m}^3 \text{s}^{-1}$
$v_d$	particle volume distribution probability density, $\text{m}^{-1}$
$W$	width, m
$w$	flow velocity in $z$ -direction, $\text{m s}^{-1}$
$X_C$	carbon conversion
$X_{\text{CH}_4}$	methane conversion
$\bar{x}$	mole fraction
$Y_{\text{H}_2}$	hydrogen yield
$z$	Cartesian/cylindrical coordinate, m

### Greek characters

$\alpha$	convective heat transfer coefficient, $\text{W m}^{-2} \text{K}^{-1}$
$\alpha$	thermal diffusivity, $\text{W m}^{-2} \text{K}^{-1}$
$\beta$	extinction coefficient, $\text{m}^{-1}$
$\beta$	gas expansion coefficient, $\text{K}^{-1}$
$\Gamma_p$	number of particles per unit volume, $\text{m}^{-3}$
$\dot{\gamma}_p$	particle number flux, $\text{m}^{-2} \text{s}^{-1}$
$\delta$	Kronecker delta function
$\epsilon$	emissivity
$\eta$	energy efficiency
$\eta$	wavenumber, $\text{m}^{-1}$
$\theta$	scattering angle, $^\circ$
$\kappa$	absorption coefficient, $\text{m}^{-1}$
$\lambda$	wavelength, m
$\mu$	dynamic viscosity, $\text{kg m}^{-1} \text{s}^{-1}$
$\nu$	stoichiometric coefficient
$\nu$	kinematic viscosity, $\text{m}^2 \text{s}^{-1}$
$\xi$	particle size parameter
$\rho$	density, $\text{kg m}^{-3}$
$\bar{\rho}$	molar concentration, $\text{mol m}^{-3}$
$\sigma$	Stefan-Boltzmann constant ( $\sigma = 5.6704 \cdot 10^{-8} \text{ W m}^2 \text{K}^{-4}$ )
$\sigma_{\text{sca}}$	scattering coefficient, $\text{m}^{-1}$
$\varsigma$	collision diameter, m

---

$\tau$	residence time
$\Phi$	scattering phase function
$\psi$	shutter beam transmission
$\Omega$	solid angle, sr

### Symbols

$\nabla$	Nabla operator
$\mathcal{R}$	random number from an uniform distribution (0,1)

### Subscripts/Superscripts

0	initial; initial/inlet
32	Sauter-mean
abs	absorption
b	blackbody
c	cavity
e	external source of radiation
el	electrical
exp	experimental
f	formation
g	gas phase
h	hydrodynamic
i	inner
in	inlet
inc	incoming
N	at normal conditions ( $T_N = 273.15$ K, $p_N = 101,325$ Pa)
out	outlet
p	particles; solid phase
r	radiative
ray	generic ray in MC
ref	reference
surr	surroundings
th	thermal

---

w	window
$\lambda$	spectral
$\tilde{\nu}$	spectral
$\infty$	ambient

## Abbreviations

AC	active carbon
BET	Brunauer-Emmett-Teller
CB	carbon black
CNRS	Centre National de la Recherche Scientifique (French National Center for Scientific Research)
CPC	compound parabolic concentrator
DLR	Deutsches Zentrum für Luft- und Raumfahrt (German Aerospace Center), Cologne, Germany
ETH	Eidgenössische Technische Hochschule (Swiss Federal Institute of Technology), Zurich, Switzerland
EU	European Union
GC	gas chromatography/chromatograph
IR	infrared
MC	Monte Carlo method
NG	natural gas
PROMES	Laboratoire Procédés, Matériaux et Energie Solaire (Laboratory of Processes, Materials and Solar Energy), Odeillo - Font-Romeu, France
PSI	Paul Scherrer Institute, Villigen, Switzerland
SEM	scanning electron micrograph
TC	thermocouple
WIS	Weizmann Institute of Science, Rehovot, Israel





# Chapter 1

## Introduction

### 1.1 Solar thermal cracking of natural gas

The prosperity of modern human society relies strongly on the availability of energy in easily storable and recallable forms, in order to perform the necessary tasks, such as the production and transportation of economical goods, the provision of services, and personal mobility. This demand, currently at ca. 16 TW (value for 2007), is expected to increase by 40 % until 2030 [59], due to world population growth and advancing industrialization of emerging markets. Presently, ca. 85 % of global primary energy demand is satisfied through fossil (hydrocarbonaceous) energy carriers [21], whose combustion leads to the emission of pollutants and of the greenhouse gas CO<sub>2</sub>, the excessive presence of which in the atmosphere is deemed to exert a negative influence on the health and the quality of life of the population as well as on the environment [63]. Secondly, since the rate of consumption of fossil fuels highly exceeds their formation rate, the global resources of coal, oil, and gas will inescapably continue shrinking. These facts require the substitution of fossil fuels with primary energy sources of smaller environmental impact and higher availability.

Solar energy, being virtually unlimited, freely available, and free of the above-mentioned negative ecological implications, presents itself as an attractive replacement for fossil sources. Its drawbacks: high dilution, intermittency, and unequal distribution over the globe require however to be overcome by concentrating the incoming solar radiation and transforming its energy into an easily storable and transportable form, in order to enable it to compete with traditional energy sources for covering any remarkable

share of global energy consumption [149].

An interesting and auspicious way of increasing the energy density, storability, and transportability solar energy is its conversion in chemical form stored in energy carriers (solar fuels), such as hydrogen, produced in high-temperature thermochemical processes driven by concentrated solar radiation [43]. Such processes comprise production of  $H_2$  from  $H_2O$  splitting, by applying two-step thermochemical cycles based on metal/metal oxide redox reactions such as Zn/ZnO [138] or ceria [25]. However, the complete replacement of fossil fuels with solar ones remains a long-term goal since the required technologies are not estimated to be ready for commercial applications in short-mid time terms.

A promising intermediate route for production of solar fuels is represented by hybrid solar-fossil thermochemical processes making use of concentrated solar radiation as the energy source of high-temperature process [43, 66, 139]. Industrially relevant examples include the thermal gasification of carbonaceous materials [78, 90, 152], the thermal cracking of natural gas [2, 4, 53], the thermal reforming of natural gas [31, 68, 159], and the carbothermal reduction of metal oxides [48, 140], for producing synthetic fluid fuels with upgraded calorific value. These hybrid solar-driven processes offer viable and efficient routes for fossil fuel decarbonization and  $CO_2$  avoidance, and further create a transition path towards solar hydrogen.

The focus of this thesis lies on thermal cracking of natural gas (NG) which has been in past applied for the production of carbon-rich hydrocarbons and carbon black [9, 57, 156]. More recent studies have considered this process for  $H_2$  production as an alternative route to steam-reforming [12, 34, 44, 45, 102, 107, 112, 136], using metallic [8, 27, 39, 70, 76, 97, 104, 111, 128, 142, 150, 167] or carbonaceous catalysts [10, 13, 37, 38, 64, 75, 77, 89, 96, 101, 127], as well as autocatalysis [119]. If the process heat required ( $170 \text{ kJ mol}(\text{CH}_4)$ ) for heating up to 1,500 K and driving the chemical reaction [148]) is delivered by a renewable energy source, in this case solar energy, the process can be realized free of combustion byproducts. Carbon produced can either be sequestered or used as a material commodity or metallurgical reducing agent under less severe  $CO_2$  restraints. If it is sequestered, no  $CO_2$  emission will result from the complete process chain

to electricity generation.

Solar reactor concepts proposed for this process include directly-irradiated solar reactors with reactants directly exposed to the concentrated solar irradiation [55, 69, 88] -, and indirectly-irradiated solar reactors - with graphite/ceramic tubes or other opaque surfaces serving as absorbers and heat conductors [3, 4, 29, 30, 115, 116]. Solar cavity-receivers containing one or more absorber tubes through which the reactants flow have been applied for the previously mentioned thermochemical processes: reduction of metal oxides [92], steam-gasification of carbonaceous materials [91], and steam reforming of methane [81]. In particular, radiative heat transfer has been analyzed for this type of configuration [93, 116].

## 1.2 Thesis outline

This thesis was carried out in the framework of the SOLHYCARB EU-Project, funded by the European Commission under contract No. SESCT 2006-19770. Final goal of the project was the development and testing of solar reactor prototypes of size up to 50 kW, the development and validation of a numerical model able to predict the performance of a commercial-scale (10 MW<sub>th</sub>) scale-up reactor in order to assess the economical feasibility of the process. A previous PhD thesis, carried out by D. Hirsch [52], comprising a thermodynamical analysis of the process, experimental campaigns, and a radiative heat transfer model, served as starting point for the work presented herein.

The first part of this thesis (Chap. 2) focuses on the development of a transient radiation-convection numerical heat transfer model for a reactive two-phase system composed of a CH<sub>4</sub> flow laden with C particles, whose thermal and optical properties vary as the decomposition reaction progresses. It is then applied to study the behavior of the two-phase medium when subjected to high-flux thermal radiation.

Chapter 3 presents the results obtained from experimental testing of an improved reactor prototype that evolved from the previous design [55], aimed to elucidate the effect of the operational parameters, namely solar inlet power, seed particle volume fraction, total gas volume flow, and CH<sub>4</sub>

concentration on the reactor's thermal performance.

A numerical model is formulated in Chap. 4 to simulate the behavior of an indirectly-irradiated solar reactor consisting of a receiver cavity, containing an array of absorber tubes through which the reacting medium flows. The model couples radiative transfer into and within the cavity-receiver to heat transfer, fluid flow, and chemical kinetics inside the absorber tubes, applying the radiation heat transfer model presented in Chap. 2. Experimental validation is accomplished with a testing data of a 10 kW reactor prototype, obtained at the 1 MW solar furnace of PROMES-CNRS [116]. The reactor model is then used to optimize the design for maximum energy conversion efficiency, and to simulate the performance of a 10 MW commercial-scale reactor for a solar tower system.

To give an additional proof of the validity of the numerical model, and to illustrate its versatility for different solar chemical processes, it is applied, in Chap. 5, to steam-gasification of carbonaceous materials. Validation is done with experimental data obtained at ETH's high-flux solar simulator [91], and the model is used to predict the performance of the process when run on the 10 MW commercial-scale reactor presented in the previous chapter.

Chapter 6 gives a summary of the conducted work and addresses challenges: either encountered during the work presented herein, or potential future ones, providing suggestions for possible improvements.

Finally, Appx. A presents an application of the radiative heat transfer model for the cavity-receiver used in Chaps. 4 and 5 to predict the temperature of the window of a directly-irradiated solar cavity reactor. Two different window materials, quartz and sapphire, are compared for the effect of their optical properties on their own and the cavity's temperatures, as well as on the energy efficiency performance of the reactor. Additional appendix chapters are provided to explain more detailedly procedures and literature data used, as well as to include unpublished contributions to this thesis from other sources.

# Chapter 2

## Radiation heat transfer model<sup>1</sup>

### 2.1 Introduction

Chemical reactors based on the concept of direct irradiation require matching the rate of radiative heat transfer to the rate of the chemical reaction. Modeling such an interaction is needed for anticipating the consequences of a given design decision on the reactor's performance, and for optimizing the reactor design for maximum solar-to-chemical energy conversion efficiency.

Previous pertinent studies of transient radiative heat transfer in solar-driven solid-gas reactions include models for suspensions of coal particles undergoing steam gasification [84, 85], packed beds of  $\text{CaCO}_3$  particles undergoing thermal decomposition [83], and of  $\text{ZnO}$  particles undergoing thermal and carbothermal reduction [98, 36, 106]. Steady-state radiative transfer analysis of solar reactions was applied for the thermal decomposition of  $\text{CH}_4$  [54], solar combined  $\text{CH}_4$ -reforming and  $\text{ZnO}$ -reduction [72], gasification of coal [151, 15] and petroleum coke [166]. Examples of analyses of non-solar reactors involving heterogeneous chemical systems include coal gasification in packed beds [16], fluidized beds [120], and entrained gasifiers [154], combustion in porous burners [94, 145], and biomass pyrolysis [33]. Further examples of radiative heat transfer analyses include studies on direct absorption of concentrated solar radiation by particle suspensions [5, 40, 65]. In this chapter, a transient radiation-convection heat transfer

---

<sup>1</sup>Material from this chapter has been published in: G. Maag, W. Lipiński, and A. Steinfeld. Particle-gas reacting flow under concentrated solar irradiation. *Int. J. Heat Mass Transfer*, 52:4997-5004, 2009.

model is developed for a reactive two-phase system composed of a  $\text{CH}_4$  flow laden with C particles, whose thermal and optical properties vary as the decomposition reaction progresses. Temperatures and gas composition are computed for boundary and initial conditions (initial/inlet particle diameter, particle volume fraction, gas phase composition, inlet gas velocity, and incident solar radiative flux) anticipated for a solar reactor. Emphasis is placed on the detailed investigation of the wavelength and directional depended radiative exchange within the particle suspension.

## 2.2 Problem statement

The two-phase system domain is depicted schematically in Fig. 2.1. It consists of a 1D slab containing  $\mu$ -sized C particles suspended in a  $\text{CH}_4$ - $\text{H}_2$ -Ar gas mixture. The gas-particle flow is directly exposed to an external source of concentrated solar radiation, assumed to have Planck's spectral distribution of a blackbody at 5,780 K. Each phase is modeled as a non-uniform and non-gray absorbing-emitting-scattering medium. The boundaries are modeled as black plane walls at  $T_{\text{surr}} = 0$  K (non-participating surroundings). The composition of each phase and its thermal and optical properties vary with time due to the heterogeneous endothermic reaction occurring at above about 1,500 K.

Each particle is assumed isothermal, as justified by the Biot number  $\text{Bi} \ll 1$  for the considered size range of the particles. For an opaque particle at temperature  $T_p$  suspended in gas flow at  $T_g < T_p$ , surrounded by cold walls and irradiated by an external flux  $q_e$ , Bi is here defined as the ratio of the internal conduction heat transfer resistance to the external radiation-convection heat transfer resistance,

$$\text{Bi}_r = \frac{d_p \left\{ \varepsilon \left[ \frac{q_e}{T_p - T_g} - \sigma (T_p + T_g) (T_p^2 + T_g^2) \right] - \alpha \right\}}{k_c}. \quad (2.1)$$

Each phase is modeled as a quasi-continuous medium using its effective volumetric transport properties [7, 62]. The C particles are modeled as absorbing, emitting, and anisotropically scattering, while scattering is neglected for the gas phase. The flow is assumed to be laminar in the direction perpendicular to the boundaries. Radiative and convective heat is

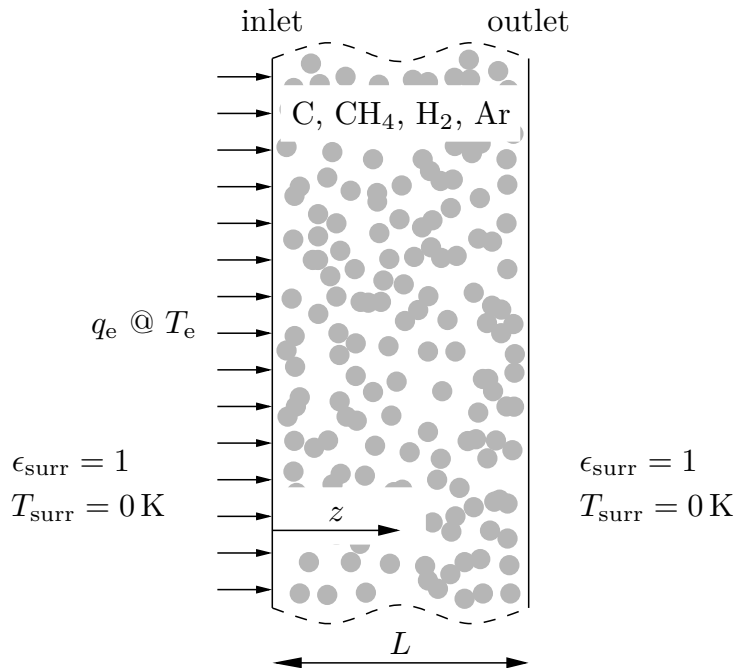
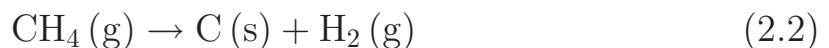


Figure 2.1: Scheme of the 1D system domain consisting of a particle-gas mixture exposed to an external source of concentrated solar radiation and undergoing heterogeneous thermochemical reaction.

exchanged between particles and gas. Mass and heat diffusion are omitted from consideration, thus significantly simplifying the flow analysis [108]. The kinetics of  $\text{CH}_4$ -decomposition,



was previously modeled for non-solar [64, 100] and solar-driven [114, 148] reactors. In this study, a simplified first-order Arrhenius type rate law was applied for a flow of  $\text{CH}_4$  laden with  $\mu$ -sized carbon particles, given by:

$$\bar{r} = \bar{\rho}_{\text{C,exp}}^{-1} k_0 \exp\left(\frac{E_a}{RT}\right) \bar{\rho}_{\text{CH}_4} \quad (2.3)$$

where  $k_0 = 1.07 \cdot 10^6 \text{ s}^{-1}$ ,  $\bar{\rho}_{\text{C,exp}} = 8.84 \text{ mol m}^{-3}$ , and  $E_a = 147 \text{ kJ mol}^{-1}$  were determined experimentally in a solar reactor prototype tested under concentrated solar irradiation [148]. This simplified rate law can reasonably describe the reaction rate for the  $\text{CH}_4$ -particle flow conditions existing in the solar reactor (Fig. 3.1), but may not be applied to the catalytic decomposition reaction using other catalysts or to reactors with different

mass/heat transfer characteristics. The carbon produced is assumed to deposit on the surface of existing laden particles, resulting in their growth with time and affecting their radiative characteristics. It is assumed that the particle growth does not affect the reaction rate.

### 2.3 Radiative heat transfer analysis

Variation of the radiative intensity  $I_\lambda(\mathbf{r}, \mathbf{s})$  along path  $\hat{\mathbf{s}}$  in a two-phase medium, where the phases are at thermal non-equilibrium to each other, is described by the equation of radiative transfer in its extended form [7, 95],

$$\hat{\mathbf{s}} \cdot \nabla I_\lambda(z, \hat{\mathbf{s}}) = S_\lambda(z, \hat{\mathbf{s}}) - [\beta_{\lambda,p}(z, \hat{\mathbf{s}}) + (1 - f_V) \kappa_{\lambda,g}(z, \hat{\mathbf{s}})] I_\lambda(z, \hat{\mathbf{s}}), \quad (2.4)$$

where  $S_\lambda(z, \hat{\mathbf{s}})$  is the radiative source function,

$$S_\lambda(z, \hat{\mathbf{s}}) = \kappa_{\lambda,p}(z) I_{b,\lambda}[T_p(z)] + (1 - f_V) \kappa_{\lambda,g}(z) I_{b,\lambda}[T_g(z)] + \frac{\sigma_{\text{sca},\lambda,p}(z)}{4\pi} \int_{4\pi} I_\lambda(z, \hat{\mathbf{s}}_{\text{inc}}) \Phi_{\lambda,p}(z, \hat{\mathbf{s}}_{\text{inc}}, \hat{\mathbf{s}}) d\Omega_{\text{inc}}, \quad (2.5)$$

and  $\beta_{\lambda,p}$ ,  $\kappa_{\lambda,p}$ ,  $\sigma_{\text{sca},\lambda,p}$  are the spectral extinction, absorption, and scattering coefficients of the solid phase, respectively,  $\kappa_{\lambda,g}$  is the spectral absorption coefficient of the gas phase, and  $\Phi_{\lambda,p}(\hat{\mathbf{s}}_i, \hat{\mathbf{s}})$  is the scattering phase function of the solid phase from  $\hat{\mathbf{s}}_i$  into  $\hat{\mathbf{s}}$ . The corresponding boundary conditions for (2.4) are

- for collimated incident solar flux at  $z = 0$ ,

$$I_\lambda(z = 0, \hat{\mathbf{s}}) = \frac{q_e}{\sigma T_e^4} \pi I_{b,\lambda}(T_p) \delta(\hat{\mathbf{s}} - \hat{\mathbf{k}}) \quad \text{for } \hat{\mathbf{s}} \cdot \hat{\mathbf{k}} > 0, \quad (2.6)$$

- for diffuse incident solar flux at  $z = 0$ ,

$$I_\lambda(z = 0, \hat{\mathbf{s}}) = \frac{q_e}{\sigma T_e^4} \pi I_{b,\lambda}(T_e) \quad \text{for } \hat{\mathbf{s}} \cdot \hat{\mathbf{k}} > 0, \quad (2.7)$$

- for the boundary at  $z = L$ ,

$$I_\lambda(z = L, \hat{\mathbf{s}}) = 0 \quad \text{for } \hat{\mathbf{s}} \cdot \hat{\mathbf{k}} < 0. \quad (2.8)$$



Radiative properties of C particles are calculated by assuming independent scattering and the refractive index of the gas phase to be equal to unity [144]. The absorption and scattering coefficients are computed by using the monodisperse approximation [35, 95],

$$\begin{aligned} \{\kappa_{\lambda,p}, \sigma_{\text{sca},\lambda,p}, \beta_{\lambda,p}\} &= \pi \int_0^{\infty} \{E_{\text{abs},\lambda,p}, E_{\text{sca},\lambda,p}, E_{\text{ext},\lambda,p}\} r^2 f(r) dr \\ &\approx \frac{3f_V}{2d_{32}} \{E_{\text{abs},\lambda,p}, E_{\text{sca},\lambda,p}, E_{\text{ext},\lambda,p}\}. \end{aligned} \quad (2.9)$$

In Eq. (2.9),  $f(d) dd_p$  is the number of spherical particles of diameter between  $d_p$  and  $d_p + dd_p$  per unit volume and  $d_{32}$  is the Sauter mean particle diameter [35]. The absorption, scattering, and extinction efficiency factors and the scattering phase function are obtained by applying the Mie theory [19], based on the particle size parameter  $\xi = \pi d/\lambda$  in the range  $10^{-2}$ - $10^2$  and the complex refractive index of the particle  $\bar{n} = n - ik$  approximated by that of propane soot [20, 32]. The absorption coefficient of the gas phase  $\kappa_{\lambda,g}$  is computed by applying the line-by-line model to the molecular spectroscopic database HITRAN-2004 for  $\text{CH}_4$  [122, 123, 143], to calculate the high-resolution ( $\Delta\eta = \Delta\lambda/\lambda^2 = 9.9\text{m}^{-1}$ ) spectral absorption coefficient  $\kappa_{\lambda,g}^*$  in the wavelength range  $10^{-7}$ - $10^{-5}$  m, which in turn is used to calculate the low-resolution absorption coefficient of the gas mixture by the box model [95],

$$\kappa_{\eta,g}(p_{\text{CH}_4}, p_0, T_g) = \frac{1}{\Delta\eta_{\text{box}}} \int_{\Delta\eta_{\text{box}}} \kappa_{\lambda,g}^*(p_{\text{CH}_4}, p_0, T_g) d\eta. \quad (2.10)$$

$\text{H}_2$  and Ar are assumed to be radiatively non-participating. The path length Monte Carlo method with ray redirection is applied to compute radiative flux divergence in the gas and solid phases [41],

$$\begin{aligned} \frac{\partial q_{r,g}}{\partial z} &= \int_0^{\infty} \frac{(1 - f_V) \kappa_{\lambda,g}}{\kappa_{\lambda,p} + (1 - f_V) \kappa_{\lambda,g}} \frac{\partial q_{r,\lambda}}{\partial z} d\lambda \\ &\approx (1 - f_V) \left( 4\kappa_{\text{P},g} \sigma T_g^4 - \frac{\sum_k q_{\text{ray},k} \kappa_{\lambda,g} ds_k}{dz} \right), \end{aligned} \quad (2.11)$$

$$\frac{\partial q_{r,p}}{\partial z} = \int_0^\infty \frac{\kappa_{\lambda,p}}{\kappa_{\lambda,p} + (1 - f_V) \kappa_{\lambda,g}} \frac{\partial q_{r,\lambda}}{\partial z} d\lambda \approx 4\kappa_{P,p} \sigma T_p^4 - \frac{\sum_k q_{ray,k} \kappa_{\lambda,p} ds_k}{dz}, \quad (2.12)$$

where  $k$  designates a generic stochastic ray traversing in 3D the path length  $ds_k$  within sub-layer of thickness  $dz$  and carrying a portion of radiative flux  $q_{ray,k} = \left[ q_e + 4\sigma \int_0^L \left( (1 - f_V) \kappa_{P,g} T_g^4 + \kappa_{P,p} T_p^4 \right) dz \right] N_{rays}^{-1}$ . The path length to a scattering event is

$$\ln \mathcal{R}_s = - \int_0^s \sigma_{sca,\lambda,p}(s^*) ds^*, \quad (2.13)$$

where  $\mathcal{R}_s$  is a random number chosen from a uniform distribution set between 0 and 1. The corresponding probabilistic cumulative distribution functions for the wavelength and direction of emission of each phase, and direction of scattering by particles are equivalent to those employed in the classic collision-based MC for two-phase media [162].

## 2.4 Conservation equations

### 2.4.1 Mass conservation

Transient 1D mass conservation equations are formulated separately for the solid and the gas phases. The molar concentration and molar flux of the gas component  $i$  ( $i = \text{CH}_4, \text{H}_2, \text{Ar}$ ) are obtained from:

$$\frac{\partial \bar{\rho}_g}{\partial t} = - \frac{\partial \dot{n}_g}{\partial z} + \bar{\rho}_p \bar{r} \sum_i \nu_i, \quad \bar{\rho}_g(t, 0 \leq z \leq L) = \frac{(1 - f_V) p_0}{\bar{R} T_g}, \quad (2.14)$$

$$\frac{\partial \bar{\rho}_g \bar{x}_i}{\partial t} = - \frac{\partial \dot{n}_g \bar{x}_i}{\partial z} + \bar{\rho}_p \nu_i \bar{r}, \quad \sum_i \bar{x}_i = 1, \quad (2.15)$$

$$\bar{x}_i(t = 0, 0 \leq z \leq L) = \bar{x}_i(t \geq 0, z = 0) = \bar{x}_{i,0},$$

where  $\bar{x}_i$  is the stoichiometric coefficient of the gas component  $i$  in Eq. (2.2);  $\nu_{\text{CH}_4} = -1$ ,  $\nu_{\text{H}_2} = 2$ , and  $\nu_{\text{Ar}} = 0$ . The molar concentration of carbon

and the number of particles are obtained from:

$$\frac{\partial \bar{\rho}_p}{\partial t} = -\frac{\partial \dot{n}_p}{\partial z} + \bar{\rho}_p \nu_C \bar{r}, \quad \bar{\rho}_p = \frac{\rho_C f_V}{M_C}, \quad \dot{n}_p(t \geq 0, z = 0) \quad (2.16)$$

$$\frac{\partial \Gamma_p}{\partial t} = -\frac{\partial \dot{\gamma}_p}{\partial z}, \quad \dot{\gamma}_p = \frac{6\bar{m}_C \dot{n}_p}{\rho_C \pi d_p^3}, \quad \Gamma = \frac{6f_V}{\pi d_p^3}, \quad (2.17)$$

$$\begin{aligned} f_V(t = 0, 0 \leq z \leq L) &= f_V(t \geq 0, z = 0) = f_{V,0}, \\ d_p(t = 0, 0 \leq z \leq L) &= d_p(t \geq 0, z = 0) = d_{p,0}, \end{aligned} \quad (2.18)$$

where  $f_{V,0}$  and  $d_{p,0}$  are the inlet and initial particle volume fraction and diameter, respectively. The particle density of carbon is taken as  $\rho_C = 2,270 \text{ kg m}^{-3}$ . Furthermore, the carbon molar flux and mean particle diameter satisfy the following conditions,

$$\dot{n}_p = \begin{cases} \dot{n}_{p,0}, & \text{for } z = 0, \\ \frac{\partial \bar{\rho}_p}{\partial \bar{\rho}_g} \dot{n}_g, & \text{for } z > 0, \end{cases} \quad (2.19)$$

$$d_p = \begin{cases} d_{p,0}, & \text{for } t = 0, \\ \left( \frac{6f_V}{\pi \Gamma} \right)^{\frac{1}{3}}, & \text{for } t > 0, \end{cases} \quad (2.20)$$

where the particles are assumed to be suspended in the flow, thus no relative movement between gas and particles is considered. Eqs. (2.14)-(2.18) are derived by assuming no accumulation of gaseous components, no creation of new particles, and negligible effect of the gas volume change due to the particle growth.

### 2.4.2 Energy conservation

Transient 1D energy conservation equations are formulated separately for the solid and gas phases. For the gas phase at constant pressure,

$$\begin{aligned} \bar{c}_{p,g} \bar{\rho}_g \frac{\partial T_g}{\partial t} &= -\bar{c}_{p,g} \dot{n}_g \frac{\partial T_g}{\partial z} - \frac{\partial q_{r,g}}{\partial z} + \Gamma \pi d_p^2 \alpha (T_p - T_g) \\ &\quad + \bar{\rho}_p \nu_{H_2} \bar{r} [\bar{h}_{H_2}(T_p) - \bar{h}_{H_2}(T_g)], \end{aligned} \quad (2.21)$$

$$T_g(t = 0, 0 \leq z \leq L) = T_g(t \geq 0, z = 0) = T_{g,0}. \quad (2.22)$$

For the solid phase,

$$\begin{aligned} \bar{c}_{p,p}\bar{\rho}_p\frac{\partial T_p}{\partial t} = & -\bar{c}_{p,p}\dot{n}_p\frac{\partial T_p}{\partial z} - \frac{\partial q_{r,p}}{\partial z} - \Gamma\pi d_p^2\alpha(T_p - T_g) \\ & - \bar{\rho}_p\bar{r}\left(\sum_i \nu_i\bar{h}_i + \bar{h}_C\right), \end{aligned} \quad (2.23)$$

$$T_p(t = 0, 0 \leq z \leq L) = T_p(t \geq 0, z = 0) = T_{p,0}. \quad (2.24)$$

where  $\bar{h}_{\text{CH}_4} = \bar{h}_{\text{CH}_4}(T_g)$ ,  $\bar{h}_{\text{H}_2} = \bar{h}_{\text{H}_2}(T_p)$ , and  $\bar{h}_C = \bar{h}_C(T_p)$ . The limiting sphere model [65] is employed to compute the partial heat transfer coefficient  $\alpha_i$  between a particle and gaseous component  $i$ . The overall heat transfer coefficient is then  $\alpha = \sum_i \bar{x}_i\alpha_i$ , assuming independence from the inter-phase mass transfer and cross-interactions between molecules of different gaseous components. The finite volume method is applied to discretize Eqs. (2.11)-(2.24) in space [42, 51, 108]. Time integration is performed by applying the explicit Euler scheme [42, 51, 108]. Note that MC needs to be run at each time step due to time-variation of the radiative characteristics of each phase as the chemical reaction progresses.

## 2.5 Numerical results

The baseline simulation parameters are summarized in Tab. 2.1 and are used in all simulation runs unless stated otherwise. Absorption and extinction efficiency factors of C particles are plotted in Fig. 2.2 as a function of radiation wavelength for selected particle diameters  $d_p = 1, 2.5, 5,$  and  $10\mu\text{m}$ . As expected for geometric optics,  $E_{\text{ext},\lambda,p}$  approaches the value of 2 and  $E_{\text{abs},\lambda,p}$  the value of 1 for short wavelengths. Thus, refraction and reflection at short wavelengths is negligible while scattering is due to diffraction. Figures 2.3 and 2.4 show the scattering phase functions for two particle diameters,  $d_p = 1$  and  $10\mu\text{m}$ , and two radiation wavelengths  $\lambda = 0.5$  and  $2\mu\text{m}$ , corresponding to the peak for solar radiation and for Planck's emissive power at 1,450 K (above which  $\text{CH}_4$ -decomposition proceeds at reasonable rates), respectively. For  $d = 10\mu\text{m}$ , the forward scattering is highly predominant at both wavelengths, but this effect diminishes for  $d_p = 1\mu\text{m}$  particles, especially at  $\lambda = 2\mu\text{m}$ . Temperature response of the C particles

Parameter	Value	Unit
$L$	0.1	m
$L/\Delta z$	50	-
$N_{\text{rays}}$	$10^6$	-
$p_0, p_{\text{in}}$	101,325	Pa
$q_e$	$1.5 \cdot 10^6$	$\text{W m}^{-2}$
$T_e$	5,780	K
$T_{g,0}, T_{g,\text{in}}$	300	K
$T_{p,0}, T_{p,\text{in}}$	300	K
$T_{\text{surr}}$	0	K
$\varepsilon_{\text{surr}}$	1	-

Table 2.1: Baseline parameters.

at  $z = L/2$  is shown in Fig. 2.5 for selected initial and inlet particle diameters  $d_{p,0} = 1, 2.5, 5,$  and  $10 \mu\text{m}$ . Both the heating rate and the steady-state temperature increase with decreasing particle size. For  $d_{p,0} = 1 \mu\text{m}$ , 1,500 K is reached in approximately 0.1 s, and steady-state temperature of 1,740 K is reached in less than 0.2 s, demonstrating the capability of extreme heating rates in directly-irradiated solar reactors. Even for  $d_{p,0} = 10 \mu\text{m}$ , steady state is still attained in less than 0.6 s. Higher temperatures and heating rates with smaller particles are due to augmented extinction of incident solar radiation, both by absorption and scattering, and due to the lower values of the "cut-off" wavelength that limit the particles' ability to emit radiation (see also Fig. 2.3 and 2.4).

Fig. 2.6 shows the variation of the spectral absorption and extinction coefficients with time at  $z = L/2$  for  $f_{V,0} = 10^{-5}$  and  $\lambda = 0.5 \mu\text{m}$ , and for two initial particle diameters  $d_{p,0} = 1$  and  $10 \mu\text{m}$ . The initial  $\kappa_{\lambda,p}$  for  $d_{p,0} = 1 \mu\text{m}$  is larger by one order of magnitude than that for  $d_{p,0} = 10 \mu\text{m}$ . The rapid decrease of both  $\kappa_{\lambda,p}$  and  $\beta_{\lambda,p}$  in the initial 150 ms is explained by the decrease of  $f_V$  as a result of gas thermal expansion during the rapid heating phase. This effect is more pronounced for smaller particles as they reach higher steady-state temperatures. Thereafter, the radiation coefficients undergo a slight but steady increase because of increasing  $f_V$  caused by particle growth during  $\text{CH}_4$ -decomposition. The latter effect cannot be observed for the larger  $10 \mu\text{m}$ -particles because of their lower

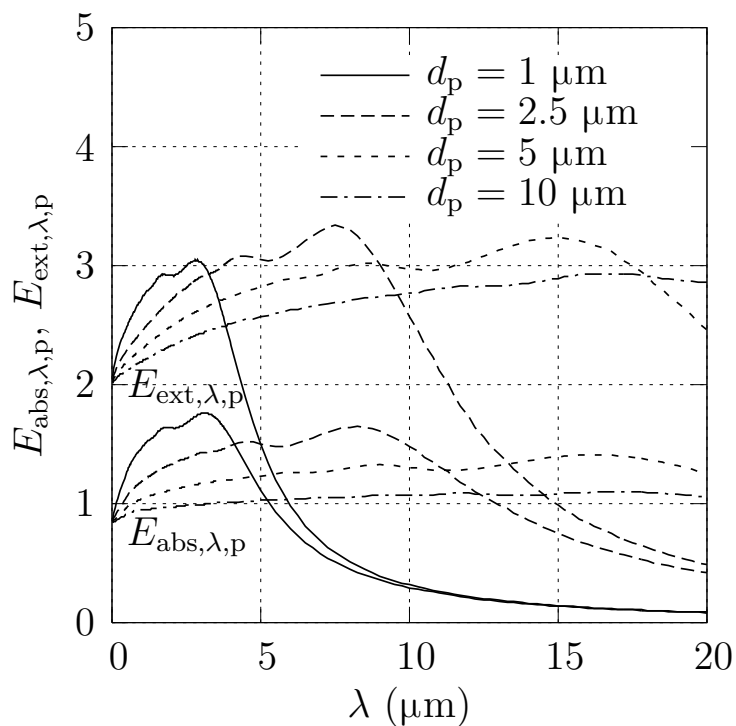


Figure 2.2: Spectral extinction and scattering efficiency factors of carbon particles for selected particle diameters  $d_p = 1, 2.5, 5,$  and  $10 \mu\text{m}$

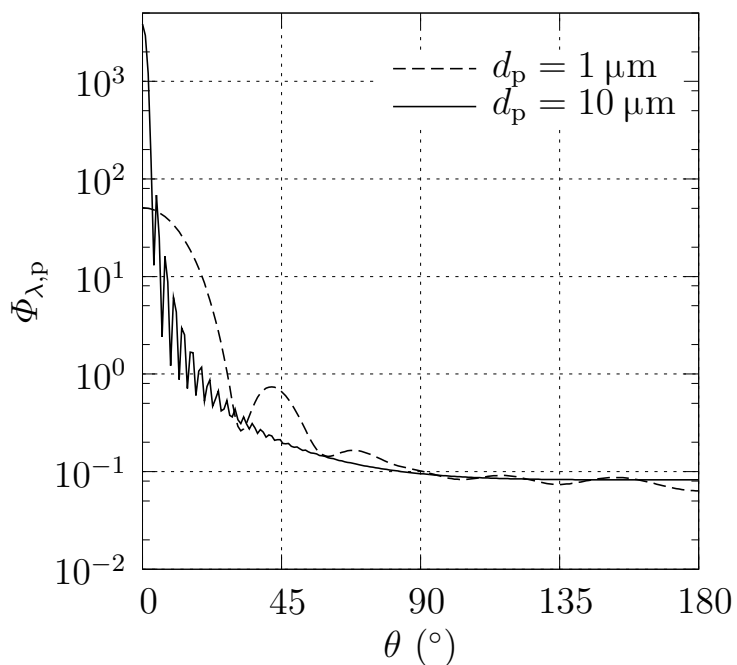


Figure 2.3: Scattering phase function of the particles for selected particle diameters  $d_p = 1$  and  $10 \mu\text{m}$ , at radiation wavelength of  $\lambda = 0.5 \mu\text{m}$ .

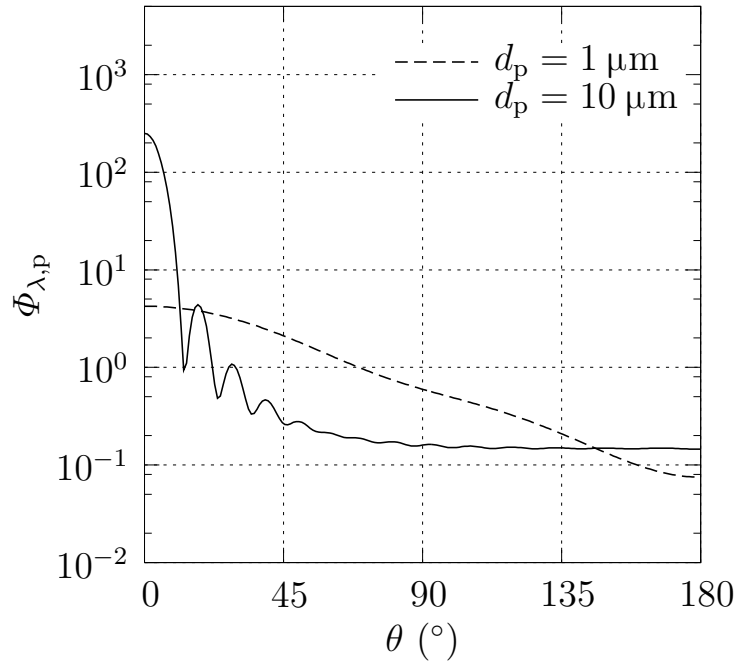


Figure 2.4: Scattering phase function of the particles for selected particle diameters  $d_p = 1$  and  $10 \mu\text{m}$ , at radiation wavelength of  $\lambda = 2 \mu\text{m}$ .

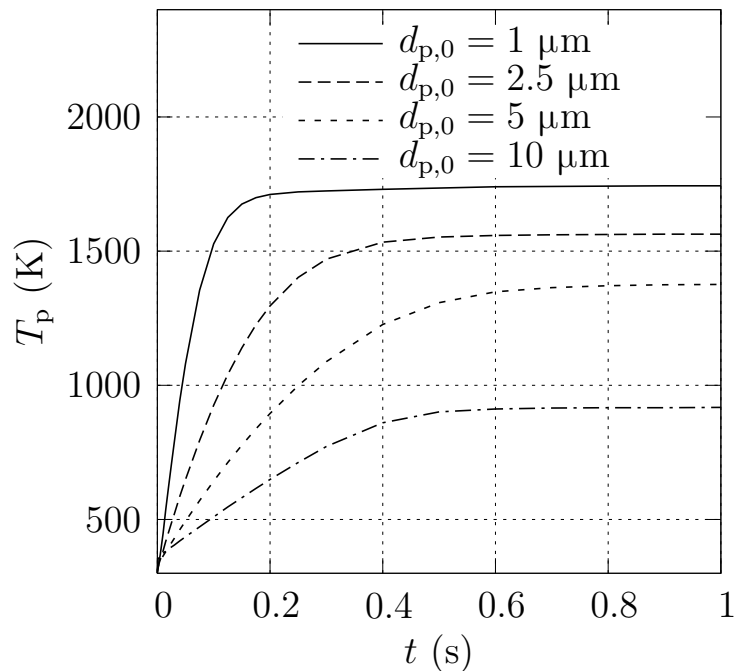


Figure 2.5: Transient particle temperature at  $z = L/2$  as a function of time for selected inlet/initial particle diameters  $d_{p,0} = 1, 2.5, 5,$  and  $10 \mu\text{m}$ .

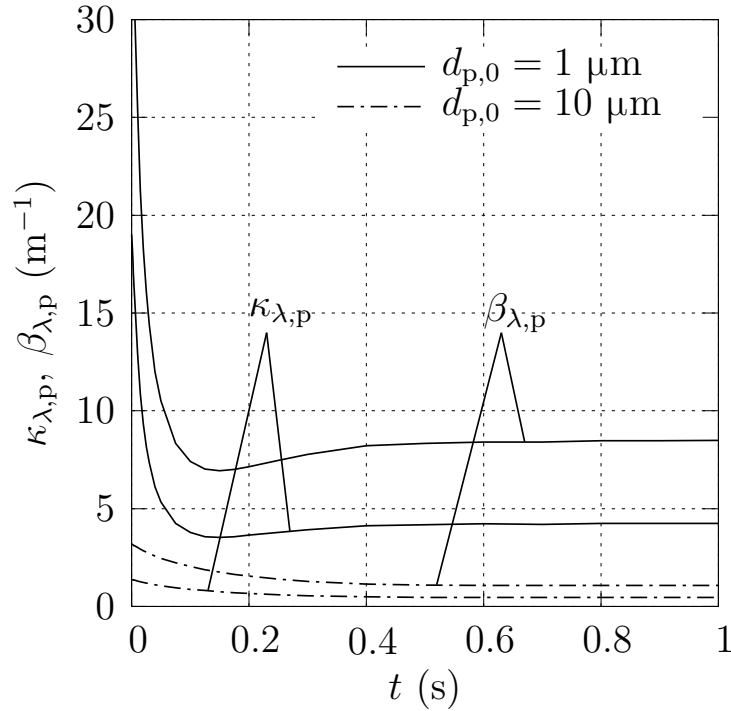


Figure 2.6: Transient spectral absorption and extinction coefficients at  $z = L/2$  for  $f_{V,0} = 10^{-5}$ ,  $\lambda = 0.5 \mu\text{m}$ , and for inlet/initial particle diameters  $d_{p,0} = 1$  and  $10 \mu\text{m}$ .

steady-state temperatures, as observed in Fig. 2.5, and hence a significantly lower rate of  $\text{CH}_4$ -decomposition and particle growth.

Fig. 2.7 shows the cumulative fraction of the incident solar radiation being absorbed directly or after single or multiple scattering along the slab at steady state for  $d_0 = 1, 2.5, 5,$  and  $10 \mu\text{m}$ . It is defined as:

$$A(z) = \frac{\int_0^z \frac{\partial q_{\text{abs}}}{\partial z^*} dz^*}{q_e}. \quad (2.25)$$

The total amount of absorbed solar radiation increases dramatically when the initial particle size is reduced: from about 12 % for  $d_{p,0} = 10 \mu\text{m}$  to over 65 % for  $d_{p,0} = 1 \mu\text{m}$ .

Figs. 2.8-2.10 show the variation of the steady-state temperature profiles across the slab with particle diameter (Fig. 2.8), particle volume fraction (Fig. 2.9), and  $\text{CH}_4$  molar concentration (Fig. 2.10). Increasing  $f_{V,0}$  at



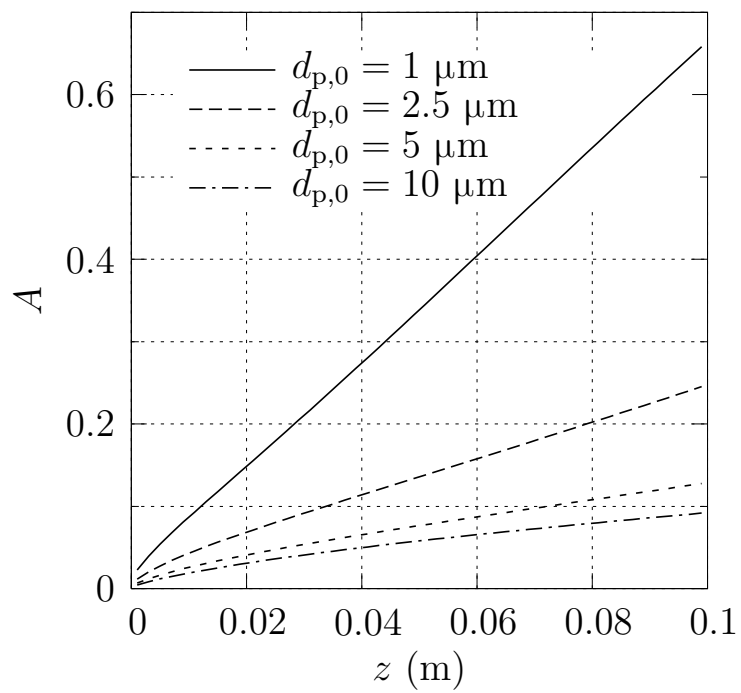


Figure 2.7: Steady-state cumulative absorbed fraction of external radiation along the slab for selected inlet/initial particle diameters  $d_{p,0} = 1, 2.5, 5,$  and  $10 \mu\text{m}$ .

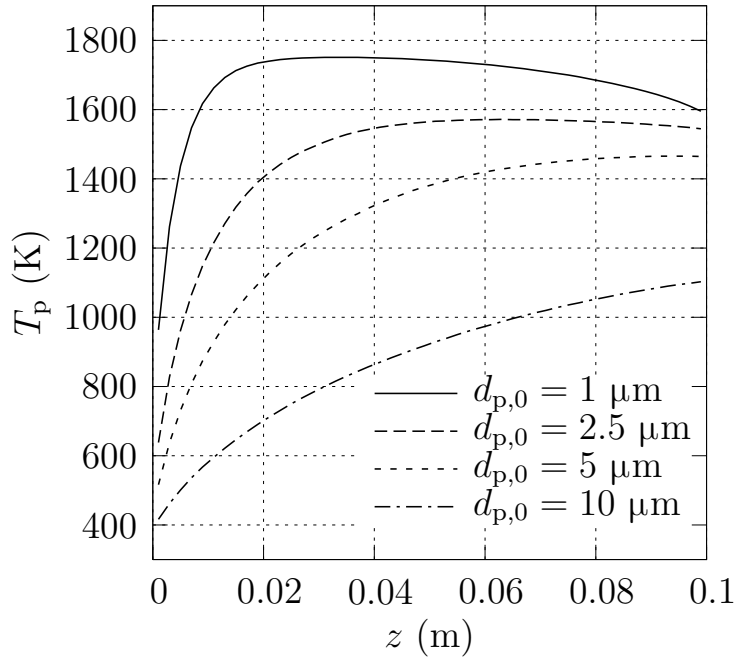


Figure 2.8: Steady-state particle temperature profile along the slab for selected inlet/initial particle diameters  $d_{p,0} = 1, 2.5, 5,$  and  $10 \mu\text{m}$ .

constant  $d_{p,0}$  or decreasing  $d_{p,0}$  at constant  $f_{V,0}$  lead to elevated steady-state temperatures as compared to those for the baseline case because of higher  $\kappa_{\lambda,p}$  and  $\beta_{\lambda,p}$  and consequently effective extinction. In contrast, an increase in  $\text{CH}_4$  concentration lowers the temperatures of both phases in spite of increasing  $\kappa_{\lambda,p}$  as a result of the 2-5 times higher  $\bar{c}_p$  of  $\text{CH}_4$  than that of Ar in the relevant temperature range.

The computations revealed that for the range of particle sizes, volume fractions, and methane molar fractions considered, the difference between the particle and gas temperatures at steady state is insignificant and reached a maximum of 53 K for  $d_{p,0} = 10 \mu\text{m}$ ,  $f_{V,0} = 10^{-5}$ ,  $\bar{x}_{\text{CH}_4} = 0.5$ , and  $z/L = 0.01$ . External thermal radiation is predominantly absorbed by the particles. For example, in the latter case, particles absorb about 100 times more effectively than the gas. Heat transfer between the solid and gas phases is predominantly by convection and by gas IR emission.

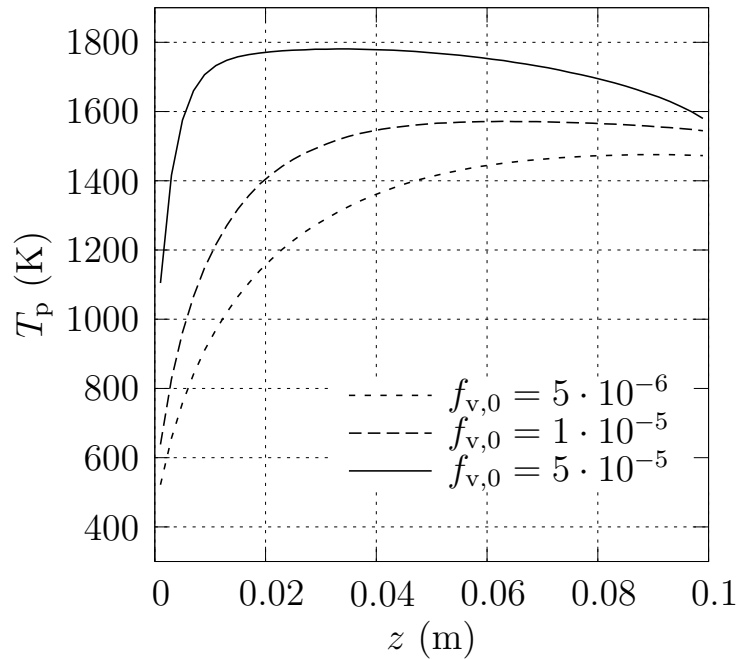


Figure 2.9: Steady-state particle temperature profile along the slab for selected inlet/initial particle volume fractions  $f_{V,0} = 0.5 \cdot 10^{-5}$ ,  $1 \cdot 10^{-5}$ ,  $5 \cdot 10^{-5}$ .

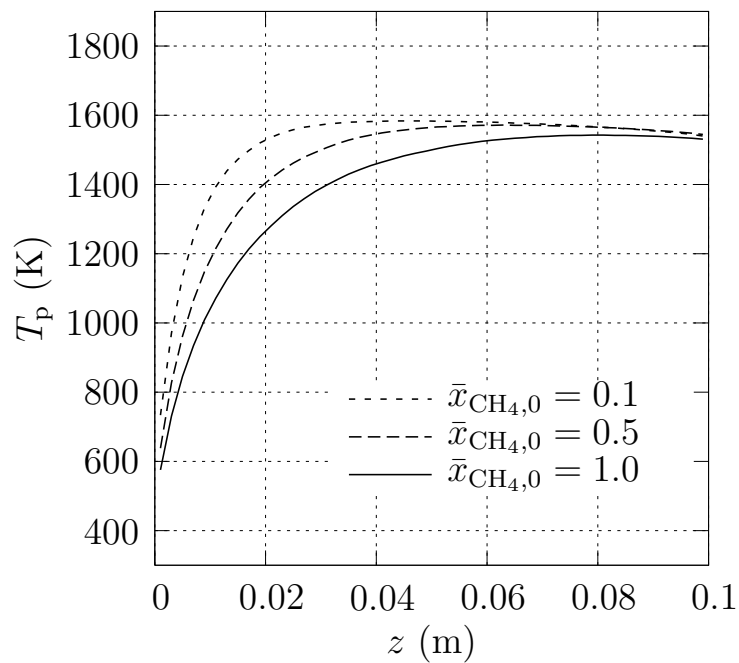


Figure 2.10: Steady-state particle temperature profile along the slab for selected inlet/initial  $\text{CH}_4$  molar fractions  $\bar{x}_{\text{CH}_4,0} = 0.1$ ,  $0.5$ , and  $1$ .

## 2.6 Summary

A numerical model was developed to compute temperature and chemical composition of a reacting two-phase solid-gas flow initially composed of  $\text{CH}_4$  laden with carbon particles, and directly exposed to concentrated solar radiation. Maximum (steady-state) temperatures in the range of 1,700–1,800 K were obtained for initial carbon particles of 1 – 10  $\mu\text{m}$  diameter and initial volume fraction in the range  $5 \cdot 10^{-6} - 5 \cdot 10^{-5}$ . The maximum  $\text{CH}_4$  conversion in steady-state was 46.5 % for the inlet and initial volume fraction and particle diameter of  $f_{V,0} = 5 \cdot 10^{-5}$  and  $d_{p,0} = 2.5 \mu\text{m}$ , corresponding to maximum particle temperatures of 1,780 K. Validation was accomplished by comparing the computed steady-state temperatures and reaction extents with those obtained experimentally using a particle-flow solar reactor prototype subjected to concentrated solar radiation. The model is applied, in Chap. 4, to estimate the net radiative heat flux from a hot absorber tube wall to a two-phase medium flowing inside the tube using cylindrical boundary conditions.

# Chapter 3

## Experimental work<sup>1,2</sup>

### 3.1 Introduction

The use of concentrated solar radiation as the energy source of high-temperature process heat has been experimentally demonstrated using directly-irradiated solar reactors - with reactants directly exposed to the concentrated solar irradiation [55, 69] - and indirectly-irradiated solar reactors - with graphite/ceramic tubes or other opaque surfaces serving as absorbers and heat conductors [3, 4, 29, 30, 116]. In a previous study [55], design and testing of a directly-irradiated solar reactor were described. The reactor featured a flow of CH<sub>4</sub> laden with carbon particles that served the functions of radiant absorbers and nucleation sites for the heterogeneous reaction, enhancing the chemical kinetics. This and previous experimental studies have pointed to the efficient means of heat transfer by the direct solar irradiation of particle suspensions [17, 71]. This chapter describes

---

<sup>1</sup>Material from this chapter has been published in: G. Maag, F. J. Gutiérrez, W. Lipiński, and A. Steinfeld. Thermal dissociation of CH<sub>4</sub> using a particle-flow chemical reactor exposed to concentrated solar radiation. In *Proceedings of the 2008 ASME International Mechanical Engineers Congress and Exhibition (IMECE)*, Boston, MA, USA, Oct-Nov 2008.

G. Maag, G. Zanganeh, and A. Steinfeld. Solar thermal cracking of methane in a particle-flow reactor for the co-production of hydrogen and carbon. *Int. J. Hydrogen Energy*, 34:7676-7685, 2009.

<sup>2</sup>The experimental campaigns were performed by a team led by the author that included M. Brühlhart, D. Brunner (at ETH, semester thesis), G. Zanganeh (at PSI, bachelor thesis), Dr. F. J. Gutiérrez, Dr. P. Loutzenhiser (at PSI), with the assistance of technical staff members P. Haueter (at ETH), K. Cuche, B. Jäggi, P. Schaller, S. Wepf, and D. Wuillemin (at PSI).

an improved reactor prototype that evolved from the previous design [55] and was employed in an experimental investigation aimed to elucidate the effect of the operational parameters, namely solar inlet power, seed particle volume fraction, total gas volume flow, and  $\text{CH}_4$  concentration on the reactor's thermal performance.

## 3.2 Solar reactor configuration

The 5 kW solar chemical reactor, described previously in detail [55], was modified to obtain a laminar axial particle flow through the cavity. The main modifications comprise the substitution of the tangential in- and outlet ports with four radial-axial  $\text{CH}_4$  inlet nozzles and a conical axial outlet to prevent deposition of carbonaceous material inside the cavity. Fig. 3.1 shows the reactor's new configuration. It consists of a 200 mm-length 100 mm-diameter cylindrical cavity receiver containing a 60 mm-diameter circular aperture to let in concentrated solar radiation. Because of multiple internal radiant reflections, the cavity-type geometry approaches a blackbody absorber that efficiently captures incoming solar radiation, as verified by Monte-Carlo ray tracing simulations [54]. The cavity is made from 10 mm-thick steel alloy, with inner walls lined with two 3 mm-thick  $\text{ZrO}_2$  layers to provide thermal insulation. A 240 mm-diameter, 3 mm-thick fused quartz window is mounted 80 mm in front of the aperture on a water-cooled conical copper funnel, where solar radiative fluxes are approximately 15 times lower than those obtained at the aperture plane. To cool and purge the window, Ar is injected through 4 nozzles at the front cone. A secondary Ar flow is injected through a ring gap at the aperture forming an aerodynamic gas curtain that prevents the particle flow from reaching the quartz window.  $\text{CH}_4$  laden with carbon black (CB) particles is injected through 4 inlet nozzles, positioned 30mm behind the aperture, right into the high radiative flux zone where the particles are rapidly heated to the desired temperature above 1,500 K at heating rates exceeding  $5,000 \text{ K s}^{-1}$ . These are directly exposed to the incoming solar irradiation, and act as radiant absorbers and nucleation surfaces for the heterogeneous cracking reaction. As the reaction occurs, the hot gas-particle flow progresses toward the rear part of cavity, where the products exit through a conical

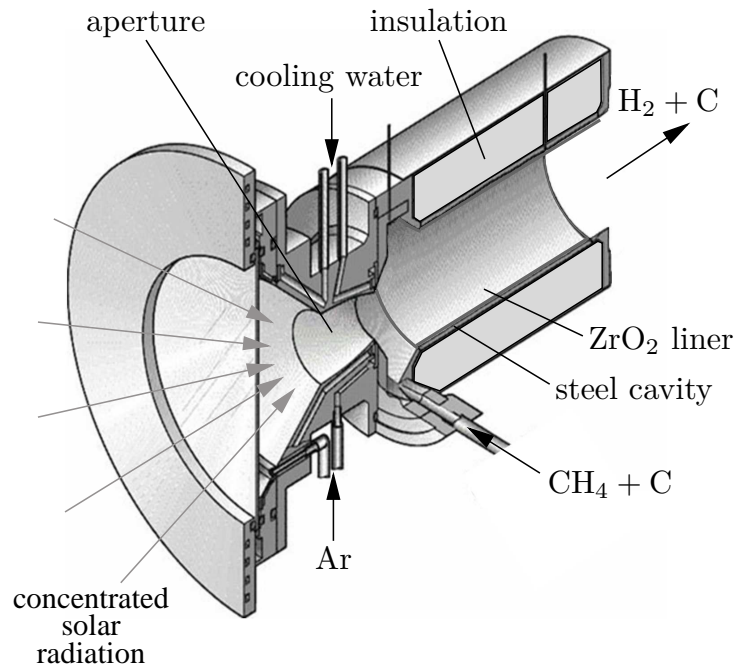


Figure 3.1: Scheme of the 5 KW particle-flow solar chemical reactor prototype.

steel funnel converging into an outlet tube leading to the cooler.

### 3.3 Experimental setup

Experimentation was carried out at ETH’s high-flux solar simulator and at PSI’s high-flux solar furnace. ETH’s high-flux solar simulator consists of a high-pressure Argon arc enclosed in a 27 mm-diameter, 200 mm-length water-cooled quartz envelope and close-coupled to a precision optical reflector to produce an intense beam of concentrated thermal radiation, that approaches the heat transfer characteristics of highly concentrating solar systems [56]. PSI’s high-flux solar furnace is made of a sun-tracking flat heliostat on-axis with an 8.5 m-diameter paraboloidal concentrator that provides 40 kW solar power with a peak solar concentration ratio<sup>3</sup> exceeding 5000 suns [49]. The experimental setup is shown schematically in Fig.

<sup>3</sup>The solar concentration ratio  $C$  is defined as  $C = Q_{\text{solar}} / (IA)$ , where  $Q_{\text{solar}}$  is the solar radiative power intercepted by the aperture of area  $A$ .  $C$  is often expressed in units of ”suns” when normalized to  $I = 1 \text{ kW m}^{-2}$ .

3.2. The reactor was positioned with its aperture at the focal plane of the lamp (ETH) or the solar concentrator (PSI). Three inlet gas flows, one for CH<sub>4</sub> and two for Ar, were controlled using Bronkhorst HI-TEC electronic flow controllers. Active carbon (AC) or carbon black (CB) particles were fed upstream into the conveying CH<sub>4</sub> stream by a rotating brush. Particle properties are given in Tab. 3.3. Their feeding rate was controlled by the speed of a piston delivering them to the brush, calibrated prior to the experimental runs. The inlet particle volume fraction was calculated as:

$$f_{V,\text{in}} = \frac{\dot{V}_{\text{p},\text{in}}}{\dot{V}_{\text{in}}} = \frac{\frac{\dot{m}_{\text{p},\text{in}}}{\rho_{\text{p}}}}{\left(\dot{V}_{\text{Ar},\text{in}} + \dot{V}_{\text{CH}_4,\text{in}}\right) \frac{T_{\text{in}}}{T_{\text{N}}} + \frac{\dot{m}_{\text{p},\text{in}}}{\rho_{\text{p}}}}. \quad (3.1)$$

The reactants' inlet temperature  $T_{\text{in}}$  was 298 K. Type-K thermocouples (TCs) were installed: twelve TCs on the outer cylinder shell and two TCs between the two layers of ZrO<sub>2</sub> inner liner. The average inner reactor wall temperature  $T_{\text{wall}}$  was then calculated by applying Fourier's Law. Pressure inside the cavity was monitored using pressure transducers. A slight overpressure was maintained inside the reactor, with a safety valve to prevent excessive pressure build-up on the quartz window due to plugging of the exit tube or thermal expansion of gas. Downstream, outlet products were cooled and the particles filtered. Gaseous products were then analyzed on-line by gas chromatography (GC, Agilent High Speed Micro G2890A, detection limit: 10 ppm, sampling rate: 0.01 Hz), supplemented by IR-based detectors for CH<sub>4</sub>, CO and CO<sub>2</sub> (Siemens Ultramat 23, detection limit: 0.2 %, sampling rate: 1 Hz), and a thermal conductivity based detector for H<sub>2</sub> (Siemens Calomat 6, detection limit: 50 ppm, sampling rate: 1 Hz). A constant flow of N<sub>2</sub>, at a mass flow rate of  $\dot{V}_{\text{N}_2} = 1 \text{ l}_{\text{N}} \text{ min}^{-1}$ , was added to the gaseous products in the outlet line to allow for the determination of the total molar outlet gas flow rate:

$$\dot{n}_{\text{g},\text{out}}(t) = \dot{n}_{\text{N}_2,\text{in}} \frac{1}{\bar{x}_{\text{N}_2,\text{out}}(t)}, \quad (3.2)$$

where  $\bar{x}_{\text{N}_2,\text{out}}$  denotes the molar fraction of N<sub>2</sub> in the outlet gas, as measured by GC. The molar outlet flow rate of each component  $i = \{\text{CH}_4, \text{H}_2, \text{CO}, \text{CO}_2, \text{O}_2\}$  is then

$$\dot{n}_{i,\text{out}} = \dot{n}_{\text{g},\text{out}} \bar{x}_{i,\text{out}}. \quad (3.3)$$



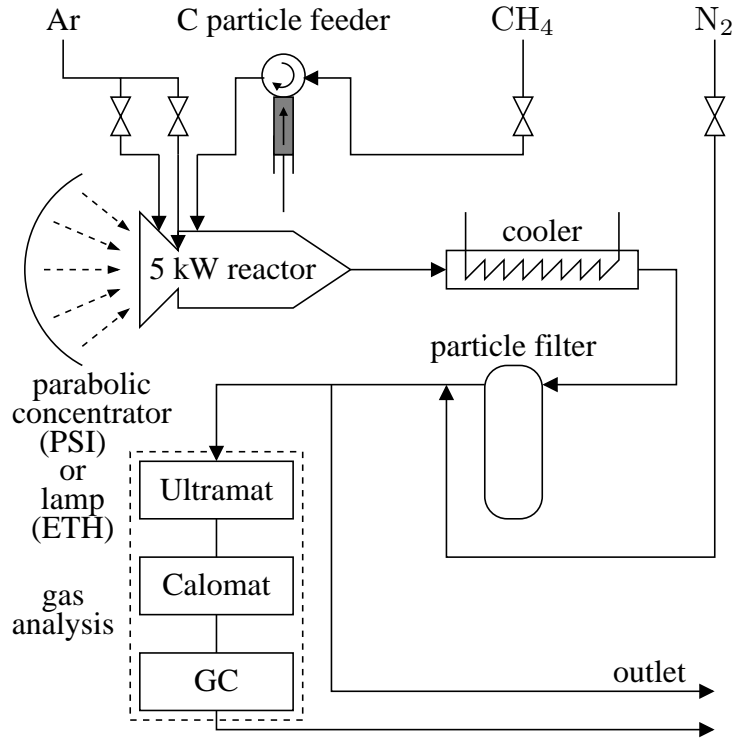


Figure 3.2: Schematic of the solar experimental setup at both facilities.

The average CH<sub>4</sub> conversion over the time lapse  $t_2 - t_1$  is defined as

$$X_{\text{CH}_4} = 1 - \frac{\int_{t_1}^{t_2} \dot{n}_{\text{CH}_4, \text{out}} dt}{\int_{t_1}^{t_2} \dot{n}_{\text{CH}_4, \text{in}} dt}. \quad (3.4)$$

The average H<sub>2</sub> yield between  $t_1$  and  $t_2$  is defined as

$$Y_{\text{H}_2} = \frac{\int_{t_1}^{t_2} \dot{n}_{\text{H}_2, \text{out}} dt}{2 \int_{t_1}^{t_2} \dot{n}_{\text{CH}_4, \text{in}} dt}. \quad (3.5)$$

$X_{\text{CH}_4}$  and  $Y_{\text{H}_2}$  are based on C-balance and H-balance, respectively, and were determined independently. Since the predicted concentrations of possible intermediate byproducts such as benzene (C<sub>6</sub>H<sub>6</sub>), ethane (C<sub>2</sub>H<sub>4</sub>), and acetylene (C<sub>2</sub>H<sub>2</sub>) are negligible for the temperature and residence time

ranges explored in this study [57], no significant difference between  $X_{\text{CH}_4}$  and  $Y_{\text{H}_2}$  was expected. GC analysis of the outlet gas confirmed the absence of significant amounts of other hydrocarbons. Assuming ideal gas, plug flow, and accounting for thermal gas expansion and gas formation by the chemical reaction, the residence time of the flow inside the cavity can be expressed as [80]:

$$\tau = \frac{pV_{\text{cavity}}}{\bar{R}T_{\text{wall},i} \left[ \dot{n}_{\text{Ar}} + \dot{n}_{\text{CH}_4} \left( 2 + \frac{Y_{\text{H}_2}}{\ln(1-Y_{\text{H}_2})} \right) \right]}. \quad (3.6)$$

The power consumed by the chemical reaction is

$$Q_{\text{chemical}} = X_{\text{CH}_4} \dot{n}_{\text{CH}_4, \text{in}} \Delta \bar{h}_{\text{R}}(T_{\text{wall},i}), \quad (3.7)$$

with  $\Delta \bar{h}_{\text{R}}(T_{\text{wall},i}) = \sum_i \nu_i \bar{h}_i(T_{\text{wall},i})$  for  $i = \{\text{CH}_4, \text{C}, \text{H}_2\}$ , being the enthalpy change of the reaction at reactor temperature per mole of  $\text{CH}_4$ . The power required for heating the reactants and the inert gas flow is

$$Q_{\text{thermal}} = \sum_i \dot{n}_{i, \text{in}} \int_{T_{\text{in}}}^{T_{\text{wall},i}} \bar{c}_{p,i}(T) dT. \quad (3.8)$$

with  $i = \{\text{CH}_4, \text{C}, \text{Ar}\}$ . Equations (3.7) and (3.8) are based on the assumption that the reaction occurs at  $T_{\text{wall},i}$ , as the particle heating time is one order of magnitude smaller than the residence time  $\tau$ .  $Q_{\text{conduction}}$  is the conduction heat loss through the cavity insulation, the rear steel flange, and the frontal cone.  $Q_{\text{reradiation}}$  is the re-radiation through the aperture, composed of radiation reflected/emitted by the window and transmitted from the cavity [164]. The solar-to-thermal energy conversion efficiency is defined as the ratio of the net power absorbed by heating the reactants to  $T_{\text{wall},i}$  and by driving the chemical reaction to the solar power input through the reactor's aperture,

$$\eta_{\text{thermal}} = \frac{Q_{\text{thermal}} + Q_{\text{chemical}}}{Q_{\text{solar}}}. \quad (3.9)$$

## 3.4 Experimental results

### 3.4.1 Solar simulator

A list of the main parameters and operational data of 29 solar experimental runs at ETH's solar simulator is given in Tab. 3.1. The values were obtained under approximate steady-state conditions. The following types of active carbon (AC) particles were fed: Fluka 05100, Fluka 05120, CarboTech PAK 800, and Merck Active Carbon. Particle properties are given in Tab. 3.3. The investigated operational parameters, in addition to the particle type, were: carbon particle mass flow rate (varied in the range 0.66-4.08 g min<sup>-1</sup>), Ar volume flow rate (varied in the range 5.9-12.3 l<sub>N</sub> min<sup>-1</sup>), CH<sub>4</sub> mass flow rate (varied in the range 1.7-4.0 l<sub>N</sub> min<sup>-1</sup>), and solar input flux (varied in the range 0.788–1.584 MW m<sup>-2</sup>). Typically, the reactor was heated to the desired operation temperature that was limited by material constraints, in this case the m.p. of the steel alloy cavity walls, 1,350 K (the ZrO<sub>2</sub> insulation layer not having been used for solar simulator experiments). It was then kept isothermally under an Ar flow by regulating the incoming radiative power via the solar simulator's arc current. Afterwards, CH<sub>4</sub> was fed until it was detected by the gas analysis downstream. Usually, a certain amount of H<sub>2</sub> was already produced in this phase due to cracking on the hot cavity walls. As soon as the CH<sub>4</sub> concentration at the outlet became steady, the particle feeder was switched on. It followed an immediate increase of the reactor wall temperature by about 10-20 K as a result of higher radiative absorption by the particle suspension. An associated increase of the H<sub>2</sub> concentration in the product gas indicated reaction in progress. Negligible quantities of CO and CO<sub>2</sub> were registered as well, presumably originating from pyrolysis of the carbon particles fed and/or from their combustion with some residual fraction of O<sub>2</sub> present inside the reactor cavity. The feeding was continued until steady state of the exhaust gas species' concentrations was established. For each run, average values from a 3-min interval under approximate steady state conditions were recorded.

Figure 3.3 shows the chemical conversion efficiencies for all experimental runs at ETH's solar simulator. A maximum  $X_{\text{CH}_4}$  of 21.6 % (run #16) and  $Y_{\text{H}_2}$  of 20.1 % (run #4) were achieved. Generally, the two values

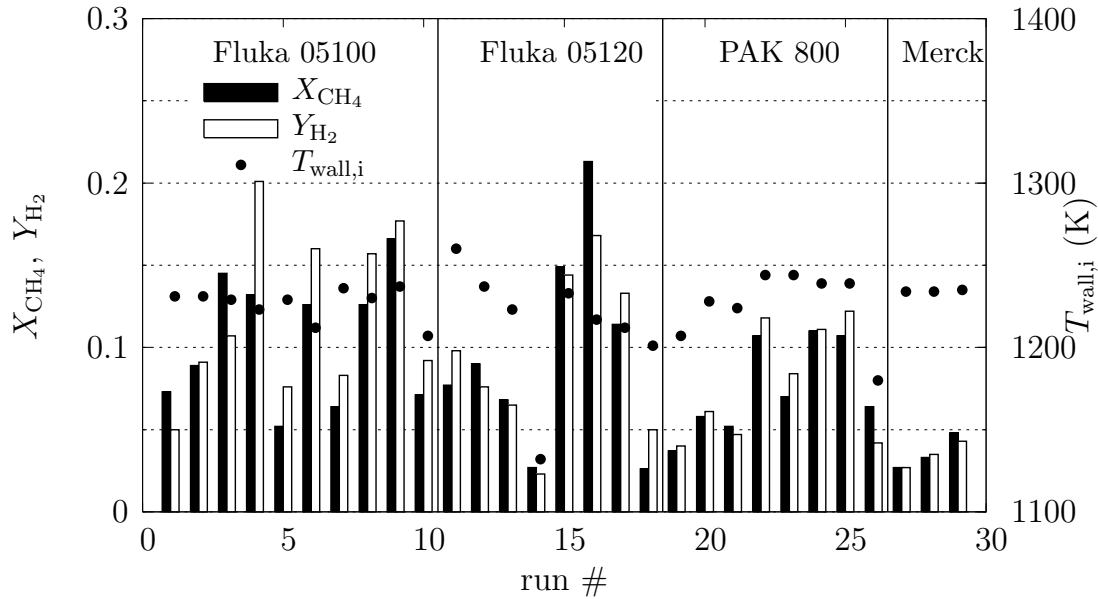


Figure 3.3:  $\text{CH}_4$  conversion and  $\text{H}_2$  yield obtained for all solar experimental runs at ETH’s high-flux solar simulator, grouped according to the laden carbon particles.

were in good agreement.  $Y_{\text{H}_2} > X_{\text{CH}_4}$  because of the release of volatiles derived from the laden particles that further underwent in-situ thermal decomposition to generate additional  $\text{H}_2$ . Discrepancies are attributed to the accuracy of the inlet mass flow rate measurement. Figures 3.4-3.6 show  $Y_{\text{H}_2}$  as a function of the main operational parameters: injected particle volume fraction (Fig. 3.4), solar power input (Fig. 3.5), and particle type (Fig. 3.6). As expected, the reaction extent increases with increasing particle feeding rate (and thus  $f_{V,\text{in}}$ ), because of the enhanced kinetics and augmented radiative absorption by an optically thicker medium. Similarly, a positive effect is attained by increasing the solar power input (and thus the radiative flux incident on the gas-particle flow), leading obviously to higher temperatures and reaction rates.  $Y_{\text{H}_2}$  obtained using Merck AC (see Fig. 3.6) is generally lower than that obtained with other activated carbons ( $> 10\%$ ) because of the relatively larger particle diameter (hand-milled from mm-sized particles) and, consequently, lower specific surface area. Typical residence time of reactants inside the cavity, considering thermal gas expansion and doubling of moles, was about 1.3 seconds.

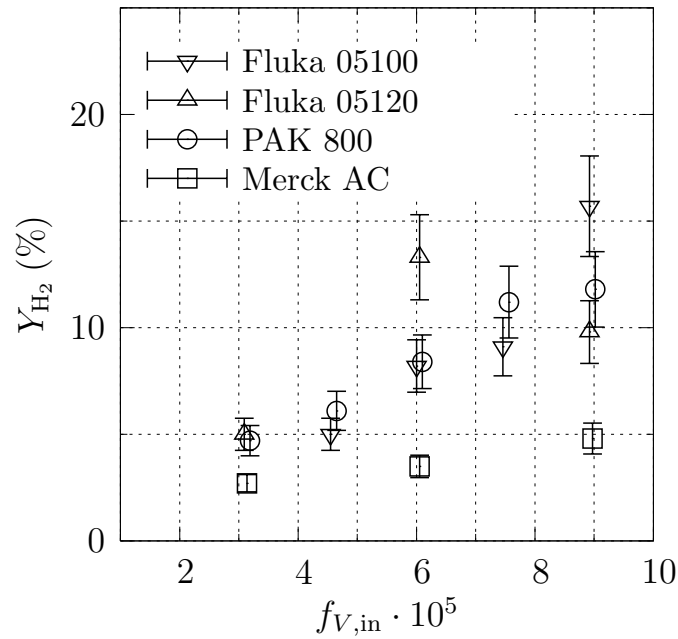


Figure 3.4: Hydrogen yield  $Y_{H_2}$  in function of inlet particle volume fraction  $f_{V,in}$  for different laden particle types.

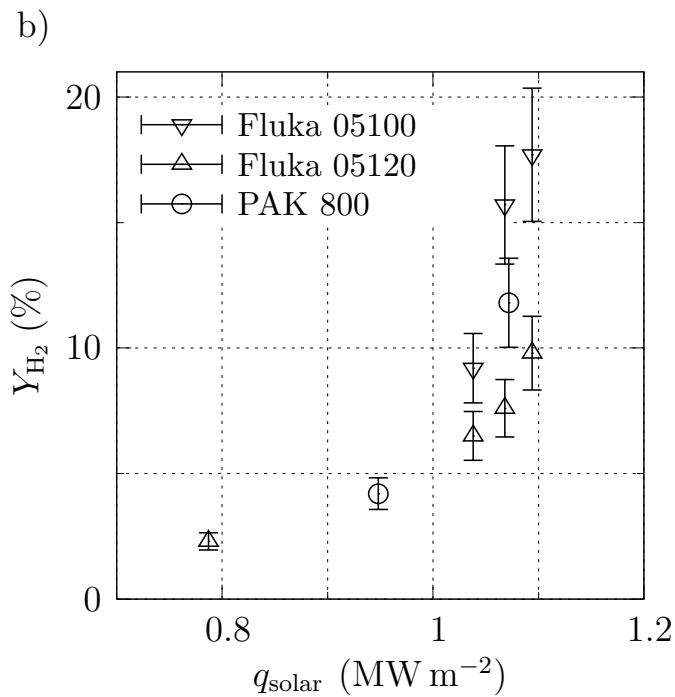


Figure 3.5: Hydrogen yield  $Y_{H_2}$  in function of inlet solar  $q_{solar}$  for different laden particle types.

Run #	carbon type	$\dot{V}_{g,in}$ $\text{In min}^{-1}$	$\bar{x}_{\text{CH}_4,in}$	$q_{\text{solar}}$ $\text{MW m}^{-2}$	$f_{V,in} \cdot 10^5$	$T_{\text{reactor}}$ K	$X_{\text{CH}_4}$	$Y_{\text{H}_2}$	$Q_{\text{chemical}}$ W	$Q_{\text{heating}}$ W	$Q_{\text{conduction}}$ W	$Q_{\text{reradiation}}$ W	$\eta_{\text{thermal}}$
1	Fluka 05100	13.8	0.167	1.094	5.24	1.231	0.073	0.050	12	311	3,299	137	0.003
2	Fluka 05100	13.8	0.167	1.094	8.57	1.231	0.089	0.091	14	342	3,266	137	0.004
3	Fluka 05100	11.3	0.177	1.068	14.6	1.229	0.145	0.107	21	329	3,192	139	0.006
4	Fluka 05100	11.1	0.162	1.068	14.8	1.223	0.132	0.201	17	319	3,212	133	0.005
5	Fluka 05100	14.7	0.163	1.068	11.2	1.229	0.052	0.076	9	389	3,143	139	0.002
6	Fluka 05100	9.4	0.181	1.068	17.5	1.212	0.126	0.160	15	287	3,257	121	0.004
7	Fluka 05100	13.8	0.167	1.068	6.93	1.236	0.064	0.083	10	329	3,195	146	0.003
8	Fluka 05100	13.8	0.167	1.068	10.3	1.230	0.126	0.157	21	358	3,161	140	0.006
9	Fluka 05100	14.7	0.163	1.094	9.65	1.237	0.166	0.177	28	377	3,212	143	0.007
10	Fluka 05100	14.7	0.163	1.038	0.65	1.207	0.071	0.092	12	363	3,074	121	0.003
11	Fluka 05120	13.2	0.167	1.094	9.02	1.260	0.077	0.098	12	344	3,236	169	0.003
12	Fluka 05120	13.2	0.167	1.068	9.02	1.237	0.090	0.076	14	334	3,184	148	0.004
13	Fluka 05120	14.0	0.171	1.038	8.49	1.223	0.068	0.065	12	345	3,076	138	0.003
14	Fluka 05120	13.9	0.173	0.787	8.57	1.132	0.027	0.023	5	304	2,303	99	0.002
15	Fluka 05120	13.8	0.174	1.053	11.1	1.233	0.149	0.144	25	371	3,079	146	0.007
16	Fluka 05120	13.7	0.175	1.053	6.99	1.217	0.213	0.168	36	322	3,132	129	0.010
17	Fluka 05120	13.9	0.165	1.079	6.90	1.212	0.114	0.133	19	320	3,252	119	0.005
18	Fluka 05120	13.9	0.165	1.079	3.58	1.201	0.026	0.050	4	288	3,309	108	0.001
19	PAK 800	13.8	0.167	0.998	5.29	1.207	0.037	0.040	6	302	3,003	129	0.002
20	PAK 800	13.8	0.167	1.068	5.28	1.228	0.058	0.061	9	309	3,224	137	0.002
21	PAK 800	13.7	0.168	1.068	3.64	1.224	0.052	0.047	8	291	3,247	133	0.002
22	PAK 800	13.8	0.167	1.068	10.2	1.244	0.107	0.118	17	364	3,144	155	0.005
23	PAK 800	13.9	0.165	1.068	6.88	1.244	0.070	0.084	11	334	3,180	155	0.003
24	PAK 800	13.9	0.165	1.068	8.54	1.239	0.110	0.111	18	348	3,165	150	0.005
25	PAK 800	13.7	0.168	1.068	12.1	1.239	0.107	0.122	17	377	3,137	149	0.005
26	PAK 800	13.8	0.159	0.924	10.3	1.180	0.064	0.042	10	333	2,816	111	0.003
27	Merck AC	13.9	0.165	1.068	3.56	1.234	0.027	0.027	4	298	3,234	144	0.001
28	Merck AC	13.9	0.165	1.068	6.86	1.234	0.033	0.035	5	330	3,198	146	0.001
29	Merck AC	13.9	0.165	1.068	10.2	1.235	0.048	0.043	8	362	3,165	145	0.002

Table 3.1: Operational parameters and results of the solar experimental runs at ETH's high-flux solar simulator using various types of active carbon as seed particles.

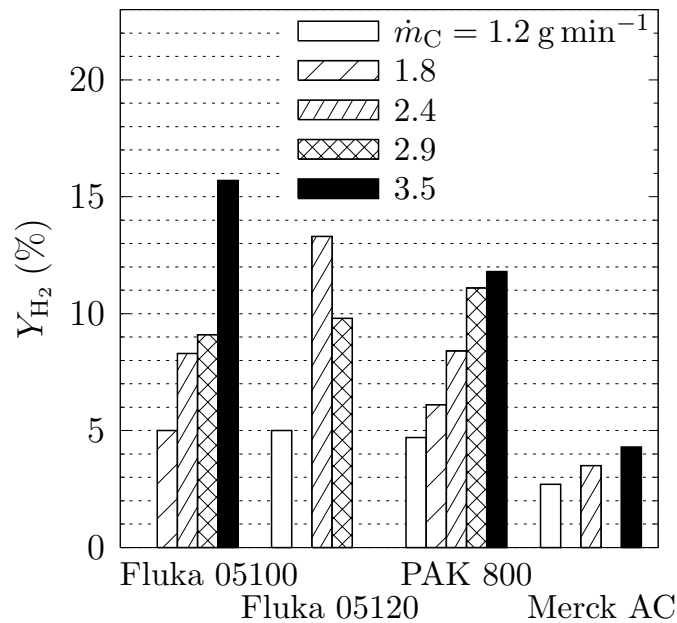


Figure 3.6: Hydrogen yield  $Y_{H_2}$  in function of inlet particle mass flow rate  $\dot{m}_{p,in}$  and different laden particle types.

### 3.4.2 Solar furnace

Radiative flux at the focal plane of the solar concentrator was measured optically prior to each experimental run using a calibrated CCD camera focused on a water-cooled,  $Al_2O_3$ -plasma-coated Lambertian (diffusely-reflecting) target. Numerical integration over the aperture area yielded the solar power input  $Q_{solar,in}$  with an accuracy of  $\pm_{13}^9 \%$  [164]. Assuming a linear dependence of  $Q_{solar}$  on the solar irradiation  $I$  and the beam transmission by the solar furnace's venetian-type shutter  $\psi$ , the solar power input to the reactor at any time was given by

$$Q_{solar}(t) = Q_{solar,0} \frac{I(t) \psi(t)}{I_0 \psi_0}, \quad (3.10)$$

where the index 0 indicates the time the flux measurement is taken. The particles used were Cabot Black Pearls 2000 (CB), whose properties are listed in Table 3.3. The main operational parameters and results under approximate steady-state conditions are listed in Tab. 3.2 for 20 solar experimental runs. The investigation was carried out on the following parameters: carbon particle volume fraction in the range  $0 - 7.2 \cdot 10^{-5}$ , gas

inlet volume flow rate in the range  $8.615.6 \text{ l}_N \text{ min}^{-1}$ <sup>4</sup>,  $\text{CH}_4$  inlet molar fraction in the range  $0.03 - 0.30$ , and average incoming solar radiation flux in the range  $0.98 - 1.72 \text{ MW m}^{-2}$  (equivalent to an average solar concentration ratio in the range 980-1,720 suns). Calculated residence times of the reacting medium (Eq. (3.6)) inside the cavity were in the range 1.1-2.4 s. Maximum incoming solar power through the aperture was 4.87 kW. Prior to each experimental run, the reactor was purged using a constant Ar stream and heated to the desired temperature. To avoid overheating over maximum inner reactor wall ( $\text{ZrO}_2$  insulation) temperatures of 1,650 K, the solar power input was regulated by controlling the furnace shutter transmission  $\psi(t)$ . Having reached the desired steady-state temperature, the injection of  $\text{CH}_4$  laden with CB particles was started, which was followed by an immediate drop of the inner wall temperature by about 50 K due to the energy sink for heating the reactants and for driving the chemical reaction, as well as due to shadowing of incoming radiation created by the particle cloud. An associated increase of the measured  $\text{H}_2$  concentration in the product gas indicated reaction in progress. Byproducts such as CO and  $\text{CO}_2$  were registered in negligible quantities, presumably originating from pyrolysis of the fed CB particles or their combustion with residual  $\text{O}_2$  present in the cavity. Once the outlet gas concentrations reached steady values, these conditions were kept for at least 200 s to allow for a minimum of three GC measurement cycles.

Fig. 3.7 shows the extent of reaction in terms of the  $\text{CH}_4$  conversion and  $\text{H}_2$  yield for experiments ordered by increasing  $T_{\text{wall},i}$ . Peak values achieved were  $X_{\text{CH}_4} = 98.8\%$  and  $Y_{\text{H}_2} = 99.1\%$ . The difference between  $X_{\text{CH}_4}$  and  $Y_{\text{H}_2}$  is attributed to the accuracy of the inlet gas flow rate measurements of  $\pm 15\%$ , entailing significant uncertainties in the determination of  $Y_{\text{H}_2}$  of up to  $\pm 20\%$  when approaching full conversion. No clear correlation is observable between  $T_{\text{wall},i}$  and the extent of reaction. A more indicative temperature of the reaction is the particle temperature, which can be calculated by radiative exchange between the reactor walls and the participating medium (see Chap. 2 and is estimated to be about 200 K higher than  $T_{\text{wall},i}$ . The particle temperature strongly depends on the particle suspension's optical properties, especially its extinction coefficient, which

---

<sup>4</sup> $\text{l}_N$  means liters at normal conditions; mass flow rates are calculated at 273 K and 1 bar.



Run #	$V_{g,in}$ $l_N \text{ min}^{-1}$	$x_{CH_4,in}$	$q_{solar}$ $\text{MW m}^{-2}$	$f_{V,in} \cdot 10^5$	$T_{reactor}$ K	$X_{CH_4}$	$Y_{H_2}$	$Q_{chemical}$ W	$Q_{heating}$ W	$Q_{conduction}$ W	$Q_{radiation}$ W	$\eta_{thermal}$	$\eta_{thermal}^*$
30	10.1	0.297	1.167	1.55	1,519	0.514	0.560	123	344	2,385	439	0.142	0.278
31	10.1	0.297	1.061	2.40	1,446	0.417	0.595	131	351	2,233	319	0.161	0.307
32	10.1	0.297	1.019	2.40	1,416	0.423	0.500	110	351	2,167	274	0.160	0.291
33	10.4	0.077	1.408	0.00	1,317	<sup>a</sup>	0.384	22	188	3,498	249	0.053	<sup>b</sup>
34	10.4	0.077	1.644	0.72	1,367	0.977	0.763	44	200	3,712	292	0.0052	0.172
35	10.4	0.077	1.599	1.29	1,350	0.972	0.912	53	199	3,605	283	0.056	0.190
36	10.4	0.077	1.348	2.04	1,316	0.988	0.991	57	194	3,635	348	0.066	0.199
37	10.3	0.053	1.348	0.68	1,604	0.910	0.888	36	235	4,215	570	0.071	0.229
38	15.6	0.077	1.447	0.86	1,498	0.887	0.812	72	341	3,617	434	0.101	0.295
39	13.0	0.077	1.355	0.77	1,459	0.889	0.793	58	274	4,836	327	0.087	0.259
40	10.4	0.077	0.976	0.22	1,600	<sup>a</sup>	0.548	33	246	4,142	506	0.101	0.188
41	8.6	0.070	1.362	0.63	1,578	0.865	0.826	36	196	4,195	520	0.060	0.185
42	10.4	0.115	1.266	0.67	1,471	0.733	0.783	69	236	3,877	405	0.085	0.222
43	10.4	0.077	0.990	0.96	1,301	0.635	0.697	40	207	3,460	217	0.088	0.245
44	10.4	0.077	1.075	0.96	1,335	0.703	0.847	42	195	3,314	190	0.078	0.251
45	10.4	0.077	1.075	0.96	1,309	0.622	0.799	46	189	3,230	190	0.077	0.252
46	13.6	0.059	1.305	0.74	1,527	0.827	0.925	55	294	4,031	415	0.095	0.275
47	12.0	0.067	1.305	0.84	1,463	0.795	0.916	54	249	3,839	326	0.082	0.261
48	10.6	0.091	1.206	0.95	1,575	0.792	0.897	64	253	4,085	498	0.093	0.305
49	10.6	0.091	1.722	1.63	1,518	0.911	0.870	61	233	4,056	474	0.060	0.258

<sup>a</sup> Unavailable  $CH_4$  measurement.

<sup>b</sup> Model simulation cannot handle  $f_{V,in} = 0$ .

Table 3.2: Operational parameters and results of the solar experimental runs at PSI's solar furnace using Cabot Black Pearls 2000 as seed particles.

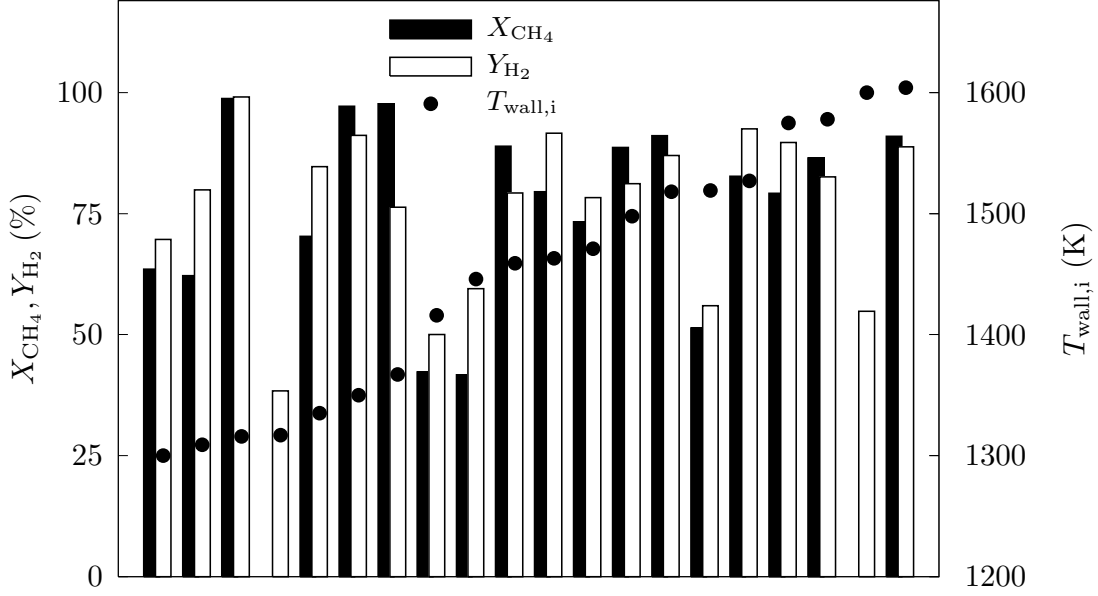


Figure 3.7: Methane conversion and hydrogen yield (see Eqs. (3.4) and (3.5)) for all 20 solar experimental runs at PSI’s high-flux solar furnace, ordered by increasing inner reactor wall temperature  $T_{\text{wall},i}$ .

in turn is a function of the particle volume fraction and determines the penetration and absorption of concentrated solar radiation. In fact, runs with high  $f_{V,\text{in}}$  ( $> 0.95 \cdot 10^{-5}$ ) resulted in chemical conversions above 50 % in spite of the relatively low  $T_{\text{wall},i}$  ( $< 1350$  K). Higher particle loading implies higher attenuation and, consequently, a more efficient absorption, resulting in the gas/particle flow being hotter than the reactor walls, as the optically-thicker particle cloud serves as a radiation shield [54]. It further augments the reaction rate due to a larger specific surface area available for the heterogeneous reaction. The opposite is true for the runs with low  $f_{V,\text{in}}$ , resulting in  $T_{\text{wall},i} > 1600$  K. For the computation of  $f_V$ ,  $\rho_{\text{CB}} = 1.8 \text{ kg m}^{-3}$ , given by the manufacturer, was used. To avoid overestimating the energetic performance of the reactor, Eqs. (3.6)-(3.8) use  $T_{\text{wall},i}$ . Figures 3.8-3.11 show  $X_{\text{CH}_4}$  and  $Y_{\text{H}_2}$  as function of the main operational parameters: injected particle volume fraction  $f_{V,\text{in}}$  for  $q_{\text{solar}} = 0.98 - 1.41 \text{ MW m}^{-2}$ ,  $\dot{V}_{\text{g},\text{in}} = 10.4 \text{ l}_\text{N} \text{ min}^{-1}$ ,  $\bar{x}_{\text{CH}_4,\text{in}} = 0.077$  (Fig. 3.8), incoming solar radiative flux  $q_{\text{solar}}$  for  $f_{V,\text{in}} = 8.3 - 9.7 \cdot 10^{-6}$ ,  $\dot{V}_{\text{g},\text{in}} = 10.4 - 12.0 \text{ l}_\text{N} \text{ min}^{-1}$ ,  $\bar{x}_{\text{CH}_4,\text{in}} = 0.067 - 0.091$  (Fig. 3.9), injected gas volume flow rate  $\dot{V}_{\text{g},\text{in}}$  for  $f_{V,\text{in}} = 6.3 - 9.7 \cdot 10^{-6}$ ,  $q_{\text{solar}} = 0.99 - 1.45 \text{ MW m}^{-2}$ ,  $\bar{x}_{\text{CH}_4,\text{in}} = 0.070 - 0.077$

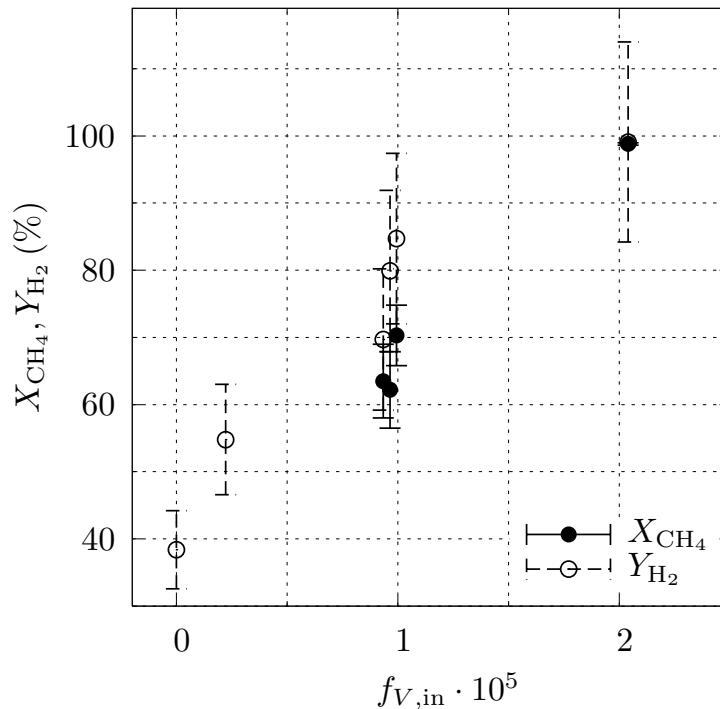


Figure 3.8: Variation of the methane conversion and hydrogen yield as a function of the inlet particle volume fraction  $f_{V,\text{in}}$ .

(Fig. 3.10), and  $\text{CH}_4$  inlet molar ratio  $\bar{x}_{\text{CH}_4,\text{in}}$  for  $f_{V,\text{in}} = 0.67 - 1.60 \cdot 10^{-5}$ ,  $q_{\text{solar}} = 1.17 - 1.35 \text{ MW m}^{-2}$ ,  $\dot{V}_{\text{g},\text{in}} = 10.1 - 12.0 \text{ l}_\text{N} \text{ min}^{-1}$  (Fig. 3.11). As the particle feeding rate was increased, the reaction extent increased as a result of the higher extinction/absorption of incoming solar radiation by the higher  $f_V$  within the cavity, which led to more elevated temperatures and, consequently, faster chemical kinetics. A similar effect was obtained by increasing  $q_{\text{solar}}$  through the aperture, also producing higher temperatures, faster kinetics, and higher conversions. If  $\dot{V}_{\text{g},\text{in}}$  is reduced, higher conversions are expected for longer residence times. In practice, the effect of  $\dot{V}_{\text{g},\text{in}}$  was relatively weak, as its variation was limited by the need of cooling and purging the quartz window. Finally, the effect of higher inlet  $\bar{x}_{\text{CH}_4,\text{in}}$  was that of increasing the specific heat of the medium, leading to lower reaction temperatures and, consequently, lower  $X_{\text{CH}_4}$  and  $Y_{\text{H}_2}$ . Generally, the observations qualitatively confirm those of Sec. 3.4.1.

An energy balance indicated an average  $\eta_{\text{thermal}} = 9.1 \%$ , with a maximum value of  $16.1 \%$  for  $f_{V,\text{in}} = 2.40 \cdot 10^{-5}$ ,  $\dot{V}_{\text{g},\text{in}} = 10.1 \text{ l}_\text{N} \text{ min}^{-1}$ ,  $\bar{x}_{\text{CH}_4,\text{in}} =$

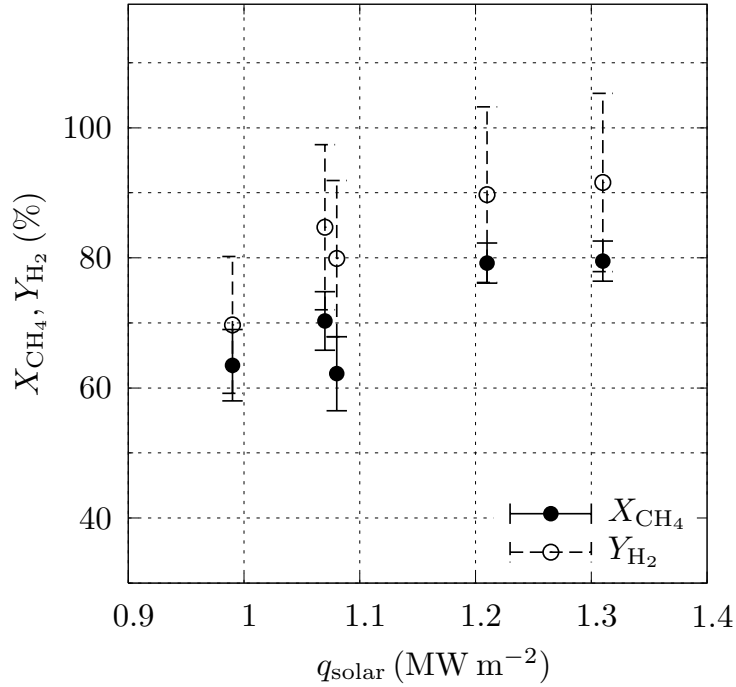


Figure 3.9: Variation of the methane conversion and hydrogen yield as a function of the incoming solar radiative flux  $q_{\text{solar}}$ .

0.297, and  $q_{\text{solar}} = 1.061 \text{ MW m}^{-2}$ . The main source of heat losses, approximately 80 % of  $Q_{\text{solar}}$ , occurred by conduction through the cavity walls. Here, a significant potential for improvement is present. Re-radiation losses were in the range 6-20 % of  $Q_{\text{solar}}$ , and - as expected - increasing with  $T_{\text{wall},i}$ . These losses can, to some extent be reduced by incorporating a secondary concentrator (e.g. CPC, [155]) at the reactor's aperture to reduce its size while boosting  $C$  and keeping  $Q_{\text{solar}}$  constant. Typically,  $Q_{\text{chemical}}$  and  $Q_{\text{heating}}$  represented 20 and 80 % of the net power absorbed.

Figs. 3.12-3.15 show  $\eta_{\text{thermal}}$  as a function of  $f_{V,\text{in}}$ ,  $q_{\text{solar}}$ ,  $\dot{V}_{g,\text{in}}$ , and  $\bar{x}_{\text{CH}_4,\text{in}}$ , respectively, for the experimental runs and parameter variations as those of Figs. 3.8-3.11.  $X_{\text{CH}_4}$  and  $Y_{\text{H}_2}$  increased with  $f_{V,\text{in}}$  (as seen in Figs. 3.8-3.11), but  $\eta_{\text{thermal}}$  remained at a constant level because of the increasing re-radiation and back-scattering losses caused by denser particle clouds close to the aperture. The influence of  $q_{\text{solar}}$  was small as both the numerator and denominator of Eq. (3.9) increase with it. Augmenting  $\dot{V}_{g,\text{in}}$  had a positive effect on the overall energetic performance since a higher rate of material was heated and reacted. The same observation is true for  $\bar{x}_{\text{CH}_4,\text{in}}$ ,

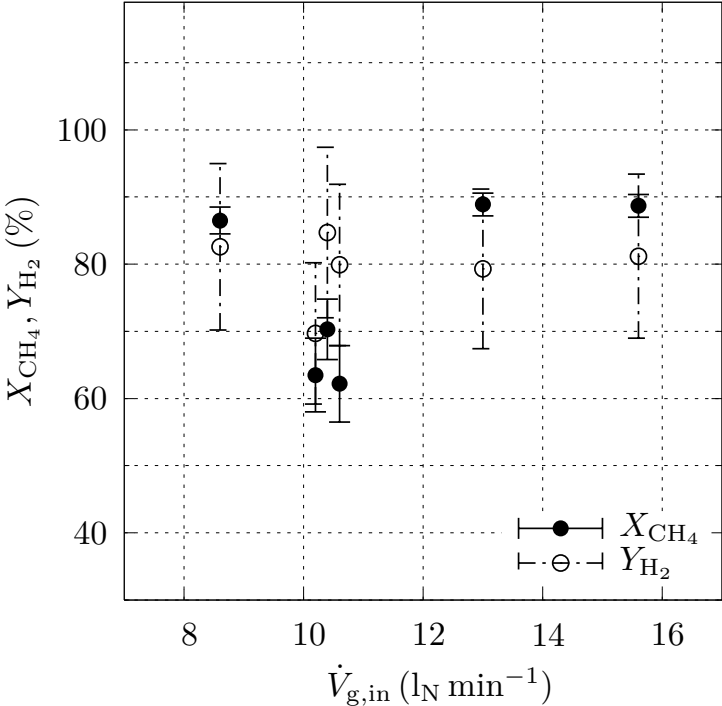


Figure 3.10: Variation of the methane conversion and hydrogen yield as a function of the inlet gas volume flow  $\dot{V}_{g,in}$ .

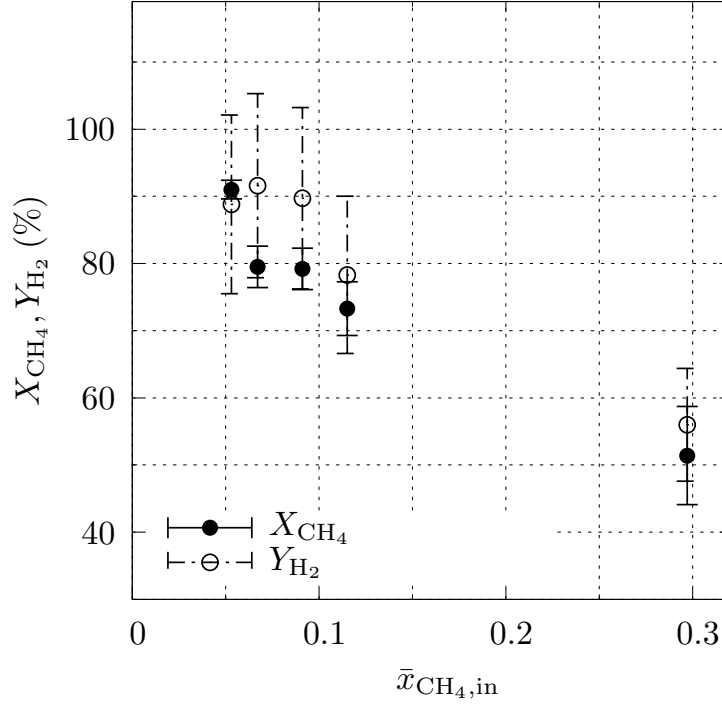


Figure 3.11: Variation of the methane conversion and hydrogen yield as a function of the inlet  $\text{CH}_4$  volume fraction  $\bar{x}_{\text{CH}_4,\text{in}}$ .

in this case due to the higher specific heat of  $\text{CH}_4$  compared to Ar. In fact, Fig. 3.15 indicates that the fraction of incoming solar power used to heat the reactants and to drive the reaction was strongly dependent on the dilution of  $\text{CH}_4$  with the carrier gas Ar, which was limited in this study because of facility constraints. To examine the full potential of the reactor in a commercial application, the use of pure  $\text{CH}_4$  as a reactant (i.e.  $\bar{x}_{\text{CH}_4,\text{in}}^* = 1$ ) was numerically simulated by applying the heat/mass transfer model shown in Chap. 2. In such a case, the solar-to-thermal energy conversion efficiency is formulated as:

$$\eta_{\text{thermal}}^* = \frac{Q_{\text{heating}}^* + Q_{\text{chemical}}^*}{Q_{\text{solar}}^*}, \quad (3.11)$$

where

$$Q_{\text{chemical}}^* = X_{\text{CH}_4} \dot{n}_{\text{CH}_4,\text{in}}^* \Delta \bar{h}_{\text{R}}(T_{\text{wall},i}), \quad (3.12)$$

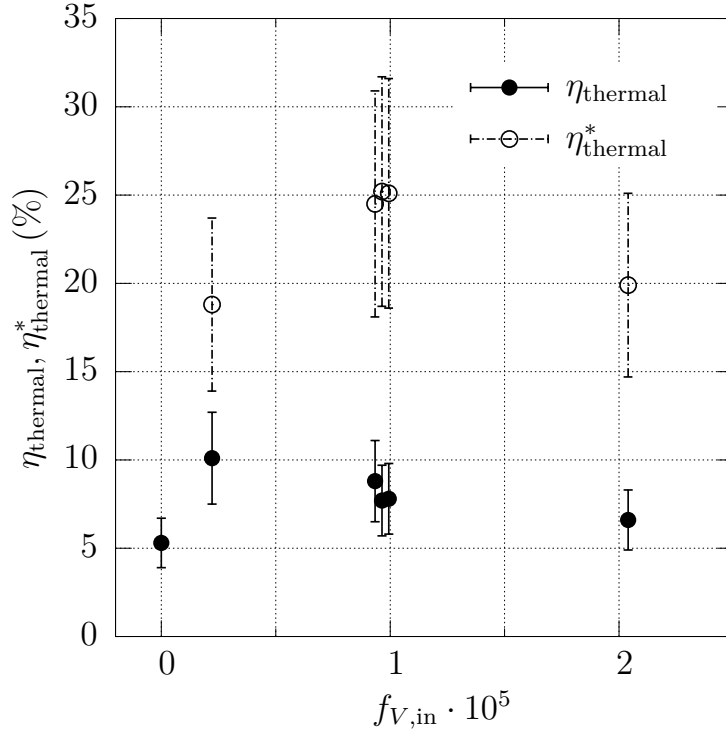


Figure 3.12: Variation of the solar-to-chemical energy conversion efficiency, experimentally obtained ( $\eta_{\text{thermal}}$ , ●) and numerically computed assuming  $\bar{x}_{\text{CH}_4,\text{in}} = 1$  ( $\eta_{\text{thermal}}^*$ , ○), as a function of the inlet particle volume fraction  $f_{V,\text{in}}$ .

and

$$Q_{\text{heating}}^* = \sum_i \dot{n}_{i,\text{in}}^* \int_{T_{\text{in}}}^{T_{\text{wall},i}} \bar{c}_{p,i}(T) dT. \quad (3.13)$$

The inlet molar flows are  $\dot{n}_{\text{CH}_4,\text{in}}^* = \dot{n}_{\text{CH}_4,\text{in}}/\bar{x}_{\text{CH}_4,\text{in}}$ , and  $\dot{n}_{\text{Ar},\text{in}}^* = 0$ . The model simulation assumes that the reactor temperatures and  $\text{CH}_4$  conversions are equal to those experimentally measured, i.e.  $T_{\text{wall},i}^* = T_{\text{wall},i}$  and  $X_{\text{CH}_4}^* = X_{\text{CH}_4}$ , and that  $Q_{\text{solar}}$  is adjusted to account for the higher specific heat of  $\text{CH}_4$  relative to Ar. The calculated  $\eta_{\text{thermal}}^*$  is shown in Fig. 3.12-3.14 as a function of  $f_{V,\text{in}}$ ,  $q_{\text{solar}}$ , and  $\dot{V}_{g,\text{in}}$ , respectively, and reaches an average value of 24.5 % and a maximum of 30.7 %.

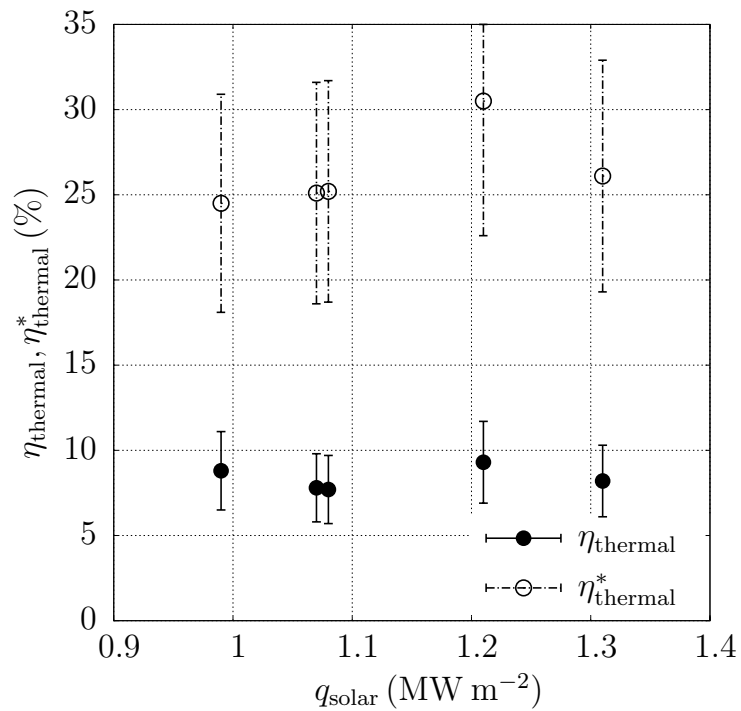


Figure 3.13: Variation of the solar-to-chemical energy conversion efficiency, experimentally obtained ( $\eta_{\text{thermal}}$ ,  $\bullet$ ) and numerically computed assuming  $\bar{x}_{\text{CH}_4, \text{in}} = 1$  ( $\eta_{\text{thermal}}^*$ ,  $\circ$ ), as a function of the incoming solar radiative flux  $q_{\text{solar}}$ .



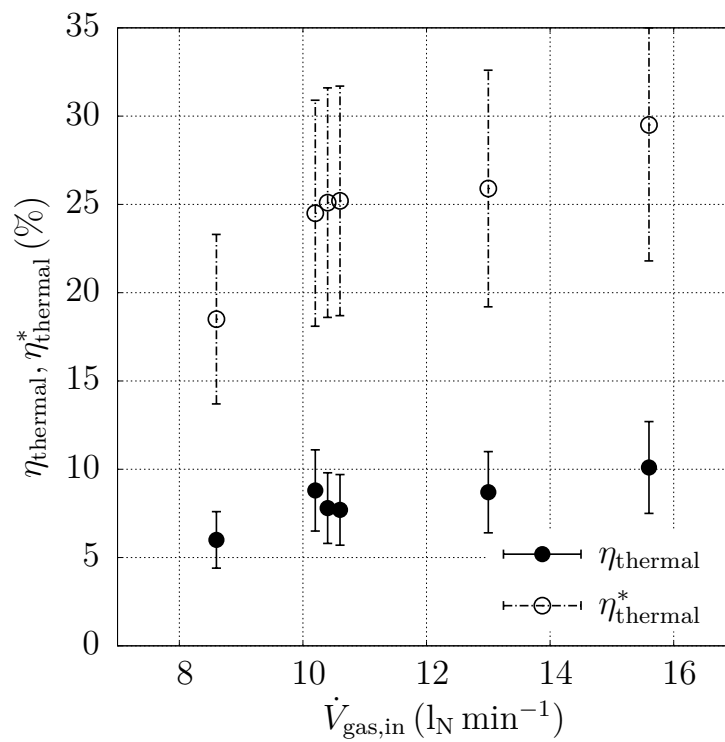


Figure 3.14: Variation of the solar-to-chemical energy conversion efficiency, experimentally obtained ( $\eta_{\text{thermal}}, \bullet$ ) and numerically computed assuming  $\bar{x}_{\text{CH}_4,\text{in}} = 1$  ( $\eta_{\text{thermal}}^*, \circ$ ), as a function of the inlet gas volume flow  $\dot{V}_{\text{g,in}}$ .

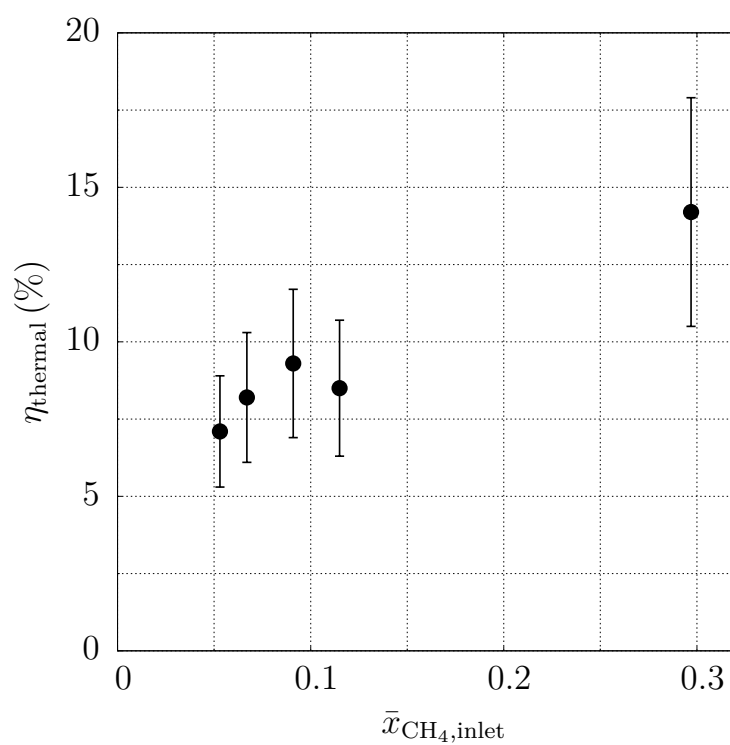


Figure 3.15: Variation of the experimentally obtained solar-to-chemical energy conversion efficiency as a function of the inlet  $\text{CH}_4$  volume fraction  $\bar{x}_{\text{CH}_4, \text{in}}$ .

Carbon type		$d_{p,90,laden}$ $\mu\text{m}$	$d_{p,90,filtered}$ $\mu\text{m}$	$S_{active,BET}$ $\text{m}^2 \text{g}^{-1}$	$V_{micropores}$ $\text{cm}^3 \text{g}^{-1}$
Fluka 05100	AC	116 <sup>a</sup>	26 (run #10) <sup>b</sup>	840.2 <sup>a</sup>	0.22 <sup>b</sup>
Fluka 05120	AC	89 <sup>a</sup>	17 (run #16) <sup>b</sup>	951.8 <sup>a</sup>	0.28 <sup>b</sup>
PAK 800	AC	152 <sup>a</sup>	22 (run #22) <sup>b</sup>	816.3 <sup>a</sup>	0.18 <sup>b</sup>
Merck AC	AC	777 <sup>b</sup>	300 (run #29) <sup>b</sup>	1,140.0 <sup>a</sup>	0.48 <sup>b</sup>
BP 2000	CB	88 <sup>b</sup>	101 (run #44) <sup>b</sup>	1,513.6 <sup>a</sup>	0.24 <sup>b</sup>

<sup>a</sup> Specified by the manufacturer.

<sup>b</sup> Determined experimentally.

Table 3.3: Properties of seed (upstream) and filtered (downstream) active carbon (AC) and carbon black (CB) particles.

### 3.5 Product characterization

Table 3.3 lists the properties of the AC and CB particles both fed (upstream) and filtered (downstream) for selected . They were characterized in terms of particle size distributions (HORIBA LA-950 analyzer),  $\text{N}_2$ -adsorption (Micromeritics 3000), and scanning electron micrography (SEM). Bigger particle sizes negatively affected chemical conversion as a result of the lower specific surface area, as observed in previous studies [101, 124, 79], and of the lower radiation absorption [54, 86]. Measured specific surface area (Tab. 3.3 ) was in the range 815-1,514  $\text{m}^2 \text{g}^{-1}$  for all carbon samples. Microporosity was in the range 0.18-0.48  $\text{m}^2 \text{g}^{-1}$ .

#### 3.5.1 Active carbon

Figure 3.16 shows the SEMs of particle samples collected in the filter downstream for each type of carbon particles laden upstream. For Fluka 05100 (a), an advanced stage of carbon growth process is noticed through the formation of spherical agglomerations of carbon generated by  $\text{CH}_4$  decomposition on the surface of the fed particles, especially on edges and defects that serve as active nucleation sites. In contrast, for Fluka 05120 (b), some spheres have formed on its surface but spherical agglomeration did not occur, presumably because of the larger particle surface available. Similarly, for PAK 800 (c), only a small quantity of deposited carbon is recognized.

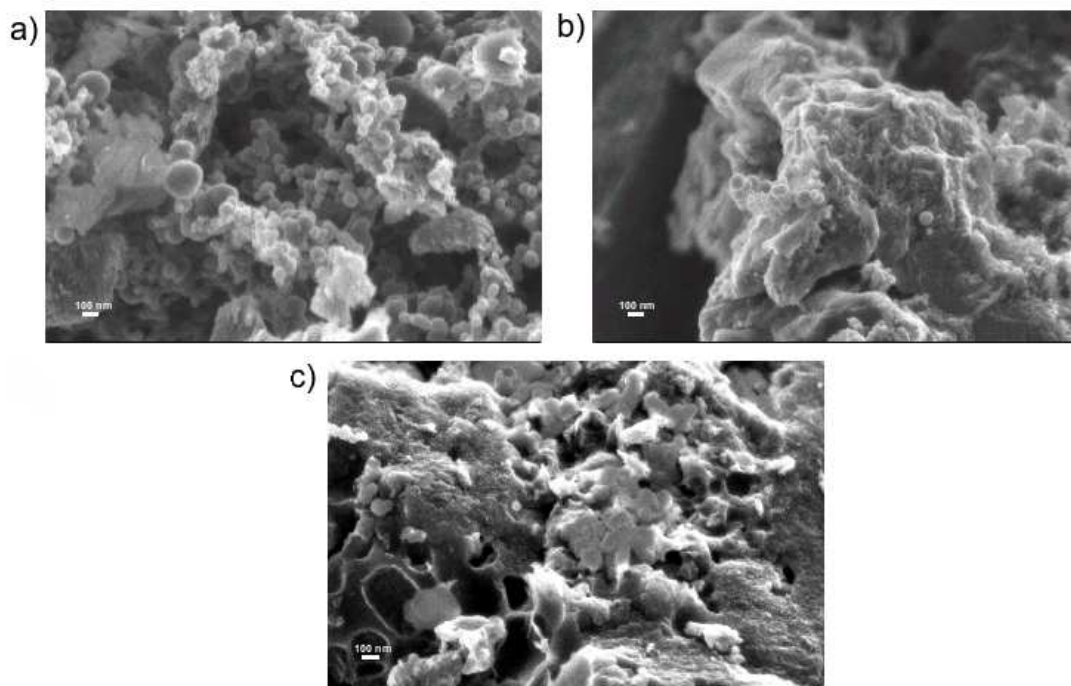


Figure 3.16: SEM of filtered solid products, using laden carbon particles of type: (a) Fluka 05100; (b) Fluka 05120; and (c) PAK 800.

### 3.5.2 Carbon black

Particles resulting from experiments using BP 2000 particles were collected from the filter after experimental runs. Fig. 3.17 shows the probability density  $v_d$  and cumulative  $V_d$  distributions for the seed CB particles (Cabot Black Pearls 2000, see properties in Tab. 3.3) and filtered products after run #44. The seed particles had a bimodal distribution with peaks at 6 and 200 nm due to the presence of particle agglomerates. After the reaction, a shift of both peaks toward higher diameters can be noticed due to particle growth when produced carbon was deposited on the seed particles' surface. Additionally, an increase of the amount of particles having diameter smaller than 2  $\mu\text{m}$  is observed, presumably formed by smaller particles detaching from the bigger agglomerates during their way through the reactor and downstream system. SEM images show that the initially smooth surface of the seed CB particles (Fig. 3.18) was entirely covered by a filamentous agglomerates after the reaction (Fig. 3.19), consisting of primary spherical particles having diameters in the 50-500 nm range (Fig. 3.20). The covering

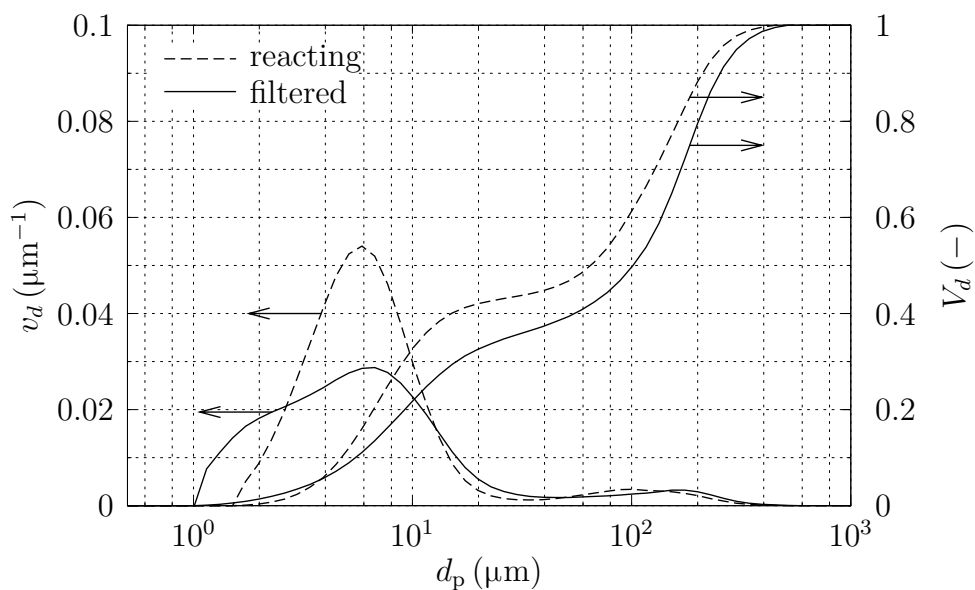


Figure 3.17: Particle volume distribution (probability density  $v_d$  and cumulative  $V_d$ ) for the reacting particles (Cabot Black Pearls 2000 carbon black) and filtered products after run #44.

of the surfaces of the seed CB particles led to blocking of pores and active sites, as indicated by a reduction in the BET specific surface area by 2 orders of magnitude, which impedes particle recirculation. For the BP 2000 sample, the entire raw surface is covered by the deposited carbon generated from  $\text{CH}_4$  decomposition, since the number of active sites and the specific surface area are higher than those for the other particle types. In this case, surface growth progresses in a spherical manner, producing particles of diameters up to 100 mm with spherical agglomerations and protruding ridges, as already observed in previous studies [64].

### 3.6 Summary

An improved design of a 5 kW solar chemical reactor for co-producing  $\text{H}_2$  and C by thermal cracking of  $\text{CH}_4$  was experimentally investigated in a solar simulator and a solar furnace. The seeding of carbon black particles to a continuous flow of  $\text{CH}_4$  proved to enhance the radiative heat transfer and the reaction kinetics. Maximum methane conversion of 98.8 % and hydrogen yield of 99.1 % were reached. The peak solar-to-chemical

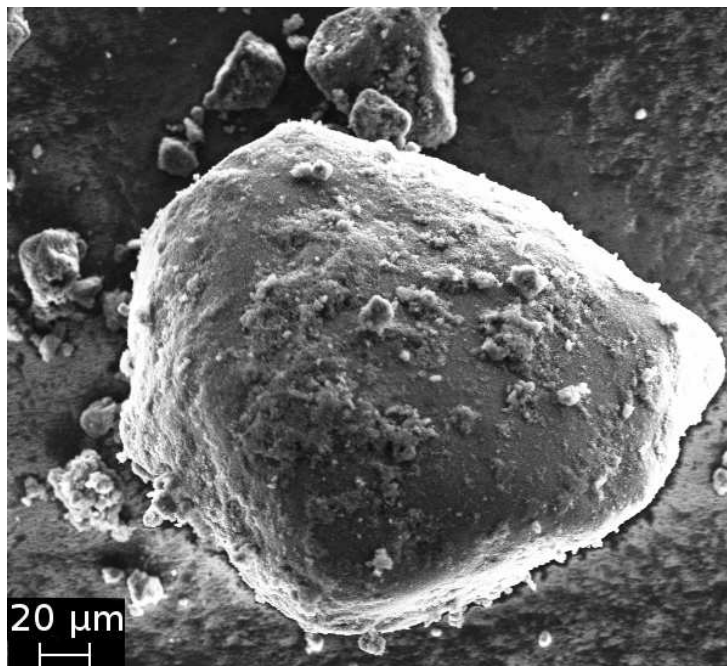


Figure 3.18: SEM images of seed Cabot Black Pearl 2000 carbon black particles.

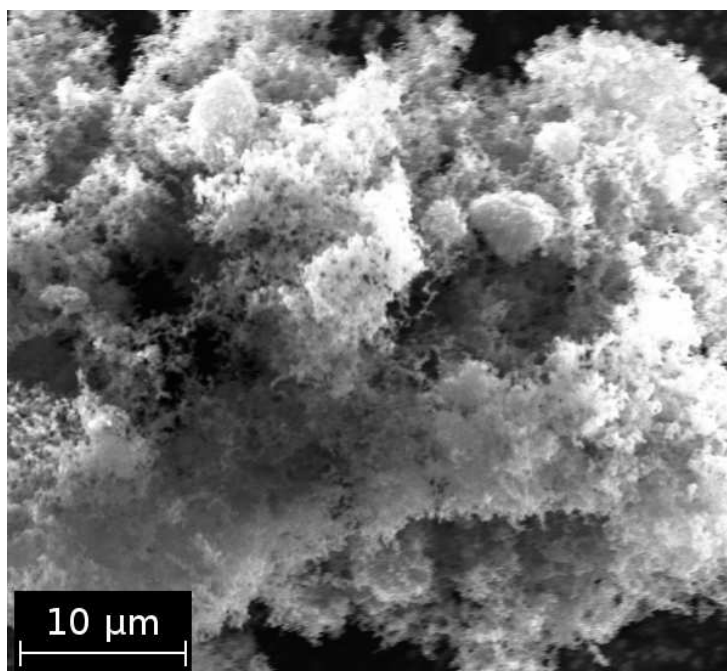


Figure 3.19: SEM images of filtered carbonaceous product after run #44.

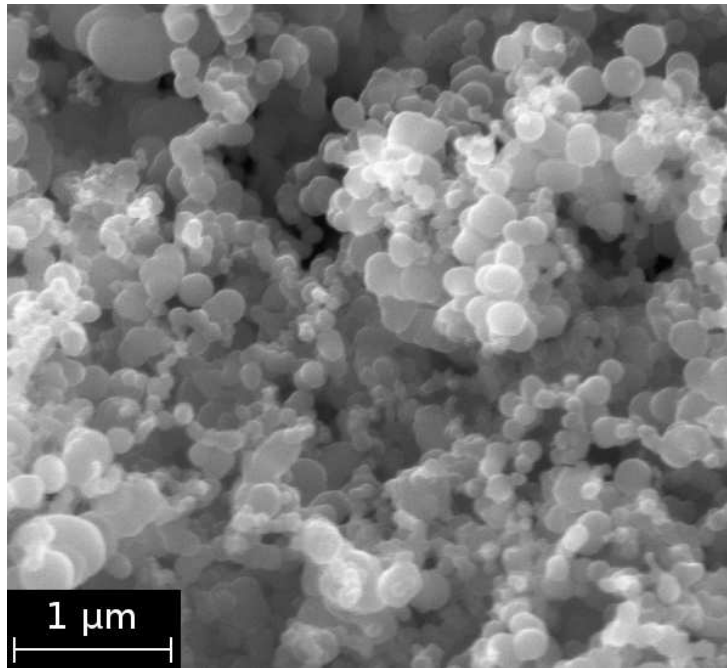


Figure 3.20: SEM images of filtered carbonaceous product after run #44.

energy conversion efficiency was 16.1 %, with an average value of 9.1 %. The parametric study showed an increase of the chemical conversion with particle volume fraction and incoming solar radiative flux as a result of the enhanced radiative absorption by the participating medium. The influence of the injected gas volume flow rate was weak in the considered parametric range, while an increase of  $\text{CH}_4$  molar concentration proved to be counterproductive for the reaction extent due to the higher specific heat of  $\text{CH}_4$ . In contrast, the solar-to-chemical energy conversion efficiency was positively influenced by an increase in the gas volume flow rate and  $\text{CH}_4$  concentration because of the increased rate of heated material in the first case and the higher specific heat of  $\text{CH}_4$  in the second. The SEM images showed deposition of filamentous agglomerates of spherical particles sized 50-500 nm, which covered the porous structure of the seed particles, reducing their BET active surface. Model simulations indicated the possibility of reaching significantly higher energy conversion efficiencies (by a factor 2-4) for the same operational parameters when employing pure  $\text{CH}_4$ .





# Chapter 4

## Scale-up reactor model<sup>1</sup>

### 4.1 Introduction

In this chapter, a numerical model is formulated to simulate the behavior of an indirectly-irradiated solar reactor consisting of a receiver cavity, containing an array of absorber tubes through which the reacting medium flows. Indirectly-irradiated solar reactor concepts proposed for methane cracking feature graphite/ceramic tubes or other opaque surfaces serving as absorbers and heat conductors [3, 4, 29, 30, 115, 116]. Also, solar cavity receivers of this type have been applied for other thermochemical processes, among which are the reduction of metal oxides [92], steam-gasification of carbonaceous materials [91], and steam reforming of methane [81]. In particular, radiative heat transfer has been analyzed for this type of configuration [81, 116].

The presented model couples radiative transfer into and within the cavity-receiver to heat transfer, fluid flow, and chemical kinetics inside the absorber tubes, applying the radiation heat transfer model presented in Chap. 2. Experimental validation is accomplished with a 10 kW reactor prototype. The reactor model is then used to optimize the design for maximum energy conversion efficiency, and to simulate the performance of a 10 MW commercial-scale reactor for a solar tower system.

---

<sup>1</sup>Material from this chapter has been published in: G. Maag, S. Rodat, G. Flamant, and A. Steinfeld. Heat transfer model and scale-up of an entrained-flow solar reactor for the thermal decomposition of methane. *Int. J. Hydrogen Energy*, 35:13232-13241, 2010.

## 4.2 Problem statement

The solar reactor prototype for 10 kW solar power input has been previously described [116]. Its configuration is shown schematically in Fig. 4.1. It consists of a thermally insulated graphite cavity of inner dimensions  $W = H = D = 0.2\text{ m}$ , containing an array of four aligned graphite absorber tubes of outer diameter  $d_{\text{absorber}} = 0.024\text{ m}$  and length  $L_{\text{absorber}} = 0.36\text{ m}$ , 0.16 m of which are inside the cavity, while the rest assumed perfectly insulated (adiabatic). The front face of the cavity has a circular aperture of diameter  $d_{\text{aperture}} = 0.09\text{ m}$ , covered by a single-layer quartz window. The distance between the front plane and the array of absorbers is 0.13 m. Concentrated solar radiation enters the cavity through the windowed aperture, irradiates the absorber tubes and the cavity walls, and undergoes multiple reflections/absorptions. Thermal energy is either absorbed by the medium flowing through the absorber tubes, lost by conduction through the cavity walls, or lost by re-radiated through the aperture.  $\text{CH}_4$ , diluted in Ar at a ratio  $\bar{x}_{\text{CH}_4}$ , is injected into the inner tubes at  $T_{\text{in}}$  and  $p_{\text{in}}$ . Figure 4.2 shows the coaxial counter-flow absorber tube.

## 4.3 Heat transfer modeling

Two coupled models are built for the cavity-receiver and for the absorber tubes. The cavity-receiver model considers the incoming solar power  $Q_{\text{solar}}$  and the net heat sink  $Q_{\text{absorber},j}$  on each absorber tube, and computes the outer surface temperatures  $T_{\text{absorber},j}$  of each absorber tube. These serve as input for the tube model which, given the inlet conditions ( $T_{\text{in}}$ ,  $p_{\text{in}}$ ) and composition ( $\bar{x}_{\text{CH}_4,\text{in}}$ ) of the gas mixture, is used to compute the net absorbed process heat by the fluid in each tube,  $Q_{\text{absorber},j}^*$ . The matching combinations of  $Q_{\text{absorber},j}$  and  $T_{\text{absorber},j}$  are obtained by iteration with convergence criterion

$$\left| 1 - Q_{\text{absorber},j}^*(T_{\text{absorber},j}, T_{\text{in}}, p_{\text{in}}, \bar{x}_{i,\text{in}}) / Q_{\text{absorber},j} \right| \leq 0.001, \quad (4.1)$$

for each surface  $j$ .

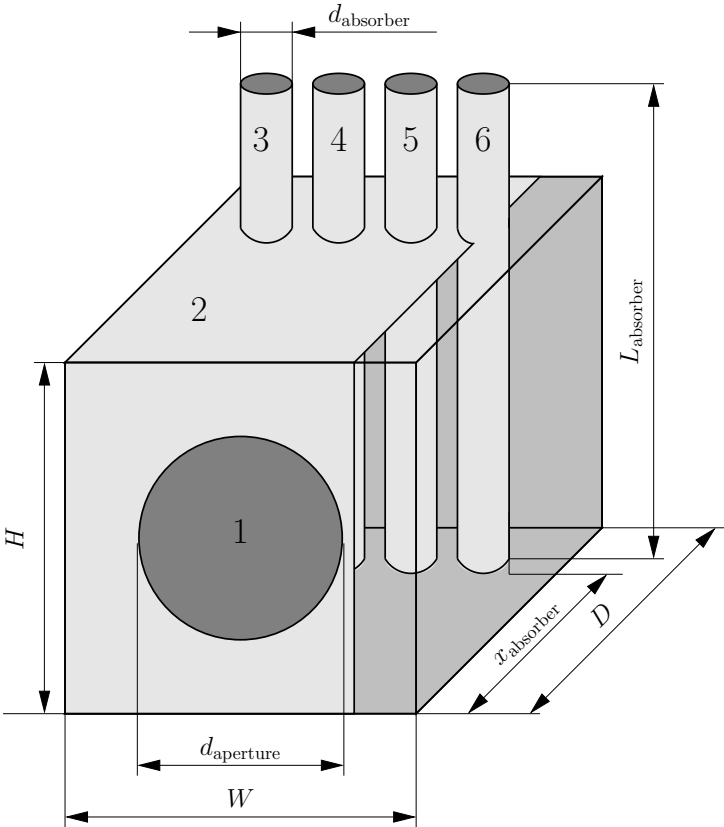


Figure 4.1: Schematic of the solar cavity receiver configuration. 1 = window, 2 = cavity, 3-6 = absorber tubes.

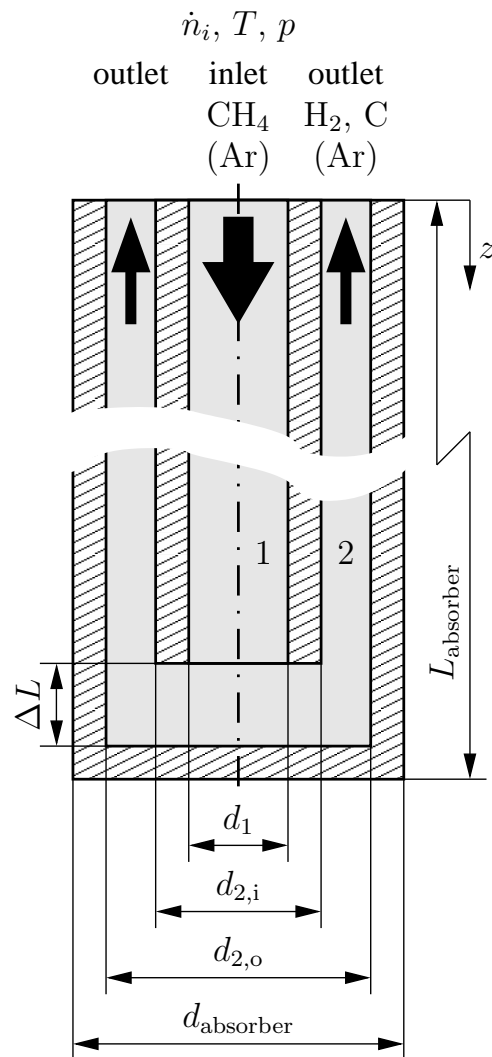


Figure 4.2: Schematic longitudinal section view of an absorber tube.

### 4.3.1 Cavity receiver

Band-approximated spectral optical properties for the quartz window and graphite are shown in Appx. B.1. For graphite, a constant value of  $E = 0.88$  is chosen for the emittance [132].  $Q_{\text{solar}}$  is assumed to have Plancks spectral distribution of a blackbody source at  $T_{\text{source}} = 5,780 \text{ K}$ . Net absorbed process heat is modeled as a heat sink on the absorber surface, whereas the net heat sink on the cavity walls represents conductive losses  $Q_{\text{conduction,wall}}$ . Further assumptions are: diffuse window, opaque-diffuse cavity walls, uniform radiative heat flux, temperature, and properties on both surfaces, as well as no conductive or convective heat transfer between window, cavity, and absorbers. The radiosity method (enclosure theory) for semi-transparent enclosures [132] is applied to obtain a spectral-dependent system of equations in terms of the steady-state temperatures and net radiative fluxes on each surface:

$$\sum_{j=1}^6 \frac{1}{E_{\lambda j,i}} (\delta_{kj} - R_{\lambda j,i} F_{k-j}) \left[ \frac{dq_{\lambda j}}{d\lambda} - E_{\lambda j,o} e_{\lambda b}(T_j) + (1 - R_{\lambda j,o}) \frac{dq_{\lambda e,j}}{d\lambda} \right] = \sum_{j=1}^6 \left( e_{\lambda b}(T_j) + \frac{V_{\lambda j,o}}{E_{\lambda j,i}} \frac{dq_{\lambda j}}{d\lambda} \right) [\delta_{kj} - (1 - V_{\lambda j,i}) F_{k-j}] \quad (4.2)$$

for  $1 \leq k \leq 6$ , ( $1 = \text{window}$ ,  $2 = \text{cavity}$ ,  $3 - 6 = \text{absorber tubes}$ , see Fig. 4.1). where  $q_{e,1} = Q_{\text{solar}}/A_{\text{window}}$ ,  $q_{e,2} = q_{e,3} = q_{e,4} = q_{e,5} = q_{e,6} = 0$ ,  $q_2 = -Q_{\text{conduction,wall}}/A_{\text{wall}}$ , and  $q_j = -Q_{\text{absorber},j}/A_{\text{absorber},j}$ , for  $3 \leq j \leq 6$ . Subscripts i and o denote inner and outer properties of the boundary walls, respectively. Neglecting external emission at the walls and absorber tubes,  $\{E_{1,o}; R_{1,o}; V_{1,o}\} = \{E_{1,i}; R_{1,i}; V_{1,i}\}$ , and  $E_{j,o} = R_{j,o} = V_{j,o} = V_{j,i} = 0$ , for  $2 \leq j \leq 6$ . The view factor matrix  $\mathbf{F}$  between the faces is obtained by Monte Carlo ray-tracing code. The system of equations (4.2) is integrated over the windows three spectral bands  $l$  to yield a system of  $6 \times 3$  spectrally-independent equations for totally  $6 \times (3 + 1)$  unknowns  $(q_{jl}, T_{jl})$ . The remaining six equations are obtained from the relationship  $q_j = \sum_{l=1}^3 q_{jl}$ , for  $1 \leq j \leq 6$ . The incoming radiation heat flux per spectral band  $l$  for each

face is  $q_{e,jl} = \frac{q_{e,j}}{\sigma T_{sun}^4} \int_{\lambda_{1,l}}^{\lambda_{2,l}} e_{b\lambda}(\lambda, T_{sun}) d\lambda$ . Since the total (spectrally-integrated) optical properties of the window and the walls are influenced by their temperatures  $T_j$ , their value has to be determined iteratively. Conductive losses through the cavity walls are approximated by applying Fourier's Law:

$$q_2 = \frac{Q_{\text{conduction,wall}}}{A_{\text{wall}}} = \frac{(UA)_{\text{insulation}}}{A_{\text{wall}}} (T_{\text{wall}} - T_{\text{ambient}}), \quad (4.3)$$

where  $T_{\text{ambient}} = 298.15 \text{ K}$  and  $(UA)_{\text{insulation}}$  is the overall heat transfer coefficient between the inner cavity wall and the surroundings. For the 10 kW prototype,  $(UA)_{\text{insulation}} = 1.14 \cdot 10^{-3} \text{ W K}^{-1} \pm 11 \%$ .

### 4.3.2 Absorber tubes

All three heat transfer modes between and through tube walls and gas-particle flows are considered. For conduction,

$$q_{\text{conduction},j}(z) = \frac{2\pi k_{\text{absorber}} [T_{j,o} - T_{j,i}(z)]}{\ln(d_{j,o}/d_{j,i})} \quad (4.4)$$

where  $j = \{1, 2\}$  denotes the inner and outer graphite tube, respectively. A typical value for graphite  $k_{\text{absorber}} = 50 \text{ W m}^{-1} \text{ K}^{-1}$  was chosen [1], which results in a difference between inner and outer surface temperature lower than 10 K. For the outer tube,  $T_{\text{absorber},o}$  is assumed to be constant over the entire surface. Convective heat transfer in the inner tube is given by [58]: for laminar flow:

$$\text{Nu}_1(z) = 3.66, \quad (4.5)$$

for turbulent flow:

$$\text{Nu}_1(z) = 0.023 \text{Re}_1(z)^{0.8} \text{Pr}(z)^{0.4}, \quad (4.6)$$

with  $\text{Re}_1(z) = [\rho_1(z) w_1(z) d_1] / \mu_1(z)$ ,  $\text{Pr}_1(z) = [\bar{c}_{p,1}(z) \mu_1(z)] / k_1(z)$ , and  $\text{Nu}_1(z) = [\alpha_1(z) d_1(z)] / k_1(z)$ . For transitional flow ( $2,300 \leq \text{Re} \leq 10,000$ ), Nu is obtained by linear interpolation between the two cases. In the outer annular gap, both convection from the outer tube to the fluid as well as from the fluid to the inner tube are considered. Laminar-flow Nu numbers for constant surface temperatures were shown to be function

of the diameter ratio  $\tilde{d} = d_{2,i}/d_{2,o}$  [129] of the annulus. Convective heat transfer coefficients are then:

- for the inner annulus wall:

$$\alpha_{2,i}(z) = \frac{\text{Nu}_{2,i}k_2(z)}{d_{2,h}}, \quad (4.7)$$

- for the outer annulus wall:

$$\alpha_{2,o}(z) = \frac{\text{Nu}_{2,o}k_2(z)}{d_{2,h}}, \quad (4.8)$$

with the hydrodynamic diameter  $d_{2,h} = d_{2,o} - d_{2,i}$ . For the considered parameter range, no turbulence is achieved in the annulus. The convective heat fluxes are then:

- for the inner tube:

$$q_{1,\text{convection}}(z) = \alpha_1(z) [T_1(z) - T_{1,\text{bulk}}(z)], \quad (4.9)$$

- for the inner annulus wall:

$$q_{2,i,\text{convection}}(z) = \alpha_{2,i}(z) [T_{2,\text{bulk}}(z) - T_{2,i}(z)], \quad (4.10)$$

- for the outer annulus wall:

$$q_{2,o,\text{convection}}(z) = \alpha_{2,o}(z) [T_{2,o}(z) - T_{2,\text{bulk}}(z)], \quad (4.11)$$

Determination of thermochemical properties of the gas mixture (Ar, CH<sub>4</sub>, H<sub>2</sub>) is described in Appx. C.

Radiative heat exchange between the tube walls and the carbon particles in the reacting flow is treated by the collision-based Monte Carlo model presented in Sec. 2, applying cylindrical boundary conditions to simulate absorber tube walls. The contribution of the gas phase is neglected since accounts for less than 5 % of the total radiative heat flux, as shown by applying the line-by-line model to the molecular spectroscopic database HITRAN-2004 [122] and in [24]. The radiative flux divergence is given by [41]

$$\frac{\partial Q_{r,\lambda}}{\partial V} d\lambda = \nabla \cdot \mathbf{q}_{r,\lambda} d\lambda = 4\kappa_P \sigma T^4 \frac{\sum_k Q_{\text{ray},k} \kappa_\lambda ds_k}{2\pi r dr dz}, \quad (4.12)$$

where  $k$  designates a generic stochastic ray traversing in 3D the path length within sub-element of volume  $dV$  and carrying a portion of radiative flux

$$Q_{\text{ray},k} = \left( Q_e + 4\sigma \int_0^{L_{\text{absorber}}} \int_0^{r_{\text{absorber},i}} \kappa_P T^4 2\pi r dr dz \right) N_{\text{rays}}^{-1}. \quad (4.13)$$

The path length  $s$  to a scattering event is calculated from:

$$\ln \mathcal{R}_s = - \int_0^s \sigma_{\text{sca},\lambda}(s) ds, \quad (4.14)$$

where  $\mathcal{R}_s$  is a random number chosen from a uniform distribution set between 0 and 1, and the right hand side of Eq. (4.14) represents the probabilistic cumulative distribution function for scattering by particles. Similarly, the wavelength and direction of emission and direction of scattering can be calculated using the corresponding cumulative distribution functions. Radiative properties of the biochar particles are calculated by assuming independent scattering and the refractive index of the gas phase to be equal to unity [144]. The absorption, scattering, and extinction coefficients and the scattering phase function are obtained by applying the Mie theory [19] for an expected  $d_{32} = 50$  nm based on the complex refractive index of the particle approximated by that of propane soot [20, 32]. For a given  $d_{32}$ , simulation results for the radiative heat flux between the inner tube wall and the medium could be reasonably well approximated in the range of interest by:

$$q_{\text{radiation}} = (af_V^2 + bf_V + c) (T_{\text{wall}}^4 - T_{\text{bulk}}^4), \quad (4.15)$$

where the parameters  $(a, b, c)$  are obtained by least-square fitting to the data points produced using the MC model (Sec. 2). This procedure was carried out for each radiative heat flux:  $q_{1,\text{radiation}}$ ,  $q_{2,\text{i,radiation}}$ ,  $q_{2,\text{o,radiation}}$ , and  $q_{2,\text{radiation}}$  to obtain the parameters listed in Tab. 4.1 for all geometrical absorber tube arrangements used in the experiments.

The steady-state 1D mass conservation equation is formulated for each component  $i$ :

$$\frac{\partial \bar{\rho}_i}{\partial t} = 0 = - \frac{\partial}{\partial z} (\bar{\rho}_i w) + \bar{r}_i. \quad (4.16)$$



		$a$	$b$	$c$
		$\text{W m}^{-2} \text{K}^{-4}$	$\text{W m}^{-2} \text{K}^{-4}$	$\text{W m}^{-2} \text{K}^{-4}$
$q_{1,\text{radiation}}$	$d_1 = 4 \text{ mm}$	-4.23	$6.61 \cdot 10^{-4}$	0
	$d_1 = 7 \text{ mm}$	-8.41	$1.03 \cdot 10^{-3}$	0
	$d_1 = 8 \text{ mm}$	-10.67	$1.23 \cdot 10^{-3}$	0
$q_{2i,\text{radiation}}$	$d_{2o} - d_{2i} = 6 \text{ mm}$	-3.69	$5.17 \cdot 10^{-4}$	0
	$d_{2o} - d_{2i} = 8 \text{ mm}$	-4.20	$5.37 \cdot 10^{-4}$	0
	$d_{2o} - d_{2i} = 9 \text{ mm}$	-2.97	$6.23 \cdot 10^{-4}$	0
$q_{2,\text{radiation}}$	$d_{2o} - d_{2i} = 6 \text{ mm}$	2.76	$-4.46 \cdot 10^{-4}$	$3.07 \cdot 10^{-8}$
	$d_{2o} - d_{2i} = 8 \text{ mm}$	3.13	$-4.44 \cdot 10^{-4}$	$2.53 \cdot 10^{-8}$
	$d_{2o} - d_{2i} = 9 \text{ mm}$	3.12	$-4.33 \cdot 10^{-4}$	$2.31 \cdot 10^{-8}$
$q_{2o,\text{radiation}}$	$d_{2o} - d_{2i} = 6 \text{ mm}$	-9.21	$1.07 \cdot 10^{-3}$	0
	$d_{2o} - d_{2i} = 8 \text{ mm}$	-12.23	$1.28 \cdot 10^{-3}$	0
	$d_{2o} - d_{2i} = 9 \text{ mm}$	-13.07	$1.29 \cdot 10^{-3}$	0

Table 4.1: Coefficients  $a$ ,  $b$ , and  $c$  determined by least-square fitting of a second-order polynomial function to simulated radiative heat transfer rates, obtained with MC for the inner absorber tube geometries used during experimentation.

with  $w$  being the flow velocity in the axial direction. The boundary condition at inlet with no particle feeding is  $\bar{\rho}_{1,i}(z=0) = \bar{x}_{\text{in},i} p_{\text{in}} / \bar{R} T_{\text{in}}$ . The particle volume fraction, necessary for the determination of the radiative transfer rates, is given by  $f_V = \bar{\rho}_p \bar{M}_C / \rho_{\text{cb}}$ . For the particle density, a typical value for carbon black,  $\rho_{\text{CB}} = 1,800 \text{ kg m}^{-3}$ , is chosen. The reaction kinetic model is explained in Appx. D. Assuming plug flow and ideal gas while neglecting the volume of the solid phase ( $f_V < 5 \cdot 10^{-5}$ ) and the pressure drop ( $< 1\%$  across the entire system),  $\dot{V}_g = wA = \dot{n}_g \bar{R} T_{\text{bulk}} / p$ . Deriving with respect to axial distance  $z$  yields the infinitesimal flow velocity change:

$$\frac{dw}{dz} = \frac{\bar{R} T_{\text{bulk}}}{p} \sum_j \sum_i \nu_{ij} r_j + \frac{w}{T_{\text{bulk}}} \frac{dT_{\text{bulk}}}{dz}. \quad (4.17)$$

The first right-hand term accounts for gas moles being produced by all chemical reactions while the second term considers thermal gas expansion. Boundary condition at inlet is  $w(z=0) = w_{\text{in}} = \dot{V}_{g,\text{in}} / A$ . The steady-state 1D energy conservation equation is formulated for the inner tube,

$$\frac{\partial}{\partial t} \left( \sum (\bar{\rho}_i \bar{h}_i) \right) = \frac{\partial}{\partial z} (\bar{\rho}_i w \bar{h}_i) + \frac{\partial q_{1,\text{conduction}}}{\partial z} + \sum_j \nu_{\text{reactant},j} \bar{r}_j \Delta \bar{h}_{R,j}, \quad (4.18)$$

and the outer annulus

$$\frac{\partial}{\partial t} \left( \sum (\bar{\rho}_i \bar{h}_i) \right) = \frac{\partial}{\partial z} (\bar{\rho}_i w \bar{h}_i) + \frac{\partial}{\partial z} (q_{2,\text{conduction}} - q_{1,\text{conduction}}) + \sum_j \nu_{\text{reactant},j} \bar{r}_j \Delta \bar{h}_{R,j}, \quad (4.19)$$

with  $q_{1,\text{conduction}}$  and  $q_{2,\text{conduction}}$  denoting heat conducted through the inner and outer tube wall, respectively. The initial condition is:  $T_1(z=0) = T_{\text{in}} = T_{\text{ambient}}$ . For each variable  $\phi = \{\dot{n}_i; T_{\text{bulk}}\}$ , the relationship  $\phi_2(L_{\text{absorber}}) = \phi_1(L_{\text{absorber}})$  is valid. Equations (4.16), and (4.17)-(4.19) are discretized in space and solved using the finite volume method [42].

## 4.4 Experimental validation

The model is validated by comparing its results to those obtained experimentally using a 10 kW<sub>th</sub> solar reactor prototype tested in the 1-MW solar

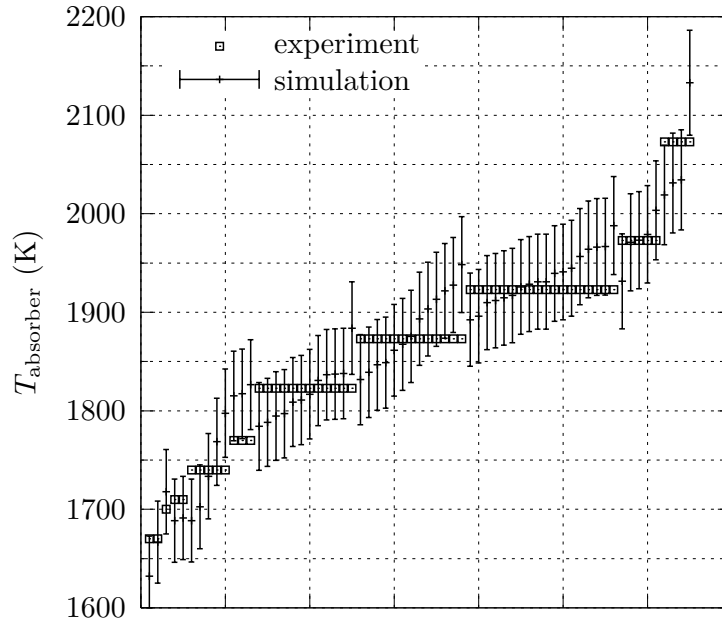


Figure 4.3: Experimentally measured and model simulated outer absorber tube temperature for 65 solar experimental runs with the 10 kW solar reactor prototype (ordered by increasing  $T_{\text{absorber,o}}$ ).

furnace of the CNRS-PROMES laboratory [147]. Figure 4.3 shows the experimentally measured (by pyrometry) and model simulated outer absorber tube temperature for all experimental runs in order of increasing  $T_{\text{absorber,o}}$ . The relative error distribution shows a standard deviation of 1.7 %. The sources of uncertainty are thermal transients in the cavity insulation and the natural unsteadiness of solar power input  $Q_{\text{solar}}$ . To account for these, an uncertainty of  $\pm 2\%$  for  $Q_{\text{conduction,wall}}$  and of  $\pm 5\%$  for  $Q_{\text{solar}}$  are assumed. Figure 4.4 shows the measured (by gas chromatography) and model simulated  $\text{H}_2$  concentration in the off gas, using a  $\text{CH}_4$ -Ar mixture as reactants. The standard deviation of relative errors is 29.1 %. The uncertainty of the simulated values stems principally from variations in system pressure and tube diameter due to carbon depositions. For example, the residence time can vary by up to 40 % and the system pressure can vary by up to 2.5 % for a 1-mm-thick carbon deposition in the tube inner walls.

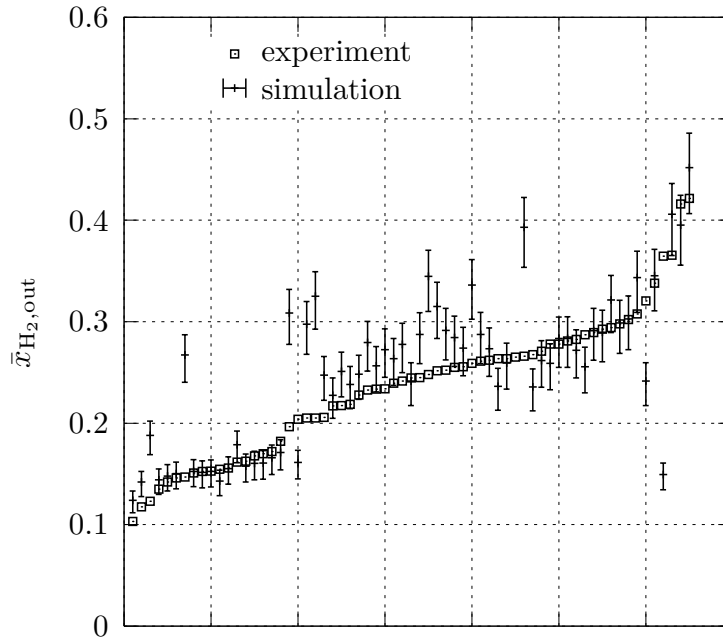


Figure 4.4: Experimentally measured and model simulated  $\text{H}_2$  concentration at the outlet for 65 solar experimental runs with the 10 kW solar reactor prototype (ordered by increasing  $\bar{x}_{\text{CH}_4,\text{out}}$ ).

## 4.5 Scale-up to 10 MW<sub>th</sub>

An industrial-scale solar reactor mounted on a solar tower system is considered. A schematic of the optimized cavity-receiver shape is shown in Fig. 4.5. Cavity optimization is more detailedly explained in Appendix E. It has seven apertures and contains an array of 26 (central receiver) or 20 (lateral receiver) tubular absorbers. Viewed from the top, the cavity has the shape of a circular section having chord length  $W$  and height  $D$ . Each absorber tube of diameter  $d_{\text{absorber},o}$  is positioned at a 1 cm gap to the adjacent one and to the wall. Secondary concentrators (CPC [155]) are incorporated at the apertures to obtain radiative flux intensities above  $3 \text{ MW m}^{-2}$  (3,000 suns). Due to the limited acceptance angle of the CPCs, a system of three cavity-receivers is considered, each one facing a dedicated part of the heliostat field as shown in Fig. 4.6. Dimensions resulting from the cavity optimization for a total  $Q_{\text{solar}} = 10 \text{ MW}$  are listed in Tab. 4.2 and differ for the central (North) and the two lateral (East/West) solar cavity-receivers due to the different incident solar heat fluxes. The absorber

dimension	unit	cavity	
		North	East/West
$D$	m	2.0	1.2
$H$	m	4.0	4.0
$W$	m	4.0	3.0
$N_{\text{absorbers}}$		26	20
$d_{\text{absorber,o}}$	m	0.14	0.14
$d_{\text{absorber,i}}$	m	0.08	0.08
$\delta$	m	0.15	0.15

Table 4.2: Optimized dimensions of the scale-up cavity-receivers.

tube geometry is simplified by removing the inner tube for a single-pass configuration.

Two performance indicators of the system are applied. The thermal energy conversion efficiency is defined as:

$$\eta_{\text{thermal}} = \frac{Q_{\text{thermal}} + Q_{\text{chemical}}}{Q_{\text{solar}}}, \quad (4.20)$$

The chemical energy conversion efficiency is defined as:

$$\eta_{\text{chemical}} = \frac{Q_{\text{chemical}}}{Q_{\text{solar}}}, \quad (4.21)$$

with  $Q_{\text{thermal}} = \sum_i \int_{T_{\text{in}}}^{T_{\text{out}}} \dot{n}_{i,\text{in}} \bar{c}_{p,i}(T) dT$  being the power supplied for heating up the injected gases  $i$  and  $Q_{\text{chemical}} = \sum_i \dot{n}_{i,\text{out}} \bar{h}_i(T_{\text{out}}) - \sum_i \dot{n}_{i,\text{in}} \bar{h}_i(T_{\text{in}})$  the sum of reaction enthalpies for all four considered chemical reactions, assuming all transformations happen at  $T_{\text{out}}$ . The performance of the three cavity-receivers is simulated over the relevant range of operational conditions, assuming pure CH<sub>4</sub> inlet flow pre-heated to 1,173 K. Figure 4.7 shows the outlet gas temperature  $T_{\text{out}}$  as a function of inlet CH<sub>4</sub> mass flow rate  $\dot{m}_{\text{CH}_4,\text{in}}$  and the incoming solar radiative flux through the apertures  $q_{\text{solar}}$  for the North (Fig. 4.7a) and the East/West (Fig. 4.7b) cavity-receivers. At design point (equinox, noon),  $Q_{\text{solar, North}} = 3,946 \text{ kW}$ ,  $Q_{\text{solar, East}} = 3,544 \text{ kW}$ ,  $Q_{\text{solar, West}} = 3,544 \text{ kW}$ , and the desired  $T_{\text{out}} = 1,870 \text{ K}$  is reached for  $\dot{m}_{\text{CH}_4,\text{in, North}} = 0.254 \text{ kg s}^{-1}$  and  $\dot{m}_{\text{CH}_4,\text{in, East}} = \dot{m}_{\text{CH}_4,\text{in, West}} = 0.221 \text{ kg s}^{-1}$ ,

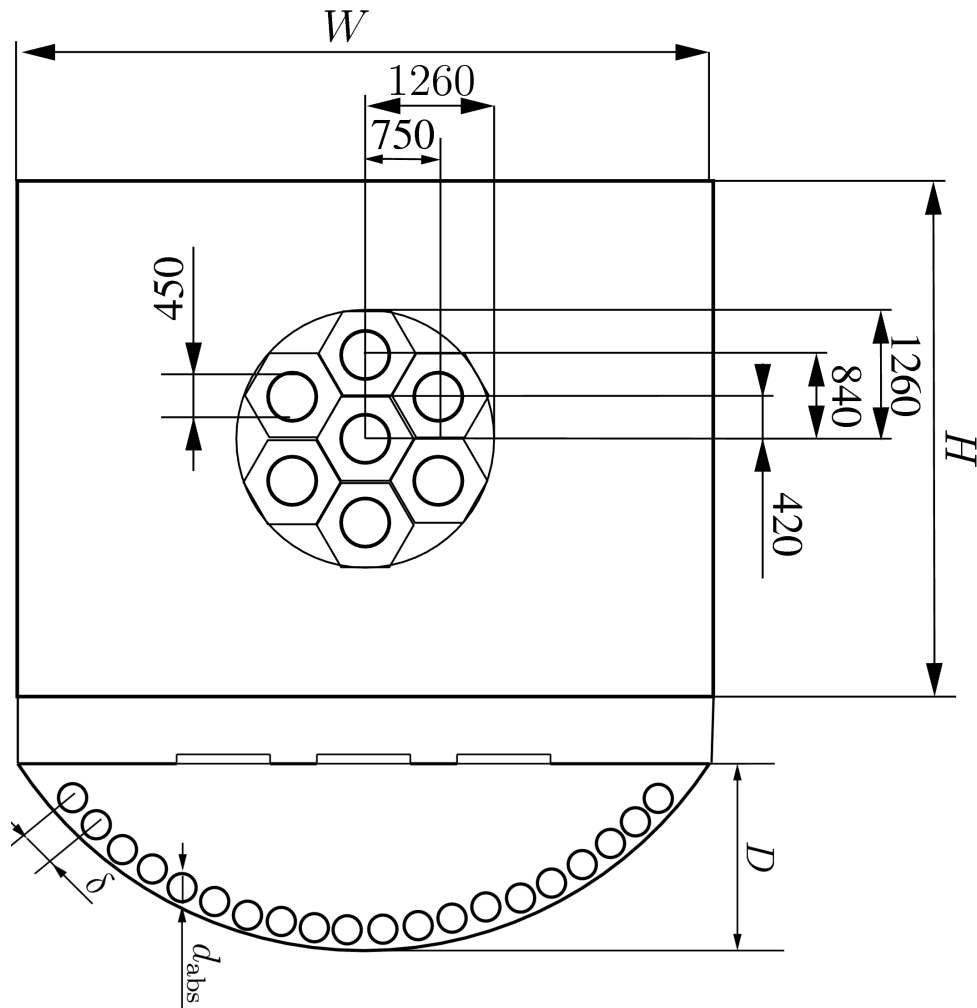


Figure 4.5: Front and top view of the 10 MW solar reactor, consisting of a cavity-receiver with seven apertures, each having a hexagonal CPC, and containing an array of 26 (North) or 20 (East/West) tubular absorbers (dimensions in mm).

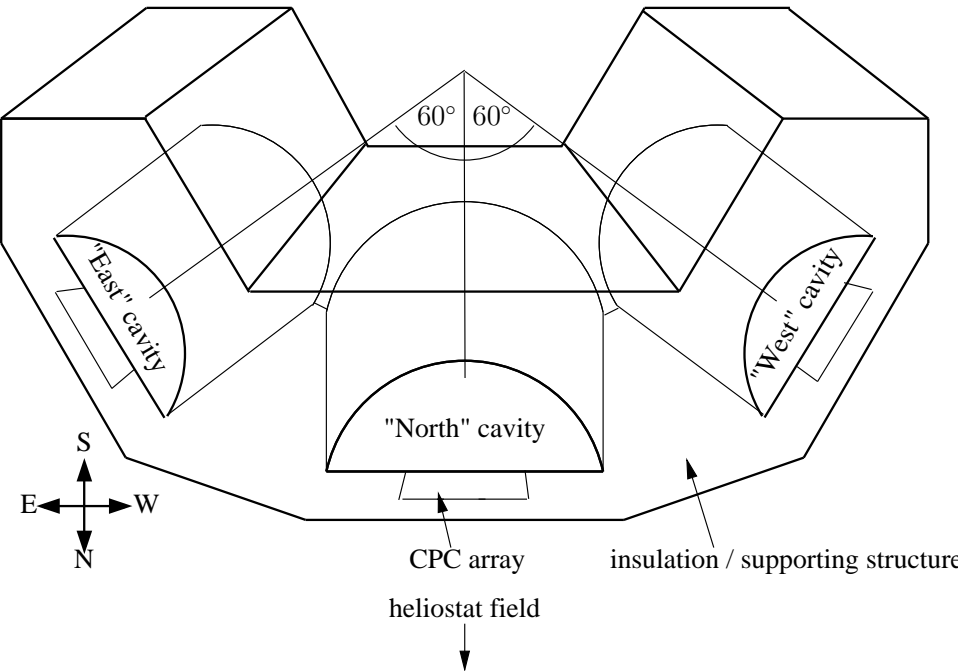


Figure 4.6: Top view of the three cavity-receivers, each one facing its dedicated portion of the heliostat field (North, East, and West), positioned at an angle of 60° from each other to allow efficient capturing of the incoming concentrated solar radiation by the CPCs.

totaling  $0.696 \text{ kg s}^{-1}$ . At this outlet temperature, over 99 % conversion of  $\text{CH}_4$  is achieved. Figures 4.8 and 4.9 show  $\eta_{\text{thermal}}$  and  $\eta_{\text{chemical}}$ , respectively, as a function of  $\dot{m}_{\text{CH}_4, \text{in}}$  and  $q_{\text{solar}}$  for the North (a) and East/West (b) scale-up cavity-receivers. While the operating conditions at design point are close to the optimum value for  $\eta_{\text{thermal}}$ , only about 2/3 of the optimum value can be reached for  $\eta_{\text{chemical}}$ . Higher  $\eta_{\text{chemical}}$  is possible by means of an increase in  $\dot{m}_{\text{CH}_4, \text{in}}$ . However, this would result in a lower  $T_{\text{out}}$  and, consequently, in a significantly reduced chemical conversion. To avoid the latter,  $L_{\text{absorber}}$  can be increased for longer residence times but at the expense of higher conduction losses through the cavity walls. Finally, Figure 4.10 shows  $\eta_{\text{chemical}}$  as a function of  $T_{\text{out}}$  for the North scale-up cavity-receiver. The parameters are  $q_{\text{solar}} = 0.6, 1.2, 1.8, 2.4, 3.0,$  and  $3.6 \text{ MW m}^{-2}$ , and  $\dot{m}_{\text{CH}_4, \text{in}} = 0.08, 0.14, 0.20,$  and  $0.26 \text{ kg s}^{-1}$ .  $\eta_{\text{chemical}}$  increases from 43 % to over 60 %, and  $\eta_{\text{thermal}}$  from 75 % to over 80 %, when  $T_{\text{out}}$  is reduced from 1,870 K to 1,600 K, but at the expense of an inferior CB quality and incomplete  $\text{CH}_4$  conversion.

## 4.6 Summary

A heat transfer model was developed to simulate a solar chemical reactor for thermally cracking natural gas. The model couples radiative heat transfer within the cavity-receiver with radiation/convection/conduction heat transfer for a reacting flow inside the absorber tubes. Experimentally validation was carried out with a 10 kW solar reactor prototype. For 65 solar experimental runs, the standard deviation of relative errors between measured and simulated outer absorber tube temperatures was 1.7 % and the one between measured and simulated  $\text{H}_2$  concentrations at the outlet was 29.1 %. The validated model was applied to optimize the design and estimate the performance of a 10 MW scale-up reactor for a solar tower system. At design point, a maximum methane mass flow of approximately  $0.75 \text{ kg s}^{-1}$  can be completely reacted for a desired outlet temperature of 1,870 K, yielding a solar-to-chemical energy conversion efficiency of 42 %. If lowered to 1,600 K, the reacted mass flow rate doubles and the efficiency rises to more than 60 %, but at the expense of an inferior carbon black quality.



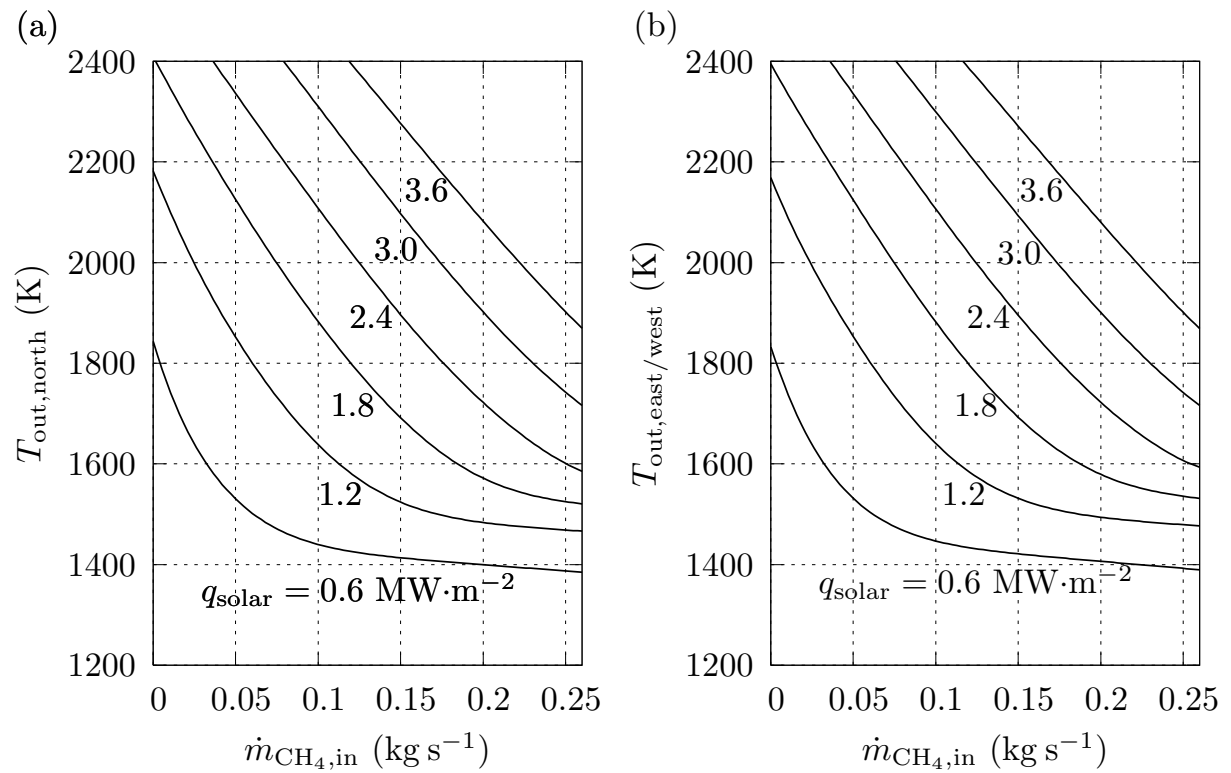


Figure 4.7: Variation of the outlet gas temperature  $T_{\text{out}}$  with inlet  $\text{CH}_4$  mass flow rate  $\dot{m}_{\text{CH}_4,\text{in}}$  for the North (a) and East/West (b) scale-up cavity-receivers. The parameter is the solar radiative flux through the reactor aperture  $q_{\text{solar}} = 0.6, 1.2, 1.8, 2.4, 3.0,$  and  $3.6 \text{ MW m}^{-2}$ .

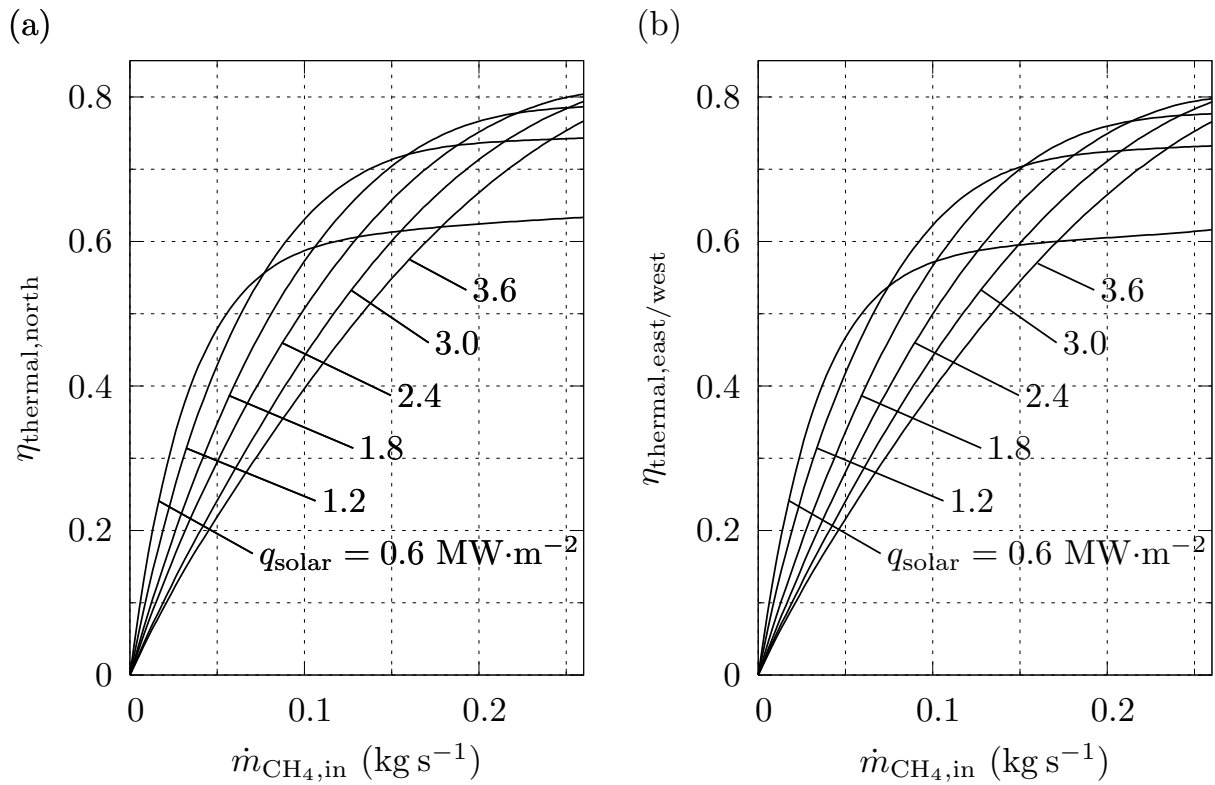


Figure 4.8: Variation of the thermal energy conversion efficiency  $\eta_{\text{thermal}}$  as a function of the inlet  $\text{CH}_4$  mass flow rate  $\dot{m}_{\text{CH}_4,\text{in}}$  for the North (a) and East/West (b) scale-up cavity-receivers. The parameter is the solar radiative flux through the reactor aperture  $q_{\text{solar}} = 0.6, 1.2, 1.8, 2.4, 3.0,$  and  $3.6 \text{ MW m}^{-2}$ .

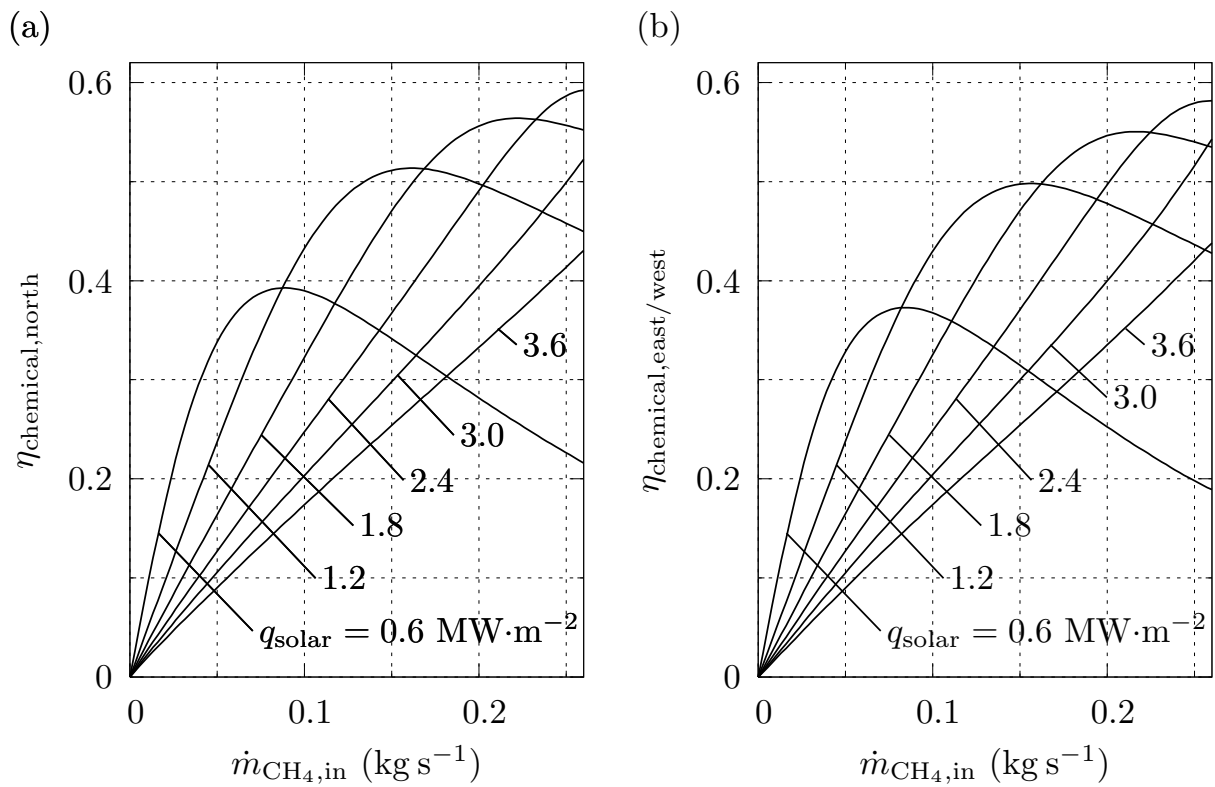


Figure 4.9: Variation of the thermal energy conversion efficiency  $\eta_{\text{chemical}}$  as a function of the inlet  $\text{CH}_4$  mass flow rate  $\dot{m}_{\text{CH}_4,\text{in}}$  for the North (a) and East/West (b) scale-up cavity-receivers. The parameter is the solar radiative flux through the reactor aperture  $q_{\text{solar}} = 0.6, 1.2, 1.8, 2.4, 3.0,$  and  $3.6 \text{ MW m}^{-2}$ .

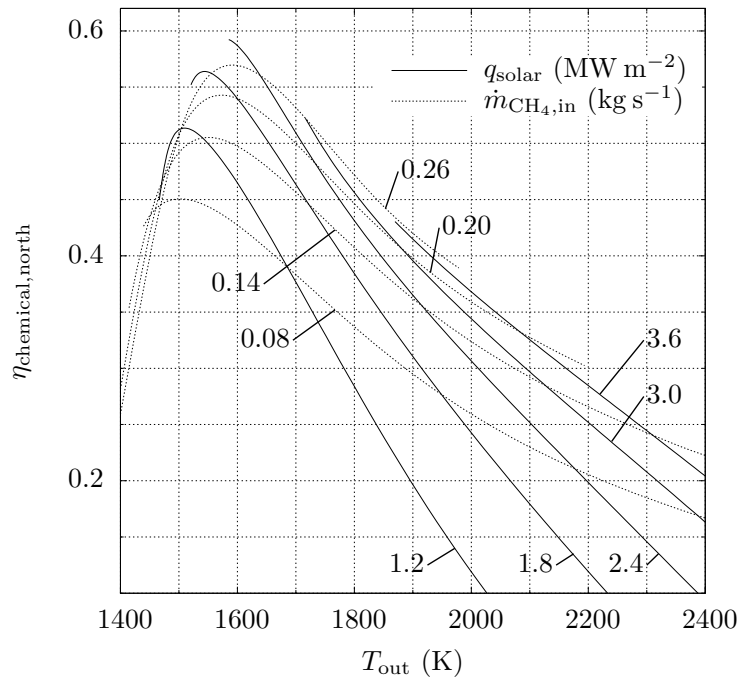


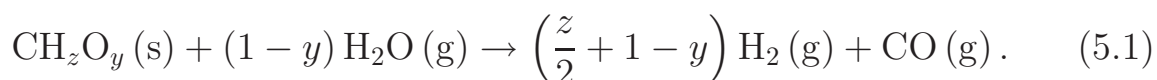
Figure 4.10: Variation of the chemical energy conversion efficiency  $\eta_{\text{chemical}}$  as a function of outlet gas temperature  $T_{\text{out}}$  for the North scale-up cavity-receivers. The parameter are the solar radiative flux through the reactor aperture  $q_{\text{solar}} = 1.2, 1.8, 2.4, 3.0,$  and  $3.6 \text{ MW m}^{-2}$ , and the inlet  $\text{CH}_4$  mass flow  $\dot{m}_{\text{CH}_4,\text{in}} = 0.08, 0.14, 0.20,$  and  $0.26 \text{ kg s}^{-1}$ .

# Chapter 5

## Biochar gasification<sup>1</sup>

### 5.1 Introduction

To prove the validity of the numerical model presented in Chap. 4 and to demonstrate its versatility for different types of solar chemical processes, in this chapter it is applied to steam-gasification of carbonaceous materials. The reaction product is synthesis gas (syngas), a mixture of mainly H<sub>2</sub> and CO that can be used for power generation in efficient combined cycles and fuel cells [135, 160], or further processed to liquid fuels via Fischer-Tropsch or other catalytic reforming processes [121, 158]. The simplified net reaction can be represented by:



Mineral matter, intrinsic water content, and other impurities contained in the feedstock are omitted from consideration in Eq. (5.1). Their presence may have an effect on the kinetics and final product composition, but their exclusion does not affect the main conclusions of this analysis. Autothermal gasification requires approximately 35 % of the injected feedstock to be combusted to supply the high-temperature process heat required to drive the endothermic reaction (5.1) [109], which results inherently in low feedstock utilization, the necessity of an air-separation unit for pure O<sub>2</sub> stream, and the contamination of the off-gas with combustion byproducts. The use of concentrated solar energy as the source of high-temperature

---

<sup>1</sup>Material from this chapter has been published in: G. Maag, and A. Steinfeld. Design of a 10 MW particle-flow reactor for syngas production by steam-gasification of carbonaceous feedstock using concentrated solar energy. *Energy Fuels*, 24:6540-6547, 2010.

process heat can eliminate these drawbacks [152]. It produces high-quality syngas with higher output per unit of feedstock. It further upgrades the calorific value of the feedstock by an amount equal to the enthalpy change of reaction, theoretically, by up to 45 % resulting in a significant reduction of CO<sub>2</sub> emissions vis-a-vis conventional autothermal gasifiers [67]. A 2<sup>nd</sup>-Law (exergy) analysis indicates that combined Brayton-Rankine power cycles running on solar-made syngas from coal can double the specific electric output per unit mass of coal and, consequently achieve specific CO<sub>2</sub> intensities of 0.49-0.56 kg(CO<sub>2</sub>) kWh<sub>el</sub><sup>-1</sup> approximately half that of conventional coal-fired generation plants [152]. CO<sub>2</sub> neutrality can be achieved if biomass is used as feedstock. Ultimately, solar-driven gasification is a means of storing intermittent solar energy in a transportable and dispatchable chemical form.

Solar-driven pyrolysis and gasification was investigated in earlier studies [14, 46, 47, 78, 103]. More recently, solar thermal gasification was successfully applied to various carbonaceous materials (among which coal, petroleum coke, vacuum residue, and charcoal) using directly irradiated fluidized-bed [67, 151], molten-salt pool [6], and vortex-flow reactors [163], as well as indirectly-irradiated packed-bed [110], and particle-flow [91] reactors with graphite/ceramic tubes or other opaque surfaces serving as absorbers and heat conductors. Of special interest is the latter reactor concept, schematically shown in Fig. 5.1. It consists of a cylindrical solar cavity-receiver with a windowless slab (rectangular) aperture containing an array of tubular absorbers, through which a reacting mixture of steam and carbonaceous particles flow. A trough compound parabolic concentrator (CPC) [155] is incorporated at the aperture to further augment the incident solar flux, reduce the aperture size, and minimize re-radiation losses. Concentrated solar energy entering through the aperture is transferred by combined radiation/conduction/convection to the reacting flow. In the following sections, the numerical reactor model developed in Chap. 4 is modified accordingly. Its experimental validation is accomplished with a 3 kW reactor prototype tested for the steam-gasification of biochar. The reactor model is then applied to optimize the design and simulate the performance of a 10 MW reactor for a solar tower system.

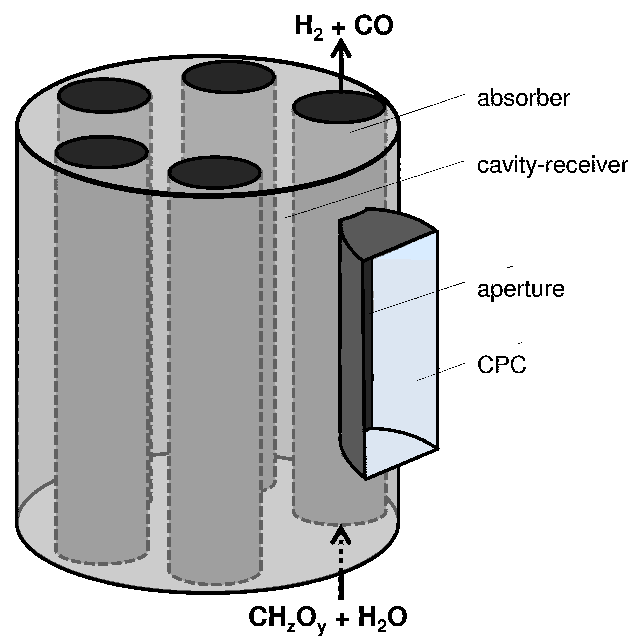


Figure 5.1: Solar reactor configuration consisting of a cavity-receiver with a windowless slab aperture containing an array of tubular absorbers, through which a reacting mixture of steam and carbonaceous particles flow. A 2D-CPC is incorporated at the aperture.

## 5.2 Problem statement

The solar reactor prototype for 3 kW solar power input has been previously described [91]. The radiative exchange between the cavity and absorber tube has been modeled in a previous study [87]. Thus, the outer absorber tube surface is taken as domain boundary. The model domain is shown schematically in Fig. 5.2. It consists of a reaction-bonded silicon-infiltrated silicon carbide absorber tube (SiSiC, HALSIC-I: 88-92 vol% SiC, 12-8 vol% metallic Si [153]) of outer diameter  $d_{\text{absorber,o}} = 2.5$  cm, inner diameter  $d_{\text{absorber,i}} = 1.8$  cm, and length  $L_{\text{absorber}} = 0.15$  m. Water vapor ( $\dot{m}_{\text{H}_2\text{O,in}} = 0.79$  g min<sup>-1</sup>), and Ar ( $\dot{V}_{\text{Ar,in}} = 4.5$  l<sub>N</sub> min<sup>-1</sup>), resulting in an inlet gas H<sub>2</sub>O molar fraction  $\bar{x}_{\text{H}_2\text{O,in}} = 0.18$ , are injected into the tube at  $T_{\text{in}} = 473$  K and  $p_{\text{in}} = 101,325$  Pa. Beech charcoal particles (Fluka 03866,  $\rho_{\text{biochar}} = 450$  kg m<sup>-3</sup> [22], mean particle size = 7.2 μm, elemental composition is CH<sub>0.418</sub>O<sub>0.117</sub>S<sub>0.003</sub>N<sub>0.006</sub>, ash content 5 %), of BET specific surface area 180 m<sup>2</sup> g<sup>-1</sup>, as determined by N<sub>2</sub> adsorption at 77 K (Micromeritics TriStar 3000), are used as the carbonaceous feedstock. The particle size distribution functions, as measured by laser scattering (HORIBA LA-950), are shown in Fig. 5.3. Plotted are the number ( $f_d$ ) and volume ( $v_d$ ) distribution probability densities of the beech charcoal feedstock. Elemental composition was determined with Leco CHN-900 (C-, H-, N-detection), Leco RO-478 (O-detection, and Leco CHNS-932 (S-detection) instruments.

Biochar particles are fed into the gas stream using a rotating brush feeder at a rate of 0.35 g min<sup>-1</sup>, resulting in a particle volume fraction  $f_V = 8.2 \cdot 10^{-5}$  at inlet. Heat is transferred by conduction through the tube wall and by combined radiation, convection, and conduction into the axially-flowing, reacting medium. For conduction,

$$q_{\text{conduction}}(z) = \frac{2\pi k_{\text{SiC}} (T_{\text{absorber,o}} - T_{\text{absorber,i}}(z))}{\ln(d_{\text{absorber,o}}/d_{\text{absorber,i}})}. \quad (5.2)$$

A value of  $k_{\text{SiC}} = 45.2$  W m<sup>-1</sup> K<sup>-1</sup> at 1,073 K is given by the manufacturer [153], which results in a difference between inner and outer surface temperature lower than 10 K. Over the reaction zone, a constant outer absorber temperature  $T_{\text{absorber,o}}$  is assumed. Convective heat transfer in the inner tube is given by [58]:



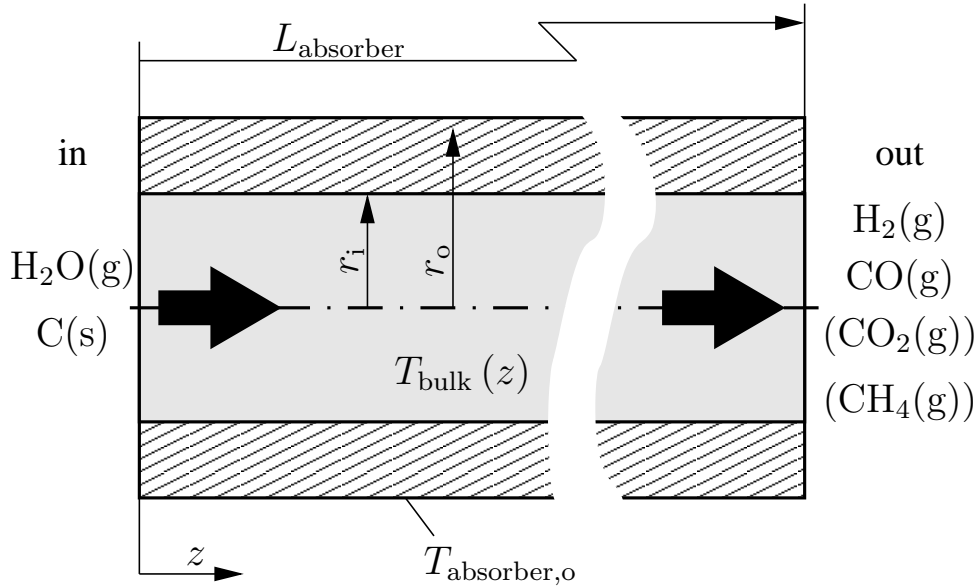


Figure 5.2: Longitudinal section view of an absorber tube.

- for laminar flow:

$$\text{Nu}(z) = 3.66, \quad (5.3)$$

- and for turbulent flow:

$$\text{Nu}(z) = 0.023\text{Re}(z)^{0.8} \text{Pr}(z)^{0.4}. \quad (5.4)$$

with  $\text{Re}(z) = \rho(z)w(z)d_{\text{absorber},i}/\mu(z)$ ,  $\text{Pr}(z) = \bar{c}_p(z)\mu(z)/k(z)$ , and  $\text{Nu}(z) = \alpha(z)d_{\text{absorber},i}(z)/k(z)$ . For transitional flow ( $2,300 \leq \text{Re} \leq 10,000$ ),  $\text{Nu}$  is obtained by linear interpolation between the two cases. The heat conductivity  $k$  and the dynamic viscosity  $\mu$  of the gas mixture (Ar, H<sub>2</sub>O, H<sub>2</sub>, CO) are calculated from the kinetic gas theory [133], whereas polynomial approximations are used for specific heat  $\bar{c}_p$  [18] (see Appx. C). The first two properties are computed for the gas phase by a weighted sum for all species using their molar concentration as weight function. Radiative heat exchange between the tube walls and the carbon particles in the reacting flow is treated by a collision-based Monte Carlo model [162] (see Sec. 4.3.2). Application of the line-by-line model to the molecular spectroscopic database HITRAN-2004 [122] for similar  $f_V$  of particles indicated that the contribution of the gas phase is less than 5 % of the total radiative flux, and therefore negligible [86]. The absorption, scattering, and extinction coefficients and the scattering phase function are obtained by applying

$Q_{\text{nominal}}$ kW	$d_{\text{absorber},i}$ m	$a$ $\text{W m}^{-2} \text{K}^{-4}$	$b$ $\text{W m}^{-2} \text{K}^{-4}$	$c$ $\text{W m}^{-2} \text{K}^{-4}$
3	0.018	-3.56	$1.88 \cdot 10^{-4}$	0
10,000	0.08	-3.37	$7.02 \cdot 10^{-4}$	0

Table 5.1: Coefficients  $a$ ,  $b$ , and  $c$  determined by least-square fitting of a second-order polynomial function to radiative heat transfer rates obtained by MC for the 3 kW and the 10 MW reactor design.

the Mie theory [19] for 11 size intervals of the particle size distribution of Fig. 5.3, based on the particle size parameter  $\xi = \pi d_{\text{particle}}/\lambda$  in the range  $10^{-1} - 10^2$  and the complex refractive index of the particle approximated by that of propane soot [20, 32]. For a given particle size distribution, simulation results for the radiative heat flux between the inner tube wall and the medium could be reasonably well approximated in the range of interest by:

$$q_{\text{radiation}} = (af_V^2 + bf_V + c) (T_{\text{wall}}^4 - T_{\text{bulk}}^4), \quad (5.5)$$

, where the parameters  $(a, b, c)$  are obtained by least-square fitting to the data points generated by MC. The parameters are listed in Tab. 5.1 for the 3 kW and the 10 MW reactor design.

The steady-state 1D mass conservation equation is formulated for each component  $i$ :

$$\frac{\partial \bar{\rho}_i}{\partial t} = 0 = -\frac{\partial}{\partial z} (\bar{\rho}_i w) + \bar{r}_i. \quad (5.6)$$

with  $w$  being the flow velocity in the axial direction. No velocity difference between the particles and the gas mixture is assumed. The boundary condition at inlet is  $\bar{\rho}_{1,i}(z=0) = \bar{x}_{\text{in},i} p_{\text{in}} / \bar{R} T_{\text{in}}$  for each inlet gaseous component  $i = (\text{H}_2\text{O}, \text{Ar})$ , and  $\bar{\rho}_j(z=0) = \bar{x}_j f_{V,\text{in}} \rho_{\text{biochar}} / [\bar{M}_{\text{biochar}} (1 + f_{V,\text{in}})]$  for each solid component of biochar  $j = (\text{C}, \text{H}, \text{O})$ : N and S are neglected, with .

The reaction kinetics were determined by thermogravimetry [109]. Application of the shrinking spherical particle model for an unreacted spherical core [80] yields an expression for the reaction rate of each component  $i$

$$\bar{r}_i = \frac{d\bar{\rho}_i(z)}{dt} = \nu_i \bar{\rho}_{\text{C},\text{in}}^{1/3} k(z) \bar{\rho}_{\text{C}}^{2/3}(z). \quad (5.7)$$

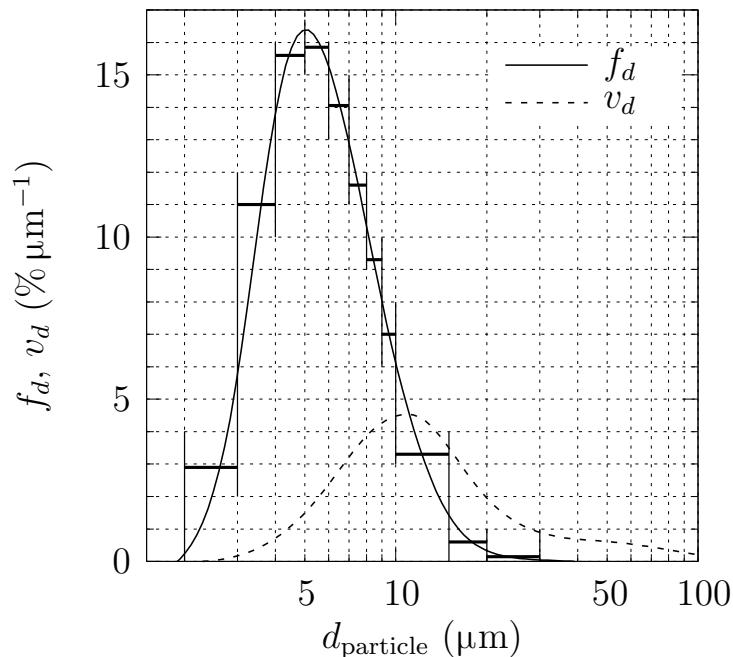


Figure 5.3: Particle number ( $f_d$ ) and volume ( $v_d$ ) distribution probability densities of the beech charcoal feedstock and the 11 discrete size intervals used for computation of the radiative properties of the particle suspension.

$\nu_i$  is the stoichiometric coefficient of each species of Eq. (5.1). The rate constant is assumed to obey the Arrhenius law,  $k(z) = k_0 \exp(-E_a/\bar{R}T_{\text{bulk}}(z))$ , with an apparent activation energy  $E_a = 43,154 \text{ J mol}^{-1}$  and a pre-exponential factor  $k_0 = 120.6 \text{ s}^{-1}$ , the latter being adjusted for the experimental validation of the reactor model, and in good agreement with the one obtained by applying a 2D steady-state reactor model with uniform reaction zone temperature ( $k_0 = 124.6 \text{ s}^{-1}$ )[91].

Assuming plug flow and ideal gas while neglecting the volume of the solid phase ( $f_V < 10^{-4}$ ) and the pressure drop (below 1 % across the entire system),  $\dot{V}_g(z) = \dot{n}_g(z) \bar{R}T_{\text{bulk}}(z)/p_{\text{in}}$ . Deriving with respect to axial distance  $z$  yields the infinitesimal flow velocity change:

$$\frac{dw}{dz} = \frac{\bar{R}T_{\text{bulk}}(z)}{p} \sum_i \dot{r}_i'''(z) + \frac{w(z)}{T_{\text{bulk}}(z)} \frac{dT_{\text{bulk}}(z)}{dz}. \quad (5.8)$$

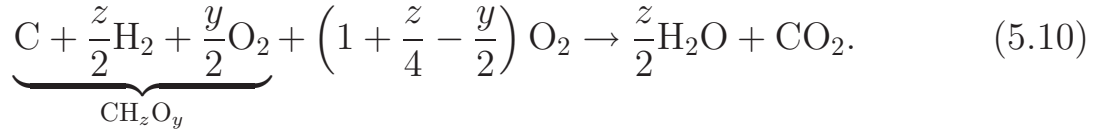
The first right-hand term accounts for gas moles being produced by the chemical reaction while the second term considers thermal gas expansion.

Boundary condition at inlet is  $w(z=0) = w_{\text{in}} = \dot{V}_{\text{g,in}}/A_{\text{absorber,i}}$ .  $A_{\text{absorber,i}}$  is the inner cross-section area of the tube.

The steady-state 1D energy conservation equation is formulated assuming infinitely fast thermal exchange between the particle suspension and the gas:

$$\begin{aligned} \frac{\partial}{\partial t} \left( \sum (\bar{\rho}_i(z) \bar{h}_i(z)) \right) &= \frac{\partial}{\partial z} (\bar{\rho}_i(z) w(z) \bar{h}_i(z)) + \\ &+ \frac{\partial q_{\text{conduction}}(z)}{\partial z} - \bar{r}_{\text{C}}(z) \Delta \bar{h}_{\text{R}}(z), \end{aligned} \quad (5.9)$$

with the initial condition  $T(z=0) = T_{\text{in}} = 473 \text{ K}$ , where  $\Delta \bar{h}_{\text{R}}(z) = \sum_i \nu_i \bar{h}_i(T_{\text{bulk}}(z))$  is the enthalpy change over the reaction per reacted number of C moles. Since charcoal has no reference enthalpy, all enthalpy changes were calculated by assigning to charcoal the reference enthalpy of its elemental composition at 300 K, and further adjusting for the small offset between the heating value of charcoal ( $473.9 \text{ kJ mol(C)}^{-1}$ , calculated from elemental composition [105]) and the enthalpy change of the combustion reaction at 300 K given by



Eqs. (5.6), (5.8), and (5.9) are discretized in space and solved using the finite volume method [42].

### 5.3 Experimental validation

The reactor model is validated by comparing its results to those obtained experimentally using a 3 kW solar reactor prototype tested at ETHs high-flux solar simulator [56]. The extent of chemical reaction is obtained through a C-balance:

$$X_{\text{C}} = \frac{\dot{n}_{\text{CO,out}} + \dot{n}_{\text{CO}_2,\text{out}} + \dot{n}_{\text{CH}_4,\text{out}}}{\dot{n}_{\text{C,in}}}. \quad (5.11)$$

Inlet biochar mass flow was determined by experimental calibration of the brush feeder. Outlet gas flows were measured on-line by gas chromatography. For the temperature measurement on the outer absorber tube wall a

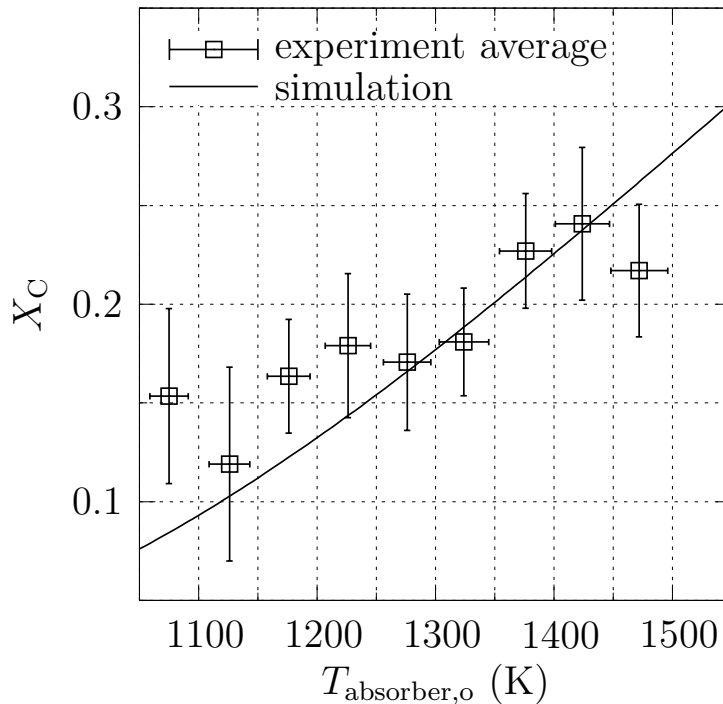


Figure 5.4: Averaged experimentally measured (18 runs at 9 different  $T_{\text{absorber,o}}$  and theoretically calculated reaction extent in function of  $T_{\text{absorber,o}}$  for the 3 kW reactor prototype.

shielded thermocouple was employed. Error bars result from inaccuracies in the measurement and feeding devices (temperature  $\pm 2\%$  of reading, gas flow controllers  $\pm 0.8\%$  of reading plus  $\pm 0.2\%$  of scale, water flow controller  $\pm 1\%$  of reading, outlet gas concentrations  $\pm 0.005$  vol%, biochar feeding rate  $\pm 0.05 \text{ g min}^{-1}$ ) [91]. Figure 5.4 shows the numerically calculated (curve) and averaged experimentally measured (data points) reaction extent as function of  $T_{\text{absorber,o}}$ . The agreement between calculated and the averages of 18 experimentally obtained values lies within  $18.8\% \pm 23.7\%$  (mean difference  $\pm$  standard deviation). The very efficient heat transfer from the inner wall to the reacting flow is mainly due to the radiation absorbed by the particles (30 – 50 % of total tube-to-bulk heat transfer rate), leading to a fast (0.030 s,  $\tau \approx 0.077$  s, for  $T_{\text{absorber,o}} = 1600$  K) convergence of the medium temperature  $T_{\text{bulk}}(z)$  within 95 % of  $T_{\text{absorber,i}}(z)$ .

## 5.4 Scale-up to 10 MW solar power input

The industrial-scale solar reactor presented in Sec. 4.5, mounted on a solar tower system is considered. A description of the optimized cavity-receiver shape is given in Appendix E. Band-approximated spectral optical properties for the quartz window and SiC absorber tubes and walls are given in Appendix B. For SiC, a constant value of  $E = 0.9$  is chosen as the properties do not vary significantly over the considered wavelength range [146].  $Q_{\text{solar}}$  is assumed to have Planck's spectral distribution of a blackbody source at  $T_{\text{source}} = 5,780$  K. Net absorbed process heat is modeled as a heat sink on the absorber surface. Further assumptions are: diffuse window, opaque-diffuse cavity walls, uniform radiative heat flux, temperature, and properties on both surfaces, as well as no conductive or convective heat transfer between window, cavity, and absorbers. Equation (4.2) applying the radiosity method (enclosure theory) for semi-transparent enclosures [132] is modified to account for the different number of surfaces, yielding a spectral-dependent system of equations in terms of the steady-state temperatures and net radiative fluxes on each surface:

$$\begin{aligned} & \sum_{j=1}^{N_{\text{absorbers}}+8} \frac{1}{E_{\lambda j,i}} (\delta_{kj} - R_{\lambda j,i} F_{k-j}) \\ & \left[ \frac{dq_{\lambda j}}{d\lambda} - E_{\lambda j,o} e_{\lambda b}(T_j) + (1 - R_{\lambda j,o}) \frac{dq_{\lambda e,j}}{d\lambda} \right] = \\ & = \sum_{j=1}^{N_{\text{absorbers}}+8} \left( e_{\lambda b}(T_j) + \frac{V_{\lambda j,o}}{E_{\lambda j,i}} \frac{dq_{\lambda j}}{d\lambda} \right) [\delta_{kj} - (1 - V_{\lambda j,i}) F_{k-j}] \end{aligned} \quad (5.12)$$

for  $1 \leq k \leq (N_{\text{absorbers}} + 8)$ , ( $1-7 =$  windows,  $8 =$  cavity,  $9-(N_{\text{absorbers}} + 8) =$  absorber tubes, see Fig. 4.6, where  $q_{e,j} = Q_{\text{solar}}/A_{\text{window}}$  (for  $1 \leq j \leq 7$ ),  $q_{e,j} = 0$  (for  $8 \leq j \leq (N_{\text{absorbers}} + 8)$ ), and  $q_j = -Q_{\text{absorber},j}/A_{\text{absorber},j}$ , for  $9 \leq j \leq (N_{\text{absorbers}} + 8)$ ). Subscripts i and o denote inner and outer properties of the boundary walls, respectively. Neglecting external emission at the walls and absorber tubes,  $\{E_{j,o}; R_{j,o}; V_{j,o}\} = \{E_{j,i}; R_{j,i}; V_{j,i}\}$ , for  $1 \leq j \leq 7$ , and  $E_{j,o} = R_{j,o} = V_{j,o} = V_{j,i}$  for  $8 \leq j \leq (N_{\text{absorbers}} + 8)$ . The view factor matrix between the faces is obtained by Monte Carlo ray-tracing code. The system of equa-

tions (5.12) is integrated over the windows three spectral bands  $l$  to yield a system of  $(N_{\text{absorbers}} + 8) \times 3$  spectrally-independent equations for totally  $(N_{\text{absorbers}} + 8) \times (3 + 1)$  unknowns  $(q_{jl}, T_j)$ . The remaining equations are obtained from the relationship  $q_j = \sum_{l=1}^3 q_{jl}$ , for  $1 \leq j \leq (N_{\text{absorbers}} + 8)$ . The incoming radiation heat flux per spectral band  $l$  for each face is  $q_{e,jl} = \frac{q_{e,j}}{\sigma T_{\text{sun}}^4} \int_{\lambda_{l,1}}^{\lambda_{l,2}} e_{\lambda b}(\lambda, T_{\text{sun}}) d\lambda$ . Since the total (spectrally-integrated) optical properties of the windows are influenced by their temperatures  $T_j$ , their value has to be determined iteratively.

This cavity-receiver model is coupled to the absorber tube model presented in Sec. 5.2. The cavity-receiver model considers the incoming solar power  $Q_{\text{solar}}$  and the net heat sink  $Q_{\text{absorber},j}$  on each absorber tube, and computes the outer surface temperatures  $T_{\text{absorber},j}$  of each absorber tube. These serve as input for the tube model which, given the inlet conditions  $(T_{\text{in}}, p_{\text{in}})$ , the composition  $(\bar{x}_{\text{in},i})$  of the gas mixture, and the inlet particle volume fraction  $(f_{V,\text{in}})$ , is used to compute the net absorbed process heat by the fluid in each tube,  $Q_{\text{absorber},j}^*$ . The matching combinations of  $Q_{\text{absorber},j}$  and  $T_{\text{absorber},j}$  are obtained by iteration with convergence criterion  $|1 - Q_{\text{absorber},j}(T_{\text{absorber},j}, T_{\text{in}}, p_{\text{in}}, \bar{x}_{\text{in},i}) / Q_{\text{absorber},j}^*| \leq 0.001$ , for each surface  $j$ . Two energetic performance indicators of the system are applied. The thermal energy conversion efficiency is defined as:

$$\eta_{\text{thermal}} = \frac{Q_{\text{thermal}} + Q_{\text{chemical}}}{Q_{\text{solar}}}, \quad (5.13)$$

The chemical energy conversion efficiency is defined as:

$$\eta_{\text{chemical}} = \frac{Q_{\text{chemical}}}{Q_{\text{solar}}}, \quad (5.14)$$

with  $Q_{\text{thermal}} = \sum_i \int_{T_{\text{in}}}^{T_{\text{out}}} \dot{n}_{\text{in},i} \bar{c}_{p,i}(T) dT$  being the power supplied for heating up the injected gases  $i$  and  $Q_{\text{chemical}} = \int_0^{L_{\text{absorber}}} \bar{r}_C(z) \Delta \bar{h}_R(T_{\text{bulk}}) A_{\text{absorber},i} dz$  the enthalpy difference between reactants and products at reaction temperature. The performance

of the three cavity-receivers is simulated over the relevant range of operational conditions, assuming pure H<sub>2</sub>O inlet flow, laden with particles at a H<sub>2</sub>O:C ratio of 2.0, pre-heated to 473 K. Figure 5.5 shows the outlet gas temperature  $T_{\text{out}}$  as a function of inlet H<sub>2</sub>O mass flow rate  $\dot{m}_{\text{H}_2\text{O},\text{in}}$  and the incoming solar radiative flux through the apertures  $q_{\text{solar}}$  for the North (a) and the East/West (b) cavity-receivers. Since  $T_{\text{out}} > 1,400$  K is required for minimizing the CO<sub>2</sub>:CO ration in the outlet gas [99],  $T_{\text{out}} = 1,500$  K is set for the present analysis. For  $q_{\text{solar}} = 3.5 \text{ MW m}^{-2}$ , such an outlet temperature is obtained with  $\dot{m}_{\text{H}_2\text{O},\text{in}} = 2.21 \text{ kg s}^{-1}$ , while for lower  $q_{\text{solar}} = 1.5 \text{ MW m}^{-2}$ , only  $0.61 \text{ kg s}^{-1}$  can be processed. Figure 5.6 shows the extent of chemical reaction  $X_{\text{C}}$  as a function of  $\dot{m}_{\text{H}_2\text{O},\text{in}}$  and  $q_{\text{solar}}$  for the North (a) and the East/West (b) cavity-receivers.  $X_{\text{C}}$  drops rapidly with increasing  $\dot{m}_{\text{H}_2\text{O},\text{in}}$ , due to insufficient residence times. For example,  $X_{\text{C}} = 31 \%$  for  $q_{\text{solar}} = 3.5 \text{ MW m}^{-2}$  at higher mass flow rate, but  $X_{\text{C}} = 67 \%$  for  $q_{\text{solar}} = 1.5 \text{ MW m}^{-2}$  at lower mass flow rate. Also, the bigger quantity of processed mass barely compensates for the higher solar concentrations necessary for heating it up and reaching the desired  $T_{\text{out}}$ . This is corroborated in Fig. 5.7, which shows the thermal energy conversion efficiency  $\eta_{\text{thermal}}$  as a function of  $\dot{m}_{\text{H}_2\text{O},\text{in}}$  and  $q_{\text{solar}}$  for the North (a) and the East/West (b) cavity-receivers. An optimum  $q_{\text{solar}} = 1.5 \text{ MW m}^{-2}$  results in maximum  $\eta_{\text{chemical}}$  (32 %), as shown in Fig. 5.8, while for  $q_{\text{solar}} = 3.5 \text{ MW m}^{-2}$  a relatively low  $\eta_{\text{chemical}}$  of 18 % is reached. Since  $X_{\text{C}}$  decreases with increasing  $\dot{m}_{\text{H}_2\text{O},\text{in}}$  the maximal attainable values for  $\eta_{\text{chemical}}$  decrease with higher  $q_{\text{solar}}$ . Assuming  $X_{\text{C}} = 1$  yields a value of 41 % for  $q_{\text{solar}} = 3.5 \text{ MW m}^{-2}$ , thus pointing out the significant solar-to-chemical efficiency gain potential through cavity shape and absorber tube size optimization at highly concentrated solar inlet flux.

## 5.5 Summary

In this chapter, the heat transfer model presented in Chap. 4 was modified to simulate a solar chemical reactor for steam gasification of carbonaceous particles. The model couples radiative heat transfer within the cavity-receiver with radiation / convection / conduction heat transfer for a reacting flow inside the absorber tubes. Experimental validation of the absorber



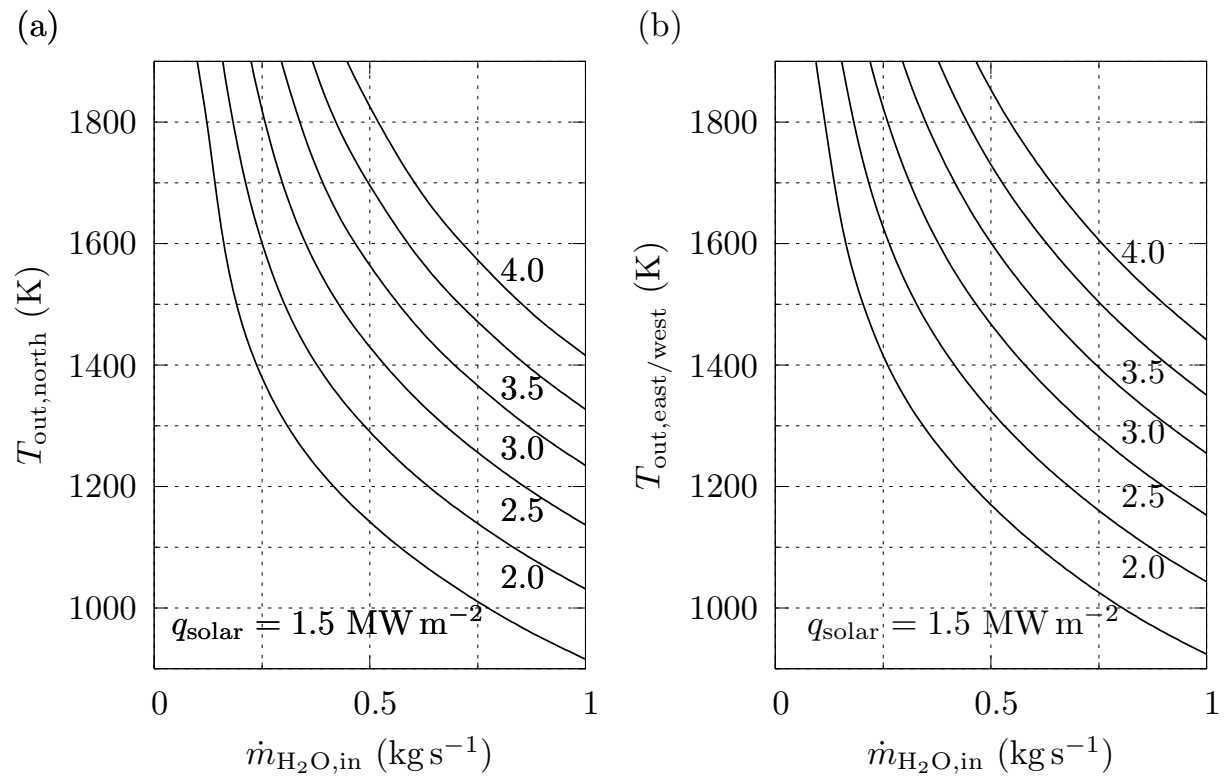


Figure 5.5: Variation of the outlet gas temperatures  $T_{\text{out}}$  with inlet  $\text{H}_2\text{O}$  mass flow rate  $\dot{m}_{\text{H}_2\text{O},\text{in}}$  for the North (a) and East/West (b) scale-up cavity-receivers. The parameter is the solar radiative flux through the reactor aperture  $q_{\text{solar}} = 1.5, 2.0, 2.5, 3.0, 3.5,$  and  $4.0 \text{ MW m}^{-2}$  and the inlet  $\text{H}_2\text{O}:\text{C}$  ratio is 2.0.

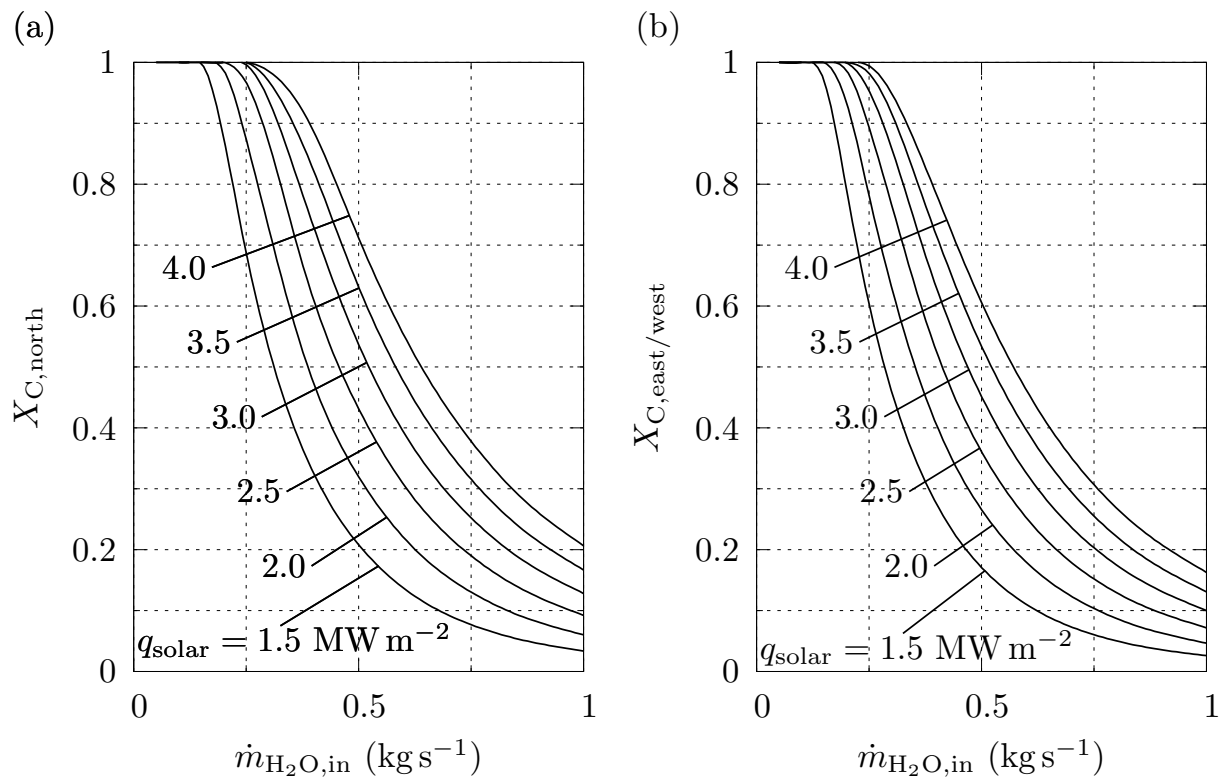


Figure 5.6: Variation of the extent of chemical reaction  $X_C$  with inlet  $H_2O$  mass flow rate  $\dot{m}_{H_2O,in}$  for the North (a) and East/West (b) scale-up cavity-receivers. The parameter is the solar radiative flux through the reactor aperture  $q_{solar} = 1.5, 2.0, 2.5, 3.0, 3.5,$  and  $4.0\ MW\ m^{-2}$  and the inlet  $H_2O:C$  ratio is 2.0.

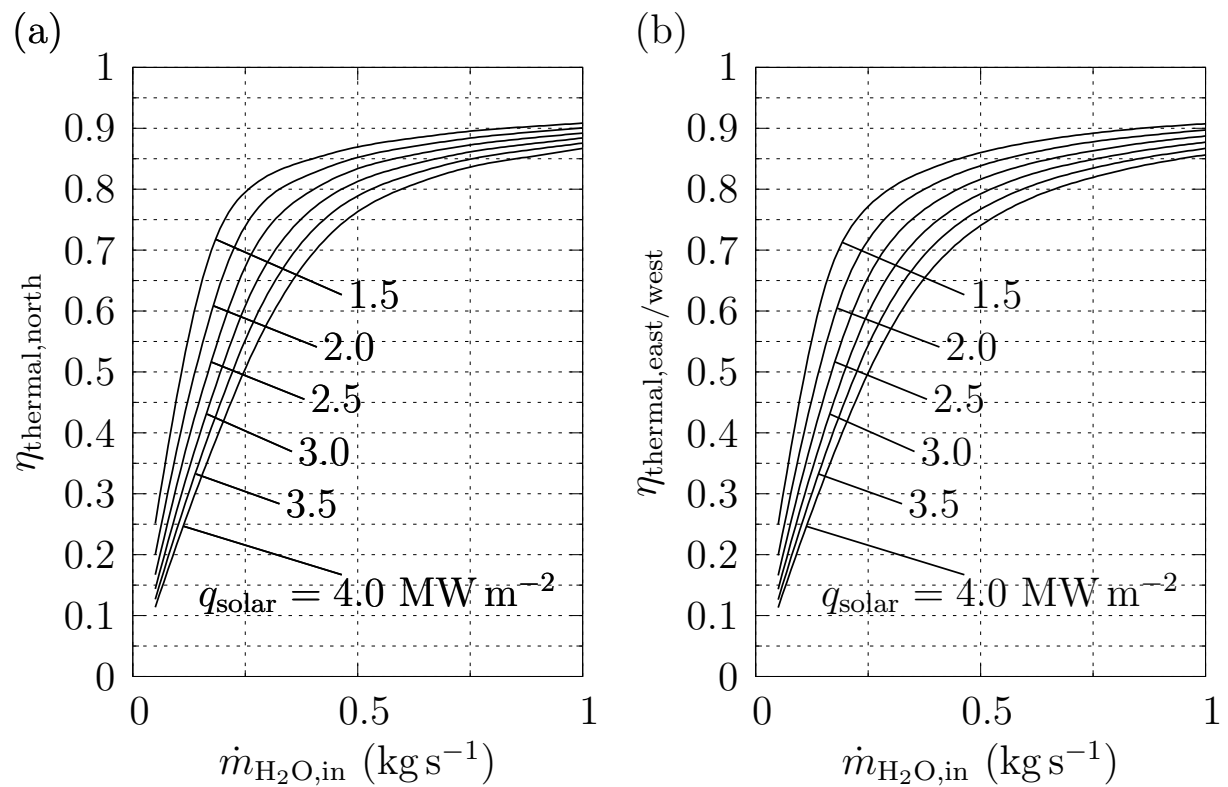


Figure 5.7: Variation of the thermal energy conversion efficiency  $\eta_{\text{thermal}}$  with inlet  $\text{H}_2\text{O}$  mass flow rate  $\dot{m}_{\text{H}_2\text{O},\text{in}}$  for the North (a) and East/West (b) scale-up cavity-receivers. The parameter is the solar radiative flux through the reactor aperture  $q_{\text{solar}} = 1.5, 2.0, 2.5, 3.0, 3.5,$  and  $4.0 \text{ MW m}^{-2}$  and the inlet  $\text{H}_2\text{O}:\text{C}$  ratio is 2.0.

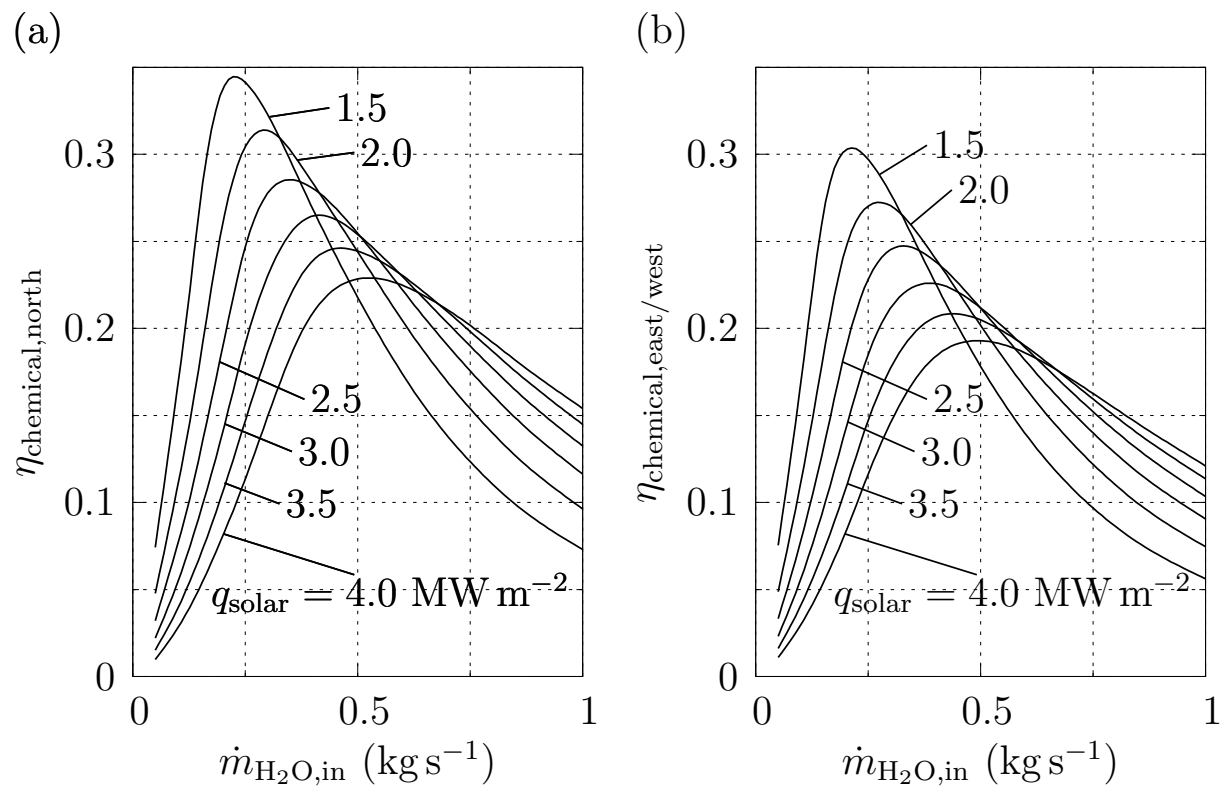


Figure 5.8: Variation of the chemical energy conversion efficiency  $\eta_{\text{chemical}}$  with inlet  $\text{H}_2\text{O}$  mass flow rate  $\dot{m}_{\text{H}_2\text{O},\text{in}}$  for the North (a) and East/West (b) scale-up cavity-receivers. The parameter is the solar radiative flux through the reactor aperture  $q_{\text{solar}} = 1.5, 2.0, 2.5, 3.0, 3.5,$  and  $4.0 \text{ MW m}^{-2}$  and the inlet  $\text{H}_2\text{O}:\text{C}$  ratio is 2.0.

---

tube model was carried out with a 3 kW solar reactor prototype. The agreement between the calculated curve for  $X_C$  in function of  $T_{\text{absorber,o}}$  and the 19 experimentally obtained values lies within  $18.8\% \pm 23.6\%$  (mean difference  $\pm$  standard deviation). The validated model was applied to estimate the performance of a 10 MW scale-up reactor for a solar tower system. For a desired outlet temperature of 1,500 K, low radiative inlet concentrations (1,500 suns) show a higher solar-to-chemical energy conversion efficiency (32 %) than higher ones (18 % at 3,500 suns) due to the higher mass flow and consequently lower residence times and extents of chemical reaction of the latter case. An estimation of the improvement potential for the solar-to-chemical energy conversion efficiency shows values up to 41 % at 3,500 suns to be obtainable by optimization of the cavity and absorber tube sizes for full reaction of the fed biochar.



# Chapter 6

## Conclusion

This thesis was performed in the framework of the EU-project SOLHY-CARB. Final goal of the project was the development and testing of solar reactor prototypes of size up to 50 kW, the development and validation of a numerical model to predict the performance of a commercial-scale (10 MW<sub>th</sub>) scale-up reactor in order to assess the economical feasibility of the process. ETH and PSI's work package included the following tasks:

1. experimental testing of a laboratory-scale solar thermal reactor prototype for thermal cracking of CH<sub>4</sub>,
2. development and validation of a numerical model to simulate radiative heat transfer within a reacting cloud of carbonaceous particles suspended in a CH<sub>4</sub> flow,
3. development and validation of a numerical model to simulate a solar thermal reactor according to the design chosen for the scale-up: an indirectly-irradiated type of reactor consisting of a receiver-cavity containing an array of absorber tubes through which the reacting medium flows,
4. application of the model to design a 10 MW<sub>th</sub> commercial-scale reactor and predict its performance.

The work carried out for these tasks constitutes the backbone of this thesis and accounts for Chapters 2 (task 2), 3 (task 1), and 4 (tasks 3 and 4). Additional elements of the thesis are the application of the 10 MW<sub>th</sub> scale-up model to the process of steam-gasification of carbonaceous material in

order to prove the validity and versatility of the chosen modeling approach. As a byproduct of the formulated model for radiative heat exchange within a solar cavity-receiver, a study comparing the thermal behavior of cavities featuring windows made from quartz and sapphire was performed (Appx. A).

## 6.1 Experimental work

An improved design of a 5 kW solar chemical reactor for co-producing  $H_2$  and C by thermal cracking of  $CH_4$  was experimentally investigated in a solar simulator and a solar furnace. A total of 49 valid experiments was performed. Modifications applied to the original reactor design (conical product outlet and additional insulation layer) showed to avoid deposition of particles inside the cavity and allowed to increase the operation temperature. Calculated inner reactor wall temperatures range between 1,130 and 1,610 K. The seeding of carbon black particles to a continuous flow of  $CH_4$  proved to enhance the radiative heat transfer and the reaction kinetics. Maximum methane conversion of 98.8 % and hydrogen yield of 99.1 % were reached. The peak solar-to-chemical energy conversion efficiency was 16.1 %, with an average value of 9.1 %. The parametric study showed an increase of the chemical conversion with particle volume fraction and incoming solar radiative flux as a result of the enhanced radiative absorption by the participating medium. The influence of the injected gas volume flow rate was weak in the considered parametric range, while an increase of  $CH_4$  molar concentration proved to be counterproductive for the reaction extent due to the higher specific heat of  $CH_4$ . In contrast, the solar-to-chemical energy conversion efficiency was positively influenced by an increase in the gas volume flow rate and  $CH_4$  concentration because of the increased rate of heated material in the first case and the higher specific heat of  $CH_4$  in the second. The SEM images showed deposition of filamentous agglomerates of spherical particles sized 50-500 nm, which covered the porous structure of the seed particles, reducing their BET active surface. Model simulations indicated the possibility of reaching significantly higher energy conversion efficiencies (by a factor 2-4) for the same operational parameters when employing pure  $CH_4$ .



## 6.2 Modeling

The modeling work was substantially divided into two distinct parts: at first, the simulation of heat and mass transfer within a two phase medium; secondly a complete reactor model.

The heat and mass transfer model was developed to compute temperature and chemical composition of a reacting two-phase solid-gas flow initially composed of  $\text{CH}_4$  laden with carbon particles, and directly exposed to concentrated solar radiation. Optical properties of the particles were computed from literature data using Mie theory, while those of  $\text{CH}_4$  were obtained from the HITRAN database and approximated using a band model. For the simulation of radiation heat transfer into and within the medium, the path length Monte Carlo method with ray redirection was applied. Maximum (steady-state) temperatures in the range of 1,700 – 1,800 K were obtained for initial carbon particles of 1 – 10  $\mu\text{m}$  diameter and initial volume fraction in the range  $5 \cdot 10^{-6}$  –  $5 \cdot 10^{-5}$ . The maximum  $\text{CH}_4$  conversion in steady-state was 46.5 % for the inlet and initial volume fraction and particle diameter of  $f_{V,0} = 5 \cdot 10^{-5}$  and  $d_0 = 2.5 \mu\text{m}$ , corresponding to maximum particle temperatures of 1,780 K. Validation was accomplished by comparing the computed steady-state temperatures and reaction extents with those obtained experimentally using a particle-flow solar reactor prototype subjected to concentrated solar radiation.

To simulate a complete solar chemical reactor, a second model, coupling radiative heat transfer within the cavity-receiver with radiation/convection/conduction heat transfer for a reacting flow inside the absorber tubes, was built. Radiative heat transfer inside the absorber tubes was approximated using a simplified correlation based on simulated data points using the first model. Experimental validation was carried out with a 10 kW solar reactor prototype. For 65 solar experimental runs, the standard deviation of relative errors between measured and simulated outer absorber tube temperatures was 1.7 % and the one between measured and simulated  $\text{H}_2$  concentrations at the outlet was 29.1 %. The validated model was applied to optimize the design and estimate the performance of a 10 MW scale-up reactor for a solar tower system. At design point, a maximum methane mass flow of approximately  $0.75 \text{ kg s}^{-1}$  can be completely reacted

for a desired outlet temperature of 1,870 K, yielding a solar-to-chemical energy conversion efficiency of 42 %. If lowered to 1,600 K, the reacted mass flow rate doubles and the efficiency rises to more than 60 %, but at the expense of an inferior carbon black quality.

The final scale-up model was additionally validated by applying it to the process of steam-gasification of biomass using experimental results obtained using a 3 kW particle-flow reactor prototype. The validated model was applied to estimate the performance of a 10 MW scale-up reactor for a solar tower system. For a desired outlet temperature of 1,500 K, low radiative inlet concentrations (1,500 suns) show a higher solar-to-chemical energy conversion efficiency (32 %) than higher ones (18 % at 3,500 suns) due to the higher mass flow and consequently lower residence times and extents of chemical reaction of the latter case. An estimation of the improvement potential for the solar-to-chemical energy conversion efficiency shows values up to 41 % at 3500 suns to be obtainable by optimization of the cavity and absorber tube sizes for full reaction of the fed biochar.

### 6.3 Outlook

Based on the performance predictions for the 10 MW<sub>th</sub> scale-up reactor presented in Chapter 4, the economic potential of the process will be assessed. It has been shown that the product quality increases with process temperature in the relevant operating range. This is valid for both the purity of the gaseous product (higher hydrogen yield) and the carbon particles, which reduces the need for gas separation equipment for the first and increases the expected market price for the second. On the other hand, the necessity of high process temperatures (up to 2,100 K) require a more complex concentrating system, able to deliver average concentrations up to 4,000 suns, with higher spillage losses. To find the optimum operating point, a trade-off between these two opposing effects has to be determined. The production of a model able to directly relate the operating temperature of the reactor to carbon black quality and thus price would have been a task beyond the scope of this thesis, but could greatly favor future assessments.

The detailed heat and mass transfer model presented in Chap. 2 resulted to be too computationally intensive to be used directly in the scale-

---

up model of Chap. 4. The search for a simplified model to be used led to the utilization of a polynomial equation for net heat transfer between absorber tube wall and the reacting medium. Parameters are the particle phase volume fraction and the temperature difference between the wall and the bulk of the reacting flow. Thus, this simplification can only be guaranteed to maintain its validity for the very same particle size, or size distribution, and temperature ranges for which the parameters of the polynomial approximation were determined. An application of the radiative heat transfer model to generate a larger number of data points in order to derive a more general relationship would represent a very useful evolution of the work presented in this thesis. For the radiative heat transfer model itself, very simple fluid flow conditions were assumed. The coupling of the very detailed radiative heat transfer model with a common 3D CFD full-featured solver would provide an useful, though probably very heavy, tool to increase the precision of the numerical predictions. Finally, the validation of the models could be enhanced by an increased accuracy of the input parameter  $\dot{m}_{C,in}$  which determines the particle phase volume fraction  $f_V$  and thus has, as shown in Chapter 2 a significant effect on radiative properties of the medium.



# Appendix A

## Temperature of a quartz/sapphire window in a solar cavity-receiver<sup>1</sup>

### A.1 Introduction

Solar receivers and reactors for highly concentrated solar applications usually feature the use of a cavity-type configuration, i.e. a well insulated enclosure designed to effectively capture incident solar radiation entering through a small opening - the aperture. Because of multiple internal reflections, the cavity's apparent absorptance<sup>2</sup> exceeds the inner surface absorptivity and, consequently, increases its ability to absorb incoming irradiation. The apparent absorptance has been calculated for cylindrical, conical, and spherical geometries having diffuse and specularly reflecting inner walls [82, 131, 137]. The larger the ratio of cavity area to aperture area, the closer the cavity-receiver approaches a blackbody absorber, but at the expense of higher conduction losses through the insulated cavity walls. Smaller apertures reduce re-radiation losses but intercept less sunlight. Consequently, the optimum aperture size becomes a compromise between maximizing radiation capture and minimizing radiation losses [141]. To some extent, the aperture size may be reduced with the help of non-imaging secondary concentrators, e.g. CPC, placed at the receiver's aperture in tandem with the primary concentrating system [155].

---

<sup>1</sup>Material from this chapter has been published in: G. Maag, C. Falter, and A. Steinfeld. Temperature of a quartz/sapphire window in a solar cavity-receiver. *J. Sol. Energy Eng.*, 133:014501, 2011.

<sup>2</sup>Fraction of energy flux emitted by a blackbody surface stretched across the cavity opening that is absorbed by the cavity walls [131]

Examples of relevant studies include a cavity containing an array of tubular absorbers [92] and two cavities in series [157, 165]. Some configurations of solar receivers and reactors are based on the direct irradiation of volumetric absorbers to provide efficient heat transfer directly to the absorbing materials (e.g. ceramic fins [61] and foams [23, 60]) and/or at the reaction site (e.g. packed-beds [126] and particle flows [164]). However, a major drawback when working with reducing or inert atmospheres is the requirement for a transparent window, which is a critical and troublesome component in high-pressure and severe environments, since it must be relatively thin for minimum radiation attenuation, yet strong and durable at high temperatures and pressures. Quartz windows ( $\text{SiO}_2$  m.p. 1,980 K) have an upper limiting operating temperature of about 1,000 °C while sapphire windows ( $\text{Al}_2\text{O}_3$  m.p. 2,290 K) allow for higher operating temperatures. Conical shapes [73], IR coatings [118], and active cooling [117] have been applied to improve window performance. In this appendix, the governing equations for radiative exchange within a generic windowed cavity-receiver are formulated for spectrally-selective quartz and sapphire windows. The calculated temperatures of window and cavity are plotted as a function of the incoming radiative flux and solar energy absorption efficiency.

## A.2 Analysis

The solar cavity-receiver is schematically depicted in Fig. A.1. The aperture is covered by a single-layer quartz/sapphire window, whose approximated optical properties are given in Appendix B for both materials. The window is exposed to concentrated solar thermal power  $Q_{\text{solar}}$ , assumed to have Planck's spectral distribution of a blackbody source at  $T_{\text{source}} = 5,780$  K. Net absorbed process heat is modeled as a heat sink on the cavity walls  $Q_{\text{cavity}}$ , whereas the net heat sink on the window  $Q_{\text{window}}$  represents convective losses. Further assumptions are: diffuse window, opaque-gray-diffuse cavity walls, uniform radiative heat flux, temperature, and properties on both surfaces, no conductive and convective heat transfer between window and cavity, and perfectly insulated cavity walls. The radiosity method (enclosure theory) for semi-transparent enclosures [130]

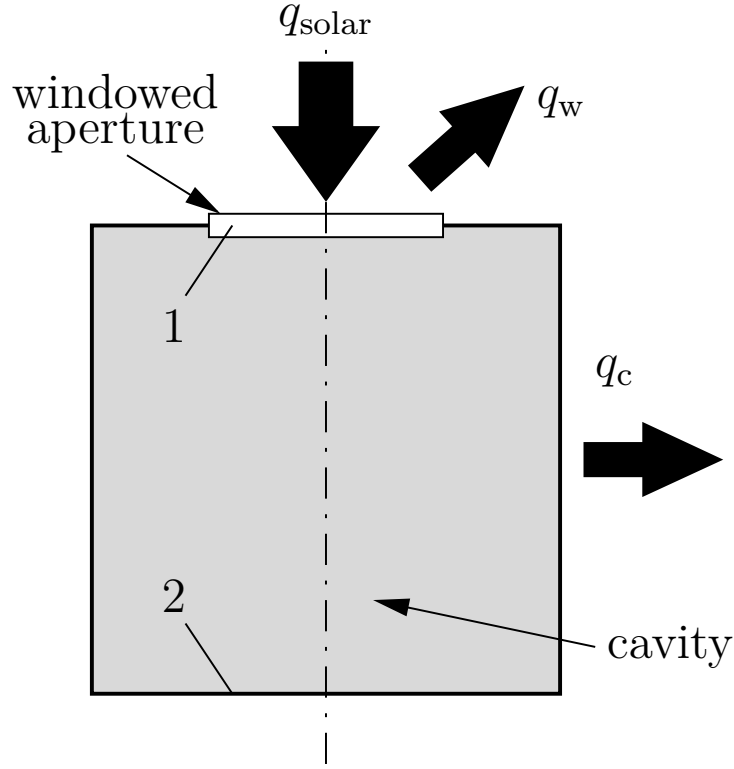


Figure A.1: Schematic of the solar cavity receiver configuration.

is applied to obtain a spectral-dependent system of equations for steady-state temperatures and net heat fluxes of the semi-transparent window and the opaque cavity (w=window, c=cavity):

$$-\frac{R_{\lambda,c}}{E_{\lambda,c}} \frac{dq_c}{d\lambda} + \frac{1}{E_{\lambda,w}} \frac{dq_w}{d\lambda} = -e_{\lambda b}(T_c) + 2e_{\lambda b}(T_w) - \frac{dq_{e,w}}{d\lambda}, \quad (\text{A.1})$$

$$\begin{aligned} & \frac{1}{E_{\lambda,c}} (1 - R_{\lambda,c} F_{c-c}) \frac{dq_c}{d\lambda} - \frac{R_{\lambda,w}}{E_{\lambda,w}} F_{c-w} \frac{dq_w}{d\lambda} = \\ & = (1 - F_{c-c}) e_{\lambda b}(T_c) - (1 + R_{\lambda,w} - V_{\lambda,w}) F_{c-w} e_{\lambda b}(T_w) + \\ & \quad \frac{R_{\lambda,w} (1 - R_{\lambda,w}) - V_{\lambda,w} (1 - V_{\lambda,w})}{E_{\lambda,w}} F_{c-w} \frac{dq_{e,w}}{d\lambda}, \end{aligned} \quad (\text{A.2})$$

where  $q_{e,w} = Q_{\text{solar}}/A_w$ ,  $q_w = -Q_{\text{convection,w}}/A_w$ , and  $q_c = -Q_c/A_c$ .

The baseline case considers a cylindrical-shaped cavity with  $d_{\text{aperture}} = 0.03$  m,  $d_c = 0.062$  m,  $L_c = 0.124$  m,  $A_c = 41.6A_w$ . The present analysis is valid for any generic cavity shape containing a flat aperture with same aspect ratios. Equation system (A.1)-(A.2) is integrated over the windows

three spectral bands  $l$  to yield a system of  $2 \times 3$  spectrally-independent equations for totally  $2 \times (3 + 1)$  unknowns ( $q_{w,l}, q_{c,l}, T_w, T_c$ ). The remaining two equations are obtained from the relationship  $q_j = \sum_{l=1}^3 q_{j,l}$ , for  $j = \{w, c\}$ . The incoming radiation heat flux per spectral band for each phase is

$$q_{e,w,l} = \frac{q_{e,w}}{\sigma T_{\text{sun}}^4} \int_{\lambda_{1,l}}^{\lambda_{2,l}} e_{\lambda b}(\lambda, T_{\text{sun}}) d\lambda. \quad (\text{A.3})$$

Since the overall total (spectrally-integrated) optical properties of the window are influenced by the temperature  $T_w$ , the problem is solved iteratively. Natural convective losses at the outer face of the window are calculated using a Nusselt correlation [26]

$$\bar{\text{Nu}}_d = 0.825 + \left\{ \frac{0.387 \text{Ra}_d^{1/6}}{\left[1 + (0.492/\text{Pr})^{9/16}\right]^{8/27}} \right\}^2, \quad (\text{A.4})$$

with  $\text{Ra}_d = g\beta(T_w - T_\infty)d_{\text{aperture}}^3$  and  $\text{Pr} = \nu/\alpha$ .  $\alpha = k/(\rho c_p)$  is the thermal diffusivity. The thermophysical properties of air:  $k$ ,  $c_p$ , and  $\nu$ , are computed using polynomial approximations obtained by least-square fitting of tabulated data [58], evaluated at film temperature  $T_{\text{film}} = (T_w + T_\infty)/2$ .  $\beta = 1/T$  is the expansion coefficient [58]. Thus,

$$q_w = \frac{Q_{\text{convection,w}}}{A_w} \bar{h} (T_w - T_\infty) = \frac{\bar{\text{Nu}}_d k}{d_{\text{aperture}}} (T_w - T_\infty). \quad (\text{A.5})$$

$T_{\text{ambient}}$  is assumed to be 298.15 K. Re-radiation losses are obtained by summing:

$$Q_{\text{emitted,w}} = A_w E_w(T_w) \sigma T_w^4, \quad (\text{A.6})$$

$$Q_{\text{reflected,w}} = R_w E_w(T_{\text{source}}) Q_{\text{solar}}, \quad (\text{A.7})$$

and

$$Q_{\text{transmitted,w}} = A_c F_{c-w} V_w(T_{\text{cavity}}) E_c(T_c) \sigma T_c^4, \quad (\text{A.8})$$

for emission, reflection, and transmission losses, respectively.  $E(T)$ ,  $R(T)$ , and  $V(T)$  are the overall total emittance, reflectance, and transmittance



of the window for radiation originating from a blackbody at temperature  $T$ . Energy balance yields:

$$Q_{\text{convection,w}} + Q_{\text{emitted,w}} + Q_{\text{reflected,w}} + Q_{\text{transmitted,w}} = (1 - \eta) Q_{\text{solar}}. \quad (\text{A.9})$$

### A.3 Results

The equation system (A.1)-(A.2) was solved iteratively using the band approximation with fractional functions. Iterative steps were performed by adapting  $T_w$  and  $T_c$  until the convergence criterion  $|1 - q_j^*(T_w, T_c) / q_j|$  was satisfied for both surfaces (window and cavity), with  $q_j^*$  and  $q_j$  being the solutions in consecutive iterations. The overall spectral emittance  $E$ , reflectance  $R$ , and transmittance  $V$  are listed in Tabs. B.1 and B.1, approximated as constants over three spectral bands for quartz and sapphire single-layer windows, based on manufacturer data. The inner cavity surface is taken as black ( $E_c = 1$ ) and no active cooling of the inner window is considered. The solar energy absorption efficiency is defined as the ratio of net power absorbed to the incoming solar radiative power:

$$\eta = \frac{Q_c}{Q_{\text{solar}}}. \quad (\text{A.10})$$

The temperature of the window is shown in Fig. A.2, and that of the cavity wall in Fig. A.3, as a function of the incoming solar radiative flux  $q_{\text{solar}}$ . The parameter is the solar energy absorption efficiency,  $\eta = 0, 0.4, 0.6$ , and  $0.8$ . For validation purposes, the windowless case is included. For the present steady-state case with black walls, radiative equilibrium yields

$$T_c|_{\text{no window}} = \sqrt[4]{\frac{(1 - \eta) q_{\text{solar}}}{\sigma}} \quad (\text{A.11})$$

The stagnation temperature curves for  $\eta = 0$  of the two windowed cases slightly exceed the windowless case, due to a slight greenhouse effect (IR radiation trap) as a result of the higher absorptance in the far IR than in the visible and near IR. As expected,  $T_w$  increases with  $q_{\text{solar}}$ , reaching maximum values (obviously for  $\eta = 0$ ) in the range 1,270 to 1,530 K for the  $q_{\text{solar}}$  range between 2 and 4 MW m<sup>-2</sup>. The window temperature decreases for higher  $\eta$  because of the lower equilibrium temperature and,

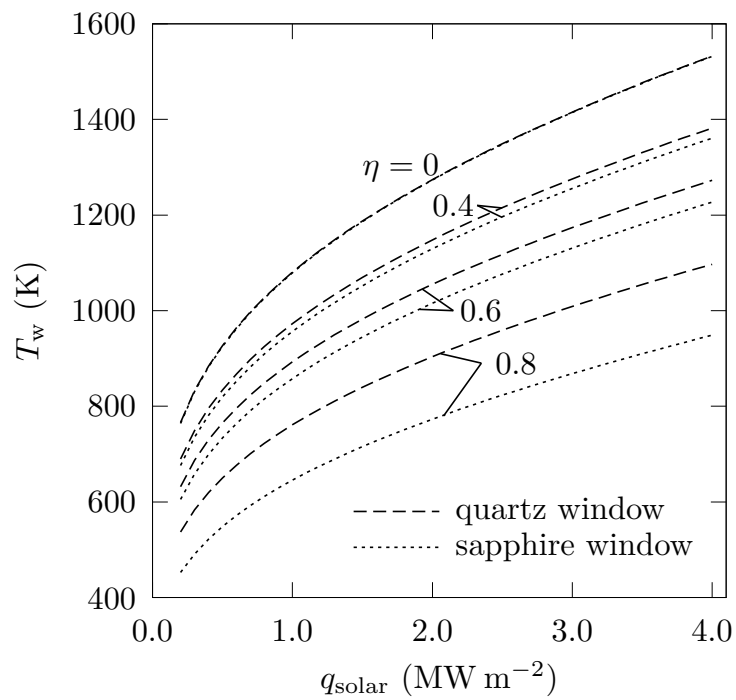


Figure A.2: Temperature of the window as a function of incoming solar radiative flux  $q_{\text{solar}}$ . The parameter is the solar energy absorption efficiency,  $\eta = 0, 0.4, 0.6,$  and  $0.8$ , for both window types and the windowless case.

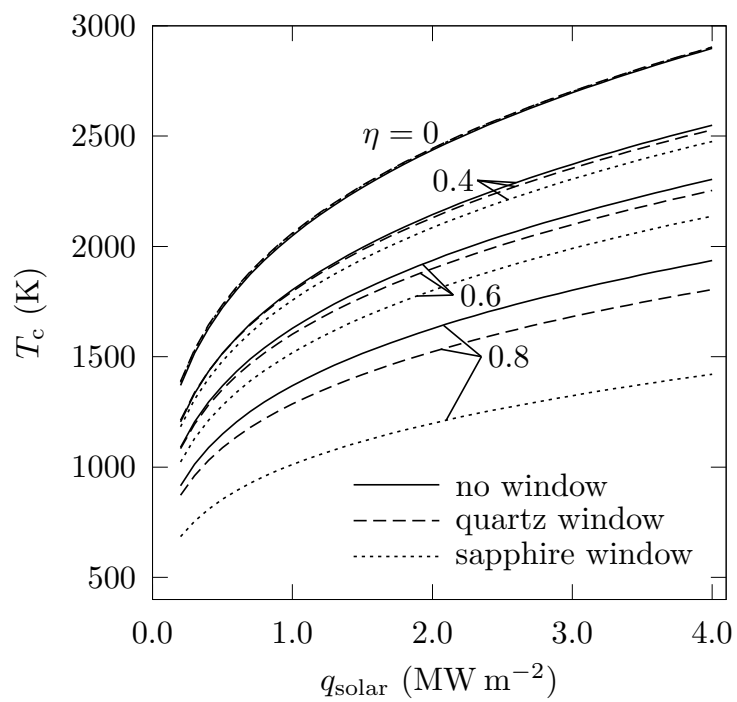


Figure A.3: Temperature of the cavity as a function of incoming solar radiative flux  $q_{\text{solar}}$ . The parameter is the solar energy absorption efficiency,  $\eta = 0, 0.4, 0.6,$  and  $0.8$ , for both window types and the windowless case.

consequently, reduced emission by the cavity. No significant difference in  $T_w$  is observed for the two materials at  $\eta = 0$ . However, the temperature gap increases with  $\eta$ , with the sapphire windows temperature becoming significantly lower than that of the quartz window, for example about 20 % for  $q_{\text{solar}} = 3.0 \text{ MW m}^{-2}$  and  $\eta = 0.8$ . Since for  $T_c$  resulting in the considered  $q_{\text{solar}}$  range, only a minimal fraction of radiative power is emitted at wavelengths longer than  $5 \text{ }\mu\text{m}$ , the lower temperature of sapphire is not a consequence of its different spectral selectivity, but rather of its higher reflection of incoming radiation. Figure A.4 shows the fraction of total losses by emission, reflection, transmission, and natural convection as a function of window temperature for both window types with  $q_{\text{solar}} = 3.0 \text{ MW m}^{-2}$ . The contribution of reflection of incoming radiation to the total losses is higher for the sapphire window due to its higher reflectance in the visible spectrum. The lower transmittance towards the outside of radiation emitted by the cavity does not compensate for these losses, as seen in Fig. A.3. Emission and convection losses by the hot window do not significantly influence the balance. For a given  $\eta$ , a higher  $q_{\text{solar}}$  is needed with a sapphire window to obtain the same  $T_c$  and compensate for reflection losses. For example, for  $T_c \approx 2,000 \text{ K}$  and  $\eta = 0.6$ ,  $q_{\text{solar}} \approx 2.5 \text{ MW m}^{-2}$  is required for quartz, but  $q_{\text{solar}} \approx 3.0 \text{ MW m}^{-2}$  is required for sapphire, resulting in  $T_w \approx 1,125 \text{ K}$  for both window materials.

## A.4 Summary

Radiative transfer within a high-temperature solar cavity-receiver containing a spectrally-selective quartz/sapphire window was analyzed. Results are presented in the form of the calculated temperatures of window and cavity which increase with the incoming radiative flux and decrease with the solar energy absorption efficiency. Both window and cavity temperatures are lower for the sapphire window because of its higher reflectance.

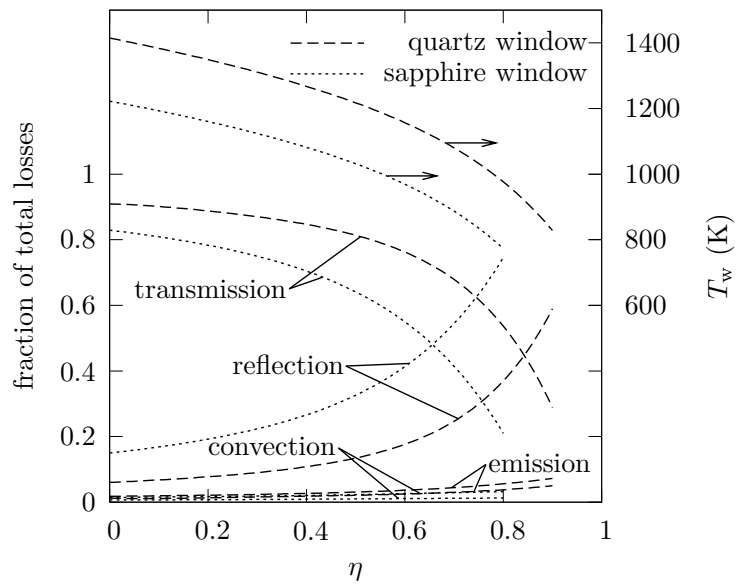


Figure A.4: Fraction of total losses by emission, reflection, transmission, and natural convection on the window as a function of window temperature for both window types with  $q_{\text{solar}} = 3.0 \text{ MW m}^{-2}$ .



# Appendix B

## Optical properties of utilized materials

### B.1 Surfaces

Optical properties for opaque and partially transparent surfaces are obtained from literature or manufacturer data sheets. For computation, the values are approximated as constant over spectral bands.

Several materials' optical properties were used in the present work. Their band-approximated overall spectral emittance  $E_\lambda$ , reflectance  $R_\lambda$ , and transmittance  $V_\lambda$ , are given for quartz (Tab. B.1), sapphire (Tab. B.1), graphite (Tab. B.1), and silicon carbide (Tab. B.1).

### B.2 Gas

Figure B.1 shows the spectral absorption coefficient of methane in function of wavenumber at a temperature of 300 K and partial pressure of 101,325 Pa. It can be noticed that four major absorption bands are present in the

Spectral band	$E_\lambda$	$R_\lambda$	$V_\lambda$
0 – 0.1 $\mu\text{m}$	0.90	0.10	0.00
0.1 – 5 $\mu\text{m}$	0.00	0.06	0.94
5 – $\infty$ $\mu\text{m}$	0.90	0.10	0.00

Table B.1: Band-approximated overall spectral emittance  $E_\lambda$ , reflectance  $R_\lambda$ , and transmittance  $V_\lambda$  of the quartz window [50, 113, 165].

Spectral band	$E_\lambda$	$R_\lambda$	$V_\lambda$
0 – 0.1 $\mu\text{m}$	0.90	0.10	0.00
0.1 – 6 $\mu\text{m}$	0.00	0.15	0.85
6 – $\infty$ $\mu\text{m}$	0.90	0.10	0.00

Table B.2: Band-approximated overall spectral emittance  $E_\lambda$ , reflectance  $R_\lambda$ , and transmittance  $V_\lambda$  of the sapphire window [125].

Spectral band	$E_\lambda$	$R_\lambda$	$V_\lambda$
0 – 0.1 $\mu\text{m}$	0.99	0.01	0.00
0.1 – 5 $\mu\text{m}$	0.90	0.10	0.00
5 – $\infty$ $\mu\text{m}$	0.80	0.20	0.00

Table B.3: Band-approximated overall spectral emittance  $E_\lambda$ , reflectance  $R_\lambda$ , and transmittance  $V_\lambda$  of a graphite plate [132].

Spectral band	$E_\lambda$	$R_\lambda$	$V_\lambda$
0 – 10.8 $\mu\text{m}$	0.90	0.10	0.00
10.8 – 14.8 $\mu\text{m}$	0.60	0.40	0.00
14.8 – $\infty$ $\mu\text{m}$	0.85	0.15	0.00

Table B.4: Band-approximated overall spectral emittance  $E_\lambda$ , reflectance  $R_\lambda$ , and transmittance  $V_\lambda$  of silicon carbide [91, 146].



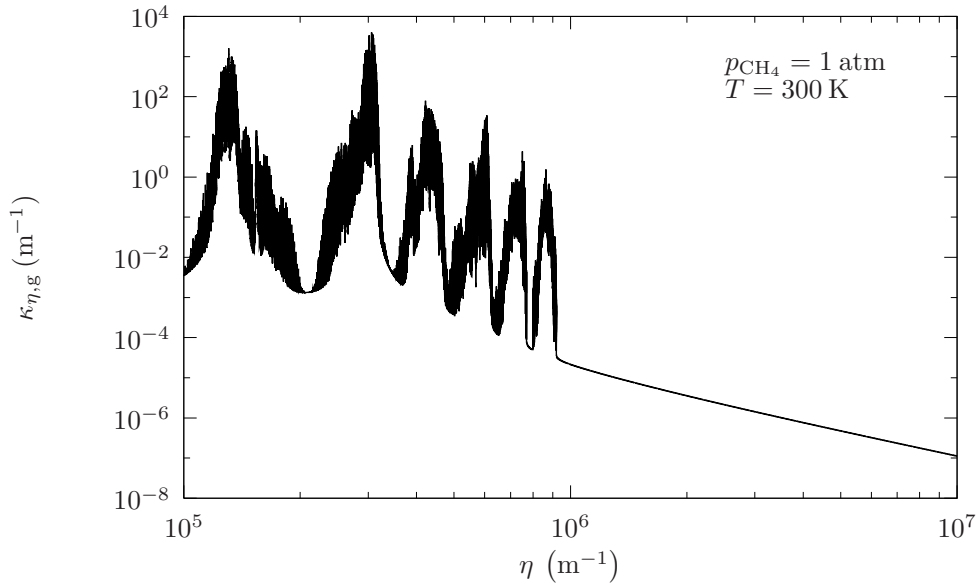


Figure B.1: Spectral absorption coefficient  $\kappa_{\lambda, \text{CH}_4}$  in function of wavenumber  $\eta$  at  $T = 300$  K and a methane partial pressure of 1 atm.

infrared wavelength range, namely at about  $1.65 \mu\text{m}$ ,  $2.30 \mu\text{m}$ ,  $3.50 \mu\text{m}$ , and  $7.40 \mu\text{m}$ . The two smaller bands at  $1.10 \mu\text{m}$ , and  $1.40 \mu\text{m}$  are less relevant since their peak values barely exceed 1. The gas absorbs thus predominantly infrared radiation emitted by the medium, whereas the absorption of visible solar radiation is practically null.

Since molecular gases absorb photons in discrete energy bands, their absorption coefficient varies strongly and rapidly across the wavelength spectrum [95]. To maintain a good precision, models for the absorption coefficient of the gas phase must thus be evaluated at a great number of points across the wavelength spectrum. In this case, as data source, supplied tabulated values for  $\text{CH}_4$  at different partial pressures and temperatures, which were calculated from the HITRAN 2004 spectroscopic database [122], for 10 discrete methane partial pressures between 0.1 and 1.0 atm and 7 temperatures between 300 and 1500 K, are used. Each one of these data sets contains the values of  $\kappa_{\eta, \text{CH}_4}(\eta)$  in function of  $10^6$  discrete wave numbers  $\eta = 1/\lambda$  between  $10^5$  and  $10^7 \text{ m}^{-1}$ .

To reduce the quantity of discrete wave numbers (or wavelengths) from  $10^6$  to a value more suitable for numerical computations, a box model [95] is applied, subdividing the relevant wavelength spectrum in bands  $j$  with

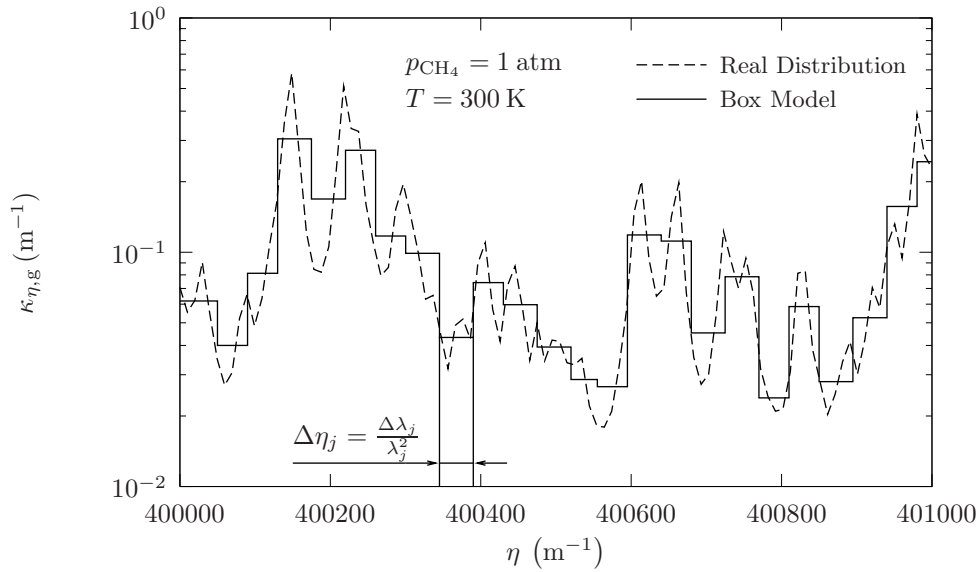


Figure B.2: Illustration of the box model for the spectral absorption coefficient of the gas phase for a selected wavenumber range.

constant absorption coefficient:

$$\bar{\kappa}_{\eta, \text{CH}_4} = \frac{1}{\eta_{j+1} - \eta_j} \int_{\eta_j}^{\eta_{j+1}} \kappa_{\eta, \text{CH}_4}(\eta) d\eta, \quad (\text{B.1})$$

The box model is illustrated in figure B.2 over a small wavenumber, which also permits to perceive the great unsteadiness of the spectral distribution of the gas absorption coefficient. Since the values for  $\kappa_{\eta, \text{CH}_4}(\eta)$  are given only at discrete intervals  $\Delta\eta$ , an analytical solution of the integral in equation B.1 is not possible, requiring a numerical integration method to be applied. In this case, the Simpson Rule is used to approximate the integral by building a quadratic polynomial function over three contiguous values of the spectral absorption coefficient ( $\kappa_{\eta, \text{CH}_4, i-1}$ ,  $\kappa_{\eta, \text{CH}_4, i}$ ,  $\kappa_{\eta, \text{CH}_4, i+1}$ ). If a chosen box interval  $\Delta\eta_{\text{box}, j} = \eta_{j+1} - \eta_j$  contains more than three wavenumber intervals  $\Delta\eta$ , which applies in this case, the composite Simpson rule is used, which leads to the following approximation for the

average absorption coefficient in the interval  $\Delta\eta_{\text{box},j}$ :

$$\bar{\kappa}_{\eta,\text{CH}_4,j} = \frac{1}{\Delta\eta_{\text{box},j}} \int_{\eta_j}^{\eta_{j+1}} \kappa_{\eta,\text{CH}_4}(\eta) d\eta \approx \frac{1}{\Delta\eta_{\text{box},j}} \cdot \frac{\Delta\eta}{3} \cdot \left[ \kappa_{\eta,\text{CH}_4}(\eta_j) + 2 \sum_{i=1}^{n/2-1} \kappa_{\eta,\text{CH}_4}(\eta_{2i}) + 4 \sum_{i=1}^{n/2} \kappa_{\eta,\text{CH}_4}(\eta_{2i-1}) + \kappa_{\eta,\text{CH}_4}(\eta_{j+1}) \right]. \quad (\text{B.2})$$

The suffix  $i$  denotes the discrete wave numbers in the original data set, whereas  $j$  stands for the bands in which the spectrum is subdivided when building the box model.  $N_{\eta\text{band}}$  is the number of wavenumber intervals in one band:

$$N_{\eta\text{band}} = \frac{\Delta\eta_{\text{box},j}}{\Delta\eta}. \quad (\text{B.3})$$

Since the application of the Simpson rule requires  $n$  to be an even number, if equation B.3 yields an odd value, the Simpson rule is used for  $n - 1$  intervals, and the integration over the last  $\Delta\eta$  is approximated by the trapezoidal rule. To obtain the same values in function of the wavelength  $\lambda$ , the relationship  $\lambda = \eta^{-1}$  has to be applied. It has to be noticed that since the  $\Delta\eta$  in the original data set are constant over the given spectrum, the corresponding wavelength intervals do vary according to the following relationship:

$$\Delta\lambda_i = \frac{1}{\eta_i^2} \Delta\eta = \lambda_i^2 \Delta\eta. \quad (\text{B.4})$$

As a consequence of this, the density of data points diminishes for increasing wavelengths, leading thus to the fact that, if constant wavelength bands instead of constant wavenumber bands for the box model are chosen, the precision of the approximation decreases for longer wavelengths.

To find the necessary number of discrete wavenumber/wavelength ranges to obtain an acceptable model, the net radiative power fluxes into each sub-layer for increasingly precise gas models are compared. The precision of the model is improved until the calculated radiative power fluxes start to

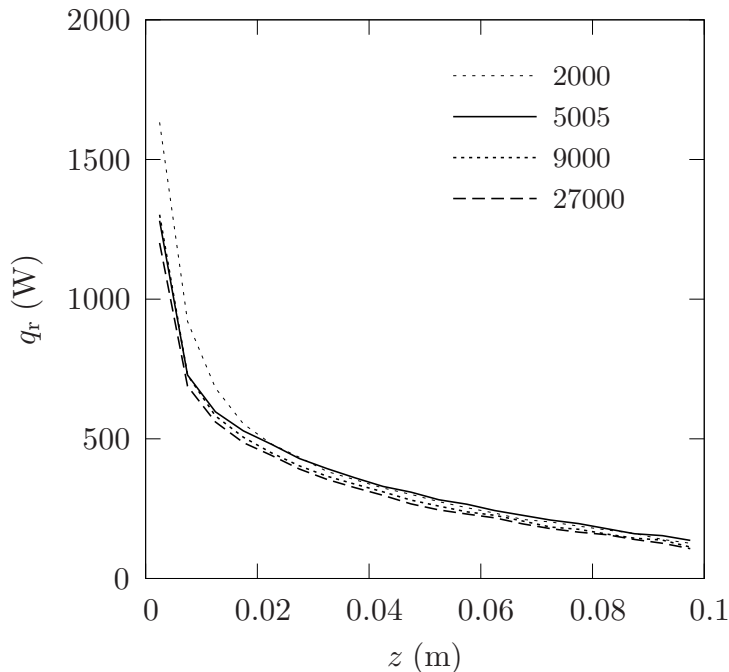


Figure B.3: Comparison of net radiative power  $q_r$  into each sublayer for gas models with 2,000, 9,000, 27,000, and 5,005 discrete wavenumber intervals.

converge, meaning that the precision gain in the results does not longer justify an improvement of the gas model. Radiative power fluxes are computed at  $T_g = 300$  K and  $p_{\text{CH}_4} = 1$  atm since the absorption coefficient is highest at low temperatures and high pressures. Figure B.3 shows the spatial distribution of the net radiative power flux  $\dot{q}_r'''$ . Since  $\kappa_{\lambda, \text{CH}_4}$  does not exceed the value of  $10^{-5}$  for  $10^6 \text{ m}^{-1} < \eta < 10^7 \text{ m}^{-1}$ , it is assumed constant over this range. The remaining range ( $10^5 \text{ m}^{-1} < \eta < 10^6 \text{ m}^{-1}$ ) is then subdivided in 2,000, 9,000, or 27,000 equal wavenumber intervals. It can be noticed that from 9,000 subdivisions upward, a good convergence of  $q_r$  is reached. To further reduce the number of necessary subdivisions, constant values for  $\kappa_{\lambda, \text{CH}_4}$  are assumed also between the four major absorption bands, allowing thus to increase the subdivision density within each band, leading to totally 5,005 discrete wavelength intervals, distributed as shown in table B.5. These ranges are dimensioned to contain the four absorption bands for each temperature and pressure distribution of  $\kappa_{\lambda, \text{CH}_4}$ . This model allows thus for the same box sizes  $\Delta\eta$  as the one with 27,000 subdivisions in the relevant wavenumber intervals, but reduces their total number more

than five times while conserving a good accuracy, as can be seen in figure B.3.

$\eta_{\text{low}}$ ( $\text{m}^{-1}$ )	$\eta_{\text{up}}$ ( $\text{m}^{-1}$ )	subdivisions
100,000	110,000	1
110,000	160,000	1,010
160,000	240,000	1
240,000	330,000	1,818
330,000	400,000	1
400,000	470,000	1,414
470,000	580,000	1
580,000	620,000	808
620,000	10,000,000	1

Table B.5: Characteristics of the box model for the spectral absorption coefficient of the gas phase.

# Appendix C

## Thermochemical properties of utilized materials

The computations presented in this piece of work require several, mostly temperature-dependent, thermochemical properties of the employed gaseous and solid species. They are:

- specific heat  $\bar{c}_p$ ,
- specific enthalpy  $\bar{h}$ ,
- heat conductivity  $k$ , and
- dynamic viscosity  $\mu$ .

As most of the values are required over a wide range of temperatures (usually 300 – 2,000 K ca.), approximate polynomial expressions in function of  $T$ , collected from various sources, are used. In this appendix, the employed functions, together with their sources, are presented.

### C.1 Specific heat

For  $\bar{c}_p$ , the polynomial expression

$$\bar{c}_p \approx a_1 + a_2T + a_3T^{-2} + a_4T^2 \quad (\text{C.1})$$

is used. Parameters  $a_1$ ,  $a_2$ ,  $a_3$ , and  $a_4$  are listed in Tab. C.1. Source is [18] unless stated otherwise.

species	$a_1$ J mol <sup>-1</sup> K <sup>-1</sup>	$a_2$ J mol <sup>-1</sup> K <sup>-2</sup>	$a_3$ J K mol <sup>-1</sup>	$a_4$ J mol <sup>-1</sup> K <sup>-3</sup>
Ar	20.785	0	0	0
C (graphite) <sup>1</sup>	14.58	9.957·10 <sup>-3</sup>	-8.50·10 <sup>5</sup>	2.40·10 <sup>-6</sup>
CH <sub>4</sub>	11.93	7.765·10 <sup>-2</sup>	1.4·10 <sup>5</sup>	-1.841·10 <sup>-5</sup>
C <sub>2</sub> H <sub>2</sub>	43.63	3.165·10 <sup>-2</sup>	-7.5·10 <sup>5</sup>	-6.31·10 <sup>-6</sup>
C <sub>2</sub> H <sub>4</sub>	39.29	5.713·10 <sup>-2</sup>	-1.3·10 <sup>6</sup>	0
C <sub>2</sub> H <sub>6</sub>	28.19	1.226·10 <sup>-1</sup>	-9.1·10 <sup>5</sup>	-2.784·10 <sup>-5</sup>
CO	30.96	2.44·10 <sup>-3</sup>	-2.8·10 <sup>5</sup>	0
CO <sub>2</sub>	51.13	4.37·10 <sup>-3</sup>	-1.47·10 <sup>6</sup>	0
H <sub>2</sub>	26.88	3.59·10 <sup>-3</sup>	1.1·10 <sup>5</sup>	0
H <sub>2</sub> O	34.38	7.84·10 <sup>-3</sup>	-4.2·10 <sup>5</sup>	0

Table C.1: Parameters for the polynomial approximation for specific heat  $\bar{c}_p$ . Source is [18].

## C.2 Specific enthalpy

For  $\bar{h}_p$ , the polynomial expression for  $\bar{c}_p$  (Eqn. (C.1)) is integrated over  $T$  to yield:

$$\bar{h}(T) \approx \bar{h}_{T_{\text{ref}}}^f + a_1 (T - T_{\text{ref}}) + \frac{a_2}{2} (T^2 - T_{\text{ref}}^2) - a_3 \left( \frac{1}{T} - \frac{1}{T_{\text{ref}}} \right) + \frac{a_4}{3} (T^3 - T_{\text{ref}}^3). \quad (\text{C.2})$$

The formation enthalpies  $\bar{h}_{T_{\text{ref}}}^f$  at reference temperature  $T_{\text{ref}} = 298$  K are given in Tab. C.2. Source is [18] unless stated otherwise.

## C.3 Thermal conductivity and viscosity

For  $k$  and  $\mu$ , values are computed based on kinetic theory [133], assuming ideal gases of hard spherical particles:

$$k = \frac{25\pi\bar{c}_V}{32N_A} \left( \frac{k_B T}{\pi m_a} \right)^{1/2} \frac{1}{\pi\zeta^2}, \quad (\text{C.3})$$

$$\mu = \frac{5\pi}{16} \left( \frac{k_B T}{\pi m_a} \right)^{1/2} \frac{m_a}{\pi\zeta^2}, \quad (\text{C.4})$$



species	$\bar{h}_{T_{\text{ref}}}^f$ J mol <sup>-1</sup> K <sup>-1</sup>
Ar	0
C (graphite) <sup>2</sup>	0
CH <sub>4</sub>	-74,900
C <sub>2</sub> H <sub>2</sub>	226,700
C <sub>2</sub> H <sub>4</sub>	52,500
C <sub>2</sub> H <sub>6</sub>	-84,700
CO	-110,500
CO <sub>2</sub>	-393,500
H <sub>2</sub>	0
H <sub>2</sub> O	-241,800

Table C.2: Specific enthalpies of formation at  $T_{\text{ref}} = 298$  K. Source is [18].

where  $m_a =$  is the atomic mass of the considered species,  $k_B$  is the Boltzmann constant,  $N_A$  the Avogadro number, and  $\zeta$  is the collision diameter, listed in Tab. C.3 for all relevant gaseous species. Constant-volume heat capacity is obtained from the relationship  $c_V = (\bar{c}_p - \bar{R}) / \bar{M}$ , with  $\bar{c}_p$  determined as shown in Sec. C.1. If several gaseous components are present in relevant quantities, the values are computed for the gas phase by a weighted sum for all species using their molar concentration as weight function.

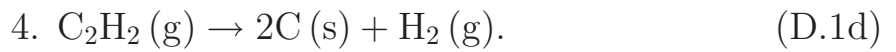
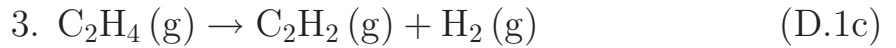
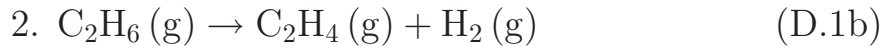
species	$\zeta$ Å
Ar	3.542
CH <sub>4</sub>	3.758
C <sub>2</sub> H <sub>2</sub>	4.033
C <sub>2</sub> H <sub>4</sub>	4.163
C <sub>2</sub> H <sub>6</sub>	4.443
CO	3.690
CO <sub>2</sub>	3.941
H <sub>2</sub>	2.827
H <sub>2</sub> O	2.641

Table C.3: Collision diameters used for the determination of  $k$  and  $\mu$  for all relevant gaseous species [28].

# Appendix D

## Chemical reaction model

The reaction kinetic model for thermal cracking of CH<sub>4</sub>, determined by DLR [161], considers four reactions:



The corresponding reaction rates are given by

$$\bar{r}_j = \frac{1}{\nu_{\text{reactant},j}} \frac{dn_{\text{reactant},j}}{dt} = k_{0,j} \sqrt{T_{\text{bulk}}} \exp\left(-\frac{E_{a,j}}{\bar{R}T}\right) \bar{\rho}_{\text{reactant},j}^{m_j}, \quad (\text{D.2})$$

for each reaction  $1 \leq j \leq 4$ . Experimentally determined values for activation energy  $E_a$ , pre-exponential factor  $k_0$ , and reaction order  $m$  are given in Tab. D.

reaction	$E_a$ kJ mol <sup>-1</sup>	$\log k_0$ $\log[\text{s}^{-1} \text{K}^{-0.5} (\text{mol m}^{-3})]^{(1-m)}$	$m$
1	397.1	12.59	1.280
2	135.6	8.856	1.101
3	68.18	5.452	1.126
4	31.38	1.513	1.970

Table D.1: Experimentally determined kinetic parameters for the rate law (Eq. D.2).



# Appendix E

## Scale-up reactor design

### E.1 Introduction

Design of the scale-up reactor using the numerical model presented in Sec. 4.3 was a task of the SOLHYCARB project and was carried out jointly between the involved project partners CNRS-PROMES (determination of material and geometrical constraints based on experience with reactor prototypes), DLR (chemical kinetics, see also Appendix D), WIS (dimensioning of the concentrating system), and ETH (building of simulation and numerical calculations). Several iterative steps were necessary to reach the final design, used in Chapters 4 and 5. This appendix chapter cannot show the entire process leading to the final result, but is aimed at explain the conclusive choice more detailedly and to give some indications for possible further improvements.

### E.2 Heliostat field<sup>1</sup>

Considering a direct insolation of  $0.85 \text{ kW m}^{-2}$ , a realistic  $\cos\phi = 0.90$ , heliostat reflectivity 0.92, blocking, shadowing and attenuation 0.05, possible spillage around the CPCs 0.03, optical efficiency of the CPCs cluster 0.94, a value of about  $16,500 \text{ m}^2$  of collector reflective surface is needed, which means about  $18,000 \text{ m}^2$  total heliostat surface. This calculus is valuable for ideal heliostats (without tracking and surface errors). In fact the total heliostat surface must be significant large with big losses by spillage around

---

<sup>1</sup>This section summarizes the main results of the heliostat field and secondary concentrator (CPC) design performed by Dr. A. Segal from WIS [134]

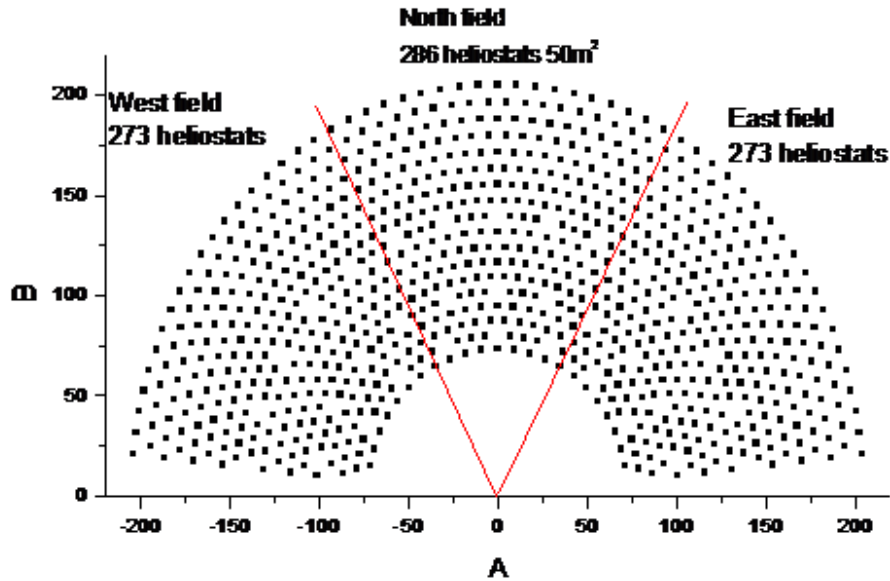


Figure E.1: Schematic top view of the heliostat field (image by WIS).

the CPC entrance. Three fields of heliostats were built so that the acceptance angle of the CPCs is no more than  $30^\circ$ , based on heliostats having an area of  $25 \text{ m}^2$ . Various heliostat dimensions ( $100 \text{ m}^2$ ,  $50 \text{ m}^2$  and  $25 \text{ m}^2$ ) were simulated, the  $25 \text{ m}^2$  ones giving the best results. The field obtained in this concept, for a tower with 80 m height, has the rear row at about 205 m distant. But at this distance even an ideal heliostat gives quite large image on the target. A schematic of the heliostat field is given in Fig. E.1. The spillage is considerable if the aim power of 10 MW is preserved, but this value can be attained at least at the design point (Equinox, Noon), see Tab E.4. The lateral fields will have a different behavior in the morning or afternoon e.g. the West field will be advantaged at the beginning of the day, and the East field will be advantaged afternoon (see Tab E.4, calculated for the hour 9:00, where the insolation has been preserved at the same value in order to illustrate the influence of the Sun position only).

## E.3 Reactor geometry

### E.3.1 Absorber tube diameter

For stability reasons, based on suggestions by the tube manufacturer, minimum tube diameters of 14 cm (outer) and 8 cm (inner) were considered. Thinner tubes would be desirable as they allow for more efficient heat transfer reaching an optimum for  $d_{\text{absorber,o}} \approx 6$  cm, increasing the amount of totally reacted per unit of occupied section area inside the reactor. Lower diameters prove to be counterproductive as the ratio of wall volume to inner volume increases.

### E.3.2 Reactor height

For the reactor height, which is at the same time the absorber tube length, the main constraint is given by the stability of the employed graphite tubes. However, it was deemed possible to connect several tubes in series in order to reduce thermal stress on the components. For this reason, no upper limit for the cavity height is assumed. On the other hand it is desirable to have absorber tubes long enough to reach flow velocities generating turbulent conditions in order to enhance heat transfer into the medium.

### E.3.3 Aperture design

While the absorber tubes require a homogeneous distribution of the radiation inside the receiver cavity, the size of the concentrated radiation spot makes it necessary to position the apertures as close as possible to each other to avoid spillage losses between them. These two objectives clearly are in contrast. The main difficulty is given by the high solar concentrations needed and thus the usage of CPCs, whose acceptance angle (in this case  $30^\circ$ ), requires their positioning towards different azimuthal angles in order to cover the entire heliostat field. The first possibility is that of having adjacent apertures/CPCs, but positioned on a curved, rather than a flat, surface. However, this would significantly reduce the available space inside the cavity.

Considering that radiation is usable only if directed towards the CPCs

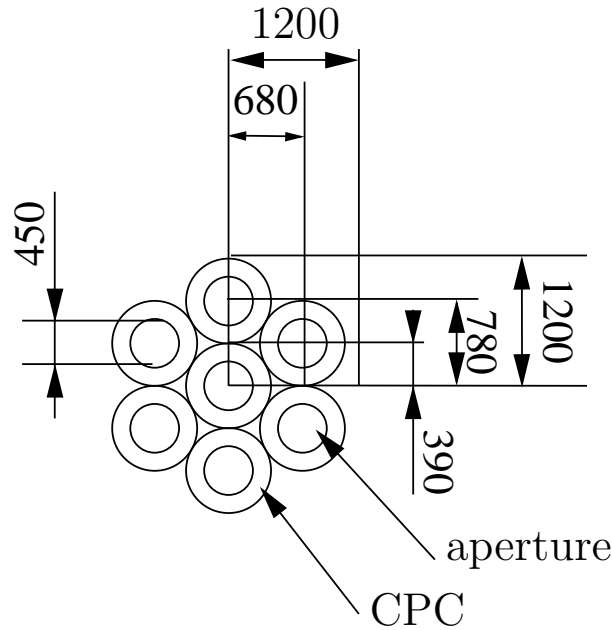


Figure E.2: Arrangement of a single CPC array.

oriented in the right direction, the fact of having all CPCs closely packed in one single group in order to reduce spillage losses, becomes unimportant. A good solution seems to be using several arrays of most densely possible packed apertures and CPCs. These arrays can be positioned facing different azimuthal angles. To obtain close to regular shapes of these in order to reduce spillage losses, the total number of apertures needs to be increased and thus their size reduced. For the receiver, 3 arrays of 7 apertures ( $d_{\text{aperture}} = 45$  cm, to maintain the nominal power of  $10 \text{ MW}_{\text{th}}$  through the apertures) each, arranged in a flower shape (see Fig. E.2), are proposed. The CPC axes of each array are positioned at  $60^\circ$  from those of the adjacent one.

### E.3.4 Single or multiple cavity

Based on the aperture design, two different concepts were taken in consideration: a single and a multiple (three) cavity design. Simulation results for the two different cavity types showed the differences in performance (process temperature, chemical conversion, and energy efficiency) to be minimal. This reduced the choice between the two concepts to a constructional issue. The choice fell thus on the multiple cavity design which allows better



adaptation of the aperture position to the concentrating system. Furthermore, the variation of the radiative flux coming from each dedicated field part, depending on the time of day, can be better accounted for by varying the mass flow.

### E.3.5 Cavity width and number of absorber tubes

To account for the different energy fluxes entering the receiver at the center and those at the sides, the possibility of having differently sized cavities is considered. A generic design of the cavity is shown in Fig. 4.5. The cavity height  $H$  already being determined by the length of the absorber tubes, the cavity width  $W$  was optimized for performance. Once defined  $W$ , the depth  $D$  is chosen in order to minimize the temperature difference between the absorber tubes. For the chosen configurations,  $\Delta T$  between the hottest and the coldest tube is  $< 10$  K at the design point. Viewed from the top the cavity assumes the shape of a circular section having chord length  $W$  and height  $D$ . Each absorber tube is positioned leaving a gap of 1 cm to the adjacent one and to the wall. The array of absorber is then positioned as close as possible towards the centerline of the cavity. Dimensions of the center and lateral cavities are listed in Tab. 4.2. A schematic view of the positioning of the three absorber cavities on a tower receiver is shown in Fig. 4.6. The perpendicular of each face forms an angle of  $60^\circ$  with that of the adjacent faces. Except for those constraints, the positioning (e.g., the tilt angle, here  $55^\circ$ ) of the cavities is adaptable to constructional issues and to the concentrating field.

## E.4 Reactor performance

The computed reactor performance, using the model presented in Chapter 4 for the operating points provided by WIS in Sec. E.2 (assuming product inlet and outlet temperatures of 1173 and 1873 K), are given in Tab. E.4 and E.4.

		North	East	West	total
Values computed by WIS					
$N_{\text{heliostats}}$		286	273	273	832
power to target	kW	4,862	4,338	4,326	13,526
spillage	kW	650	610	598	1,858
into CPCs	kW	4,151	3,728	3,728	11,607
CPC losses	kW	205	184	184	573
into receiver	kW	3,946	3,544	3,544	11,034
average flux	MW m <sup>-2</sup>	3.54	3.18	3.18	3.30
Values computed during this thesis					
$\dot{m}_{\text{CH}_4,\text{in}}$	kg s <sup>-1</sup>	0.254	0.221	0.221	0.696
$\dot{m}_{\text{H}_2,\text{out}}$	kg s <sup>-1</sup>	0.063	0.055	0.053	0.173
$\dot{m}_{\text{C},\text{out}}$	kg s <sup>-1</sup>	0.182	0.157	0.157	0.494
$X_{\text{CH}_4}$		1.000	1.000	1.000	1.000
$Y_{\text{H}_2}$		0.990	0.988	0.998	0.994
$Q_{\text{thermal}}$	kW	3,006	2,621	2,622	8,249
$Q_{\text{chemical}}$	kW	1,683	1,473	1,473	4,629
$\eta_{\text{thermal}}$		0.762	0.740	0.740	0.748
$\eta_{\text{chemical}}$		0.427	0.417	0.417	0.420

Table E.1: Reactor performance at design point,  $T_{\text{out}} = 1,870$  K.

		North	East	West	total
Values computed by WIS					
$N_{\text{heliostats}}$		286	273	273	832
power to target	kW	4,448	3,272	4,414	12,134
spillage	kW	656	925	616	2,197
into CPCs	kW	3,791	2,347	3,798	9,936
CPC losses	kW	188	115	188	491
into receiver	kW	3,603	2,232	3,610	9,445
Values computed during this thesis					
$\dot{m}_{\text{CH}_4,\text{in}}$	$\text{kg s}^{-1}$	0.227	0.117	0.227	0.571
$\dot{m}_{\text{H}_2,\text{out}}$	$\text{kg s}^{-1}$	0.057	0.029	0.056	0.142
$\dot{m}_{\text{C},\text{out}}$	$\text{kg s}^{-1}$	0.164	0.086	0.161	0.411
$X_{\text{CH}_4}$		1.000	1.000	1.000	1.000
$Y_{\text{H}_2}$		0.991	0.995	0.987	0.995
$Q_{\text{thermal}}$	kW	2,687	1,393	2,685	6,765
$Q_{\text{chemical}}$	kW	1,497	764	1,521	3,782
$\eta_{\text{thermal}}$		0.746	0.624	0.744	0.716
$\eta_{\text{chemical}}$		0.416	0.342	0.422	0.400

Table E.2: Reactor performance at equinox, 9:00,  $T_{\text{out}} = 1,870$  K

## E.5 Conclusions

Design and optimization of the cavity shape and dimensions yielded a reasonable reactor concept which was useful for the task of estimate the performance of the 10 MW scale-up process for solar thermal cracking of methane. However, this design can only serve as a starting point for a real reactor. A principal issue which needs a solution is that of the very high concentrations needed, which require small aperture areas and, therefore, high spillage losses. The fact of using 3D CPCs additionally contributes to the problem, since the total aperture area needs to be divided among the parts of the heliostat field due to the acceptance angle of the CPCs. While one solution could be the employment of concentrating heliostats, another one could be given by using, instead of three aperture clusters with 3D CPCs, a single, bigger one, having rectangular apertures and using 2D CPCs or asymmetric concentrators with their axis horizontally to the ground in order to avoid the acceptance angle issue, as proposed by [74]. On the other hand, it would have to be proven the desired concentrations are attainable with such a design. Additionally, very elongate windows would be required, which could be a constructional issue.

# List of Figures

2.1	Scheme of the 1D system domain consisting of a particle-gas mixture exposed to an external source of concentrated solar radiation and undergoing heterogeneous thermochemical reaction. . . . .	7
2.2	Spectral extinction and scattering efficiency factors of carbon particles for selected particle diameters $d_p = 1, 2.5, 5,$ and $10 \mu\text{m}$ . . . . .	14
2.3	Scattering phase function of the particles for selected particle diameters $d_p = 1$ and $10 \mu\text{m}$ , at radiation wavelength of $\lambda = 0.5 \mu\text{m}$ . . . . .	14
2.4	Scattering phase function of the particles for selected particle diameters $d_p = 1$ and $10 \mu\text{m}$ , at radiation wavelength of $\lambda = 2 \mu\text{m}$ . . . . .	15
2.5	Transient particle temperature at $z = L/2$ as a function of time for selected inlet/initial particle diameters $d_{p,0} = 1, 2.5, 5,$ and $10 \mu\text{m}$ . . . . .	15
2.6	Transient spectral absorption and extinction coefficients at $z = L/2$ for $f_{V,0} = 10^{-5}$ , $\lambda = 0.5 \mu\text{m}$ , and for inlet/initial particle diameters $d_{p,0} = 1$ and $10 \mu\text{m}$ . . . . .	16
2.7	Steady-state cumulative absorbed fraction of external radiation along the slab for selected inlet/initial particle diameters $d_{p,0} = 1, 2.5, 5,$ and $10 \mu\text{m}$ . . . . .	17
2.8	Steady-state particle temperature profile along the slab for selected inlet/initial particle diameters $d_{p,0} = 1, 2.5, 5,$ and $10 \mu\text{m}$ . . . . .	18

2.9	Steady-state particle temperature profile along the slab for selected inlet/initial particle volume fractions $f_{V,0} = 0.5 \cdot 10^{-5}, 1 \cdot 10^{-5}, 5 \cdot 10^{-5}$ . . . . .	19
2.10	Steady-state particle temperature profile along the slab for selected inlet/initial $\text{CH}_4$ molar fractions $\bar{x}_{\text{CH}_4,0} = 0.1, 0.5,$ and 1. . . . .	19
3.1	Scheme of the 5 KW particle-flow solar chemical reactor prototype. . . . .	23
3.2	Schematic of the solar experimental setup at both facilities. . . . .	25
3.3	$\text{CH}_4$ conversion and $\text{H}_2$ yield obtained for all solar experimental runs at ETH's high-flux solar simulator, grouped according to the laden carbon particles. . . . .	28
3.4	Hydrogen yield $Y_{\text{H}_2}$ in function of inlet particle volume fraction $f_{V,\text{in}}$ for different laden particle types. . . . .	29
3.5	Hydrogen yield $Y_{\text{H}_2}$ in function of inlet solar $q_{\text{solar}}$ for different laden particle types. . . . .	29
3.6	Hydrogen yield $Y_{\text{H}_2}$ in function of inlet particle mass flow rate $\dot{m}_{p,\text{in}}$ and different laden particle types. . . . .	31
3.7	Methane conversion and hydrogen yield (see Eqs. (3.4) and (3.5)) for all 20 solar experimental runs at PSI's high-flux solar furnace, ordered by increasing inner reactor wall temperature $T_{\text{wall},i}$ . . . . .	34
3.8	Variation of the methane conversion and hydrogen yield as a function of the inlet particle volume fraction $f_{V,\text{in}}$ . . . . .	35
3.9	Variation of the methane conversion and hydrogen yield as a function of the incoming solar radiative flux $q_{\text{solar}}$ . . . . .	36
3.10	Variation of the methane conversion and hydrogen yield as a function of the inlet gas volume flow $\dot{V}_{g,\text{in}}$ . . . . .	37
3.11	Variation of the methane conversion and hydrogen yield as a function of the inlet $\text{CH}_4$ volume fraction $\bar{x}_{\text{CH}_4,\text{in}}$ . . . . .	38
3.12	Variation of the solar-to-chemical energy conversion efficiency, experimentally obtained ( $\eta_{\text{thermal}}, \bullet$ ) and numerically computed assuming $\bar{x}_{\text{CH}_4,\text{in}} = 1$ ( $\eta_{\text{thermal}}^*, \circ$ ), as a function of the inlet particle volume fraction $f_{V,\text{in}}$ . . . . .	39

3.13	Variation of the solar-to-chemical energy conversion efficiency, experimentally obtained ( $\eta_{\text{thermal}}, \bullet$ ) and numerically computed assuming $\bar{x}_{\text{CH}_4, \text{in}} = 1$ ( $\eta_{\text{thermal}}^*, \circ$ ), as a function of the incoming solar radiative flux $q_{\text{solar}}$ . . . . .	40
3.14	Variation of the solar-to-chemical energy conversion efficiency, experimentally obtained ( $\eta_{\text{thermal}}, \bullet$ ) and numerically computed assuming $\bar{x}_{\text{CH}_4, \text{in}} = 1$ ( $\eta_{\text{thermal}}^*, \circ$ ), as a function of the inlet gas volume flow $\dot{V}_{\text{g, in}}$ . . . . .	41
3.15	Variation of the experimentally obtained solar-to-chemical energy conversion efficiency as a function of the inlet $\text{CH}_4$ volume fraction $\bar{x}_{\text{CH}_4, \text{in}}$ . . . . .	42
3.16	SEM of filtered solid products, using laden carbon particles of type: (a) Fluka 05100; (b) Fluka 05120; and (c) PAK 800. . . . .	44
3.17	Particle volume distribution (probability density $v_d$ and cumulative $V_d$ ) for the reacting particles (Cabot Black Pearls 2000 carbon black) and filtered products after run #44. . . . .	45
3.18	SEM images of seed Cabot Black Pearl 2000 carbon black particles. . . . .	46
3.19	SEM images of filtered carbonaceous product after run #44. . . . .	46
3.20	SEM images of filtered carbonaceous product after run #44. . . . .	47
4.1	Schematic of the solar cavity receiver configuration. 1 = window, 2 = cavity, 3-6 = absorber tubes. . . . .	51
4.2	Schematic longitudinal section view of an absorber tube. . . . .	52
4.3	Experimentally measured and model simulated outer absorber tube temperature for 65 solar experimental runs with the 10 kW solar reactor prototype (ordered by increasing $T_{\text{absorber, o}}$ ). . . . .	59
4.4	Experimentally measured and model simulated $\text{H}_2$ concentration at the outlet for 65 solar experimental runs with the 10 kW solar reactor prototype (ordered by increasing $\bar{x}_{\text{CH}_4, \text{out}}$ ). . . . .	60
4.5	Front and top view of the 10 MW solar reactor, consisting of a cavity-receiver with seven apertures, each having a hexagonal CPC, and containing an array of 26 (North) or 20 (East/West) tubular absorbers (dimensions in mm). . . . .	62

4.6	Top view of the three cavity-receivers, each one facing its dedicated portion of the heliostat field (North, East, and West), positioned at an angle of $60^\circ$ from each other to allow efficient capturing of the incoming concentrated solar radiation by the CPCs. . . . .	63
4.7	Variation of the outlet gas temperature $T_{\text{out}}$ with inlet $\text{CH}_4$ mass flow rate $\dot{m}_{\text{CH}_4, \text{in}}$ for the North (a) and East/West (b) scale-up cavity-receivers. The parameter is the solar radiative flux through the reactor aperture $q_{\text{solar}} = 0.6, 1.2, 1.8, 2.4, 3.0,$ and $3.6 \text{ MW m}^{-2}$ . . . . .	65
4.8	Variation of the thermal energy conversion efficiency $\eta_{\text{thermal}}$ as a function of the inlet $\text{CH}_4$ mass flow rate $\dot{m}_{\text{CH}_4, \text{in}}$ for the North (a) and East/West (b) scale-up cavity-receivers. The parameter is the solar radiative flux through the reactor aperture $q_{\text{solar}} = 0.6, 1.2, 1.8, 2.4, 3.0,$ and $3.6 \text{ MW m}^{-2}$ . . . . .	66
4.9	Variation of the thermal energy conversion efficiency $\eta_{\text{chemical}}$ as a function of the inlet $\text{CH}_4$ mass flow rate $\dot{m}_{\text{CH}_4, \text{in}}$ for the North (a) and East/West (b) scale-up cavity-receivers. The parameter is the solar radiative flux through the reactor aperture $q_{\text{solar}} = 0.6, 1.2, 1.8, 2.4, 3.0,$ and $3.6 \text{ MW m}^{-2}$ . . . . .	67
4.10	Variation of the chemical energy conversion efficiency $\eta_{\text{chemical}}$ as a function of outlet gas temperature $T_{\text{out}}$ for the North scale-up cavity-receivers. The parameter are the solar radiative flux through the reactor aperture $q_{\text{solar}} = 1.2, 1.8, 2.4, 3.0,$ and $3.6 \text{ MW m}^{-2}$ , and the inlet $\text{CH}_4$ mass flow $\dot{m}_{\text{CH}_4, \text{in}} = 0.08, 0.14, 0.20,$ and $0.26 \text{ kg s}^{-1}$ . . . . .	68
5.1	Solar reactor configuration consisting of a cavity-receiver with a windowless slab aperture containing an array of tubular absorbers, through which a reacting mixture of steam and carbonaceous particles flow. A 2D-CPC is incorporated at the aperture. . . . .	71
5.2	Longitudinal section view of an absorber tube. . . . .	73



5.3	Particle number ( $f_d$ ) and volume ( $v_d$ ) distribution probability densities of the beech charcoal feedstock and the 11 discrete size intervals used for computation of the radiative properties of the particle suspension. . . . .	75
5.4	Averaged experimentally measured (18 runs at 9 different $T_{\text{absorber,o}}$ and theoretically calculated reaction extent in function of $T_{\text{absorber,o}}$ for the 3 kW reactor prototype. . . . .	77
5.5	Variation of the outlet gas temperatures $T_{\text{out}}$ with inlet H <sub>2</sub> O mass flow rate $\dot{m}_{\text{H}_2\text{O,in}}$ for the North (a) and East/West (b) scale-up cavity-receivers. The parameter is the solar radiative flux through the reactor aperture $q_{\text{solar}} = 1.5, 2.0, 2.5, 3.0, 3.5,$ and $4.0 \text{ MW m}^{-2}$ and the inlet H <sub>2</sub> O:C ratio is 2.0. . . . .	81
5.6	Variation of the extent of chemical reaction $X_C$ with inlet H <sub>2</sub> O mass flow rate $\dot{m}_{\text{H}_2\text{O,in}}$ for the North (a) and East/West (b) scale-up cavity-receivers. The parameter is the solar radiative flux through the reactor aperture $q_{\text{solar}} = 1.5, 2.0, 2.5, 3.0, 3.5,$ and $4.0 \text{ MW m}^{-2}$ and the inlet H <sub>2</sub> O:C ratio is 2.0. . . . .	82
5.7	Variation of the thermal energy conversion efficiency $\eta_{\text{thermal}}$ with inlet H <sub>2</sub> O mass flow rate $\dot{m}_{\text{H}_2\text{O,in}}$ for the North (a) and East/West (b) scale-up cavity-receivers. The parameter is the solar radiative flux through the reactor aperture $q_{\text{solar}} = 1.5, 2.0, 2.5, 3.0, 3.5,$ and $4.0 \text{ MW m}^{-2}$ and the inlet H <sub>2</sub> O:C ratio is 2.0. . . . .	83
5.8	Variation of the chemical energy conversion efficiency $\eta_{\text{chemical}}$ with inlet H <sub>2</sub> O mass flow rate $\dot{m}_{\text{H}_2\text{O,in}}$ for the North (a) and East/West (b) scale-up cavity-receivers. The parameter is the solar radiative flux through the reactor aperture $q_{\text{solar}} = 1.5, 2.0, 2.5, 3.0, 3.5,$ and $4.0 \text{ MW m}^{-2}$ and the inlet H <sub>2</sub> O:C ratio is 2.0. . . . .	84
A.1	Schematic of the solar cavity receiver configuration. . . . .	95
A.2	Temperature of the window as a function of incoming solar radiative flux $q_{\text{solar}}$ . The parameter is the solar energy absorption efficiency, $\eta = 0, 0.4, 0.6,$ and $0.8,$ for both window types and the windowless case. . . . .	98

---

A.3	Temperature of the cavity as a function of incoming solar radiative flux $q_{\text{solar}}$ . The parameter is the solar energy absorption efficiency, $\eta = 0, 0.4, 0.6,$ and $0.8,$ for both window types and the windowless case. . . . .	99
A.4	Fraction of total losses by emission, reflection, transmission, and natural convection on the window as a function of window temperature for both window types with $q_{\text{solar}} = 3.0 \text{ MW m}^{-2}.$ . . . . .	101
B.1	Spectral absorption coefficient $\kappa_{\lambda, \text{CH}_4}$ in function of wavenumber $\eta$ at $T = 300 \text{ K}$ and a methane partial pressure of $1 \text{ atm}.$	105
B.2	Illustration of the box model for the spectral absorption coefficient of the gas phase for a selected wavenumber range. .	106
B.3	Comparison of net radiative power $q_r$ into each sublayer for gas models with $2,000, 9,000, 27,000,$ and $5,005$ discrete wavenumber intervals. . . . .	108
E.1	Schematic top view of the heliostat field (image by WIS). . .	118
E.2	Arrangement of a single CPC array. . . . .	120

# List of Tables

- 2.1 Baseline parameters. . . . . 13
- 3.1 Operational parameters and results of the solar experimental runs at ETH’s high-flux solar simulator using various types of active carbon as seed particles. . . . . 30
- 3.2 Operational parameters and results of the solar experimental runs at PSI’s solar furnace using Cabot Black Pearls 2000 as seed particles. . . . . 33
- 3.3 Properties of seed (upstream) and filtered (downstream) active carbon (AC) and carbon black (CB) particles. . . . . 43
- 4.1 Coefficients  $a$ ,  $b$ , and  $c$  determined by least-square fitting of a second-order polynomial function to simulated radiative heat transfer rates, obtained with MC for the inner absorber tube geometries used during experimentation. . . . . 57
- 4.2 Optimized dimensions of the scale-up cavity-receivers. . . . . 61
- 5.1 Coefficients  $a$ ,  $b$ , and  $c$  determined by least-square fitting of a second-order polynomial function to radiative heat transfer rates obtained by MC for the 3 KW and the 10 MW reactor design. . . . . 74
- B.1 Band-approximated overall spectral emittance  $E_\lambda$ , reflectance  $R_\lambda$ , and transmittance  $V_\lambda$  of the quartz window [50, 113, 165]. 103
- B.2 Band-approximated overall spectral emittance  $E_\lambda$ , reflectance  $R_\lambda$ , and transmittance  $V_\lambda$  of the sapphire window [125]. . . . 104
- B.3 Band-approximated overall spectral emittance  $E_\lambda$ , reflectance  $R_\lambda$ , and transmittance  $V_\lambda$  of a graphite plate [132]. . . . . 104

---

B.4	Band-approximated overall spectral emittance $E_\lambda$ , reflectance $R_\lambda$ , and transmittance $V_\lambda$ of silicon carbide [91, 146]. . . . .	104
B.5	Characteristics of the box model for the spectral absorption coefficient of the gas phase. . . . .	110
C.1	Parameters for the polynomial approximation for specific heat $\bar{c}_p$ . Source is [18]. . . . .	112
C.2	Specific enthalpies of formation at $T_{\text{ref}} = 298 \text{ K}$ . Source is [18].	113
C.3	Collision diameters used for the determination of $k$ and $\mu$ for all relevant gaseous species [28]. . . . .	114
D.1	Experimentally determined kinetic parameters for the rate law (Eq. D.2). . . . .	115
E.1	Reactor performance at design point, $T_{\text{out}} = 1,870 \text{ K}$ . . . . .	122
E.2	Reactor performance at equinox, 9:00, $T_{\text{out}} = 1,870 \text{ K}$ . . . . .	123

# Bibliography

- [1] Mpdb 5.50. Jahm Software, Inc., North Reading, PA, USA, 1999.
- [2] S. Abanades and G. Flamant. Solar hydrogen production from the thermal splitting of methane in a high temperature solar chemical reactor. *Sol. Energy*, 80:1321–1332, 2006.
- [3] S. Abanades and G. Flamant. Experimental study and modeling of a high-temperature solar chemical reactor for hydrogen production from methane cracking. *Int J. Hydrogen Energy*, 32:1508–1515, 2007.
- [4] S. Abanades and G. Flamant. Hydrogen production from solar thermal dissociation of methane in a high-temperature fluid-wall reactor. *Chem Eng. Process.*, 47:490–498, 2008.
- [5] M. Abdelrahman, P. Fumeaux, and P. Suter. Study of solid-gas suspensions used for direct absorption of concentrated solar radiation. *Sol. Energy*, 22:45–48, 1979.
- [6] R. Adinberg, M. Epstein, and J. Karni. Solar gasification of biomass: A molten salt pyrolysis study. *J. Sol. Energy Eng.*, 126(3):850–857, 2004.
- [7] K. S. Adzerikho, E. F. Nogotov, and V. P. Trofimov. *Radiative Heat Transfer in Two-Phase Media*. CRC Press, Boca Raton, 1993.
- [8] J. Ashok, G. Raju, P. S. Reddy, M. Subrahmanyam, and A. Venugopal. Catalytic decomposition of CH<sub>4</sub> over NiO-Al<sub>2</sub>O<sub>3</sub>-SiO<sub>2</sub> catalysts: influence of catalyst preparation conditions on the production of H<sub>2</sub>. *Int J. Hydrogen Energy*, 33:4809–4818, 2008.

- 
- [9] M. H. Back and R. A. Back. Thermal decomposition and reactions of methane. In L. F. Albright, B. L. Crynes, and W. H. Corcoran, editors, *Pyrolysis: theory and industrial practice*, pages 1–24. Academic Press, New York, 1983.
- [10] Z. Bai, H. Chen, W. Li, and B. Li. Hydrogen production by methane decomposition over coal char. *Int J. Hydrogen Energy*, 31:899–905, 2006.
- [11] I. Barin and G. Platzki. *Thermochemical Data of Pure Substances*. Weinheim, 1995.
- [12] L. Barreto, A. Makihira, and K. Riahi. The hydrogen economy in the 21st century: a sustainable development scenario. *Int J. Hydrogen Energy*, 28:267–284, 2003.
- [13] O. Bautista, F. Méndez, and C. T. no. Theoretical analysis of the direct decomposition of methane gas in a laminar stagnation-point flow: CO<sub>2</sub>-free production of hydrogen. *Int J. Hydrogen Energy*, 33:7419–7426, 2008.
- [14] W. H. Beattie, R. Berjoan, and J.-P. Coutures. High-temperature solar pyrolysis of coal. *Solar Energy*, 31(2):137 – 143, 1983.
- [15] A. Belghit, M. Daguinet, and A. Reddy. Heat and mass transfer in a high temperature packed moving bed subjected to an external radiative source. *Chemical Engineering Science*, 55:3967–3978, 2000.
- [16] A. Belghit and S. E. Issami. Hydrogen production by steam-gasification of coal in gas-solid moving bed using nuclear heat. *Energy Convers. Manage.*, 42:81–99, 2001.
- [17] R. Bertocchi, J. Karni, and A. Kribus. Experimental evaluation of a non-isothermal high temperature solar particle receiver. *Energy*, 29:687–700, 2004.
- [18] M. Binnewies and E. Milke. *Thermochemical Data of Elements and Compounds*. Wiley, 2<sup>nd</sup> edition, 2002.

- 
- [19] C. F. Bohren and D. R. Huffman. *Absorption and Scattering of Light by Small Particles*. John Wiley & Sons, New York, 1983.
- [20] T. C. Bond and R. W. Bergstrom. Light absorption by carbonaceous particles: An investigative review. *Aerosol Sci. Technol.*, 40:27–67, 2006.
- [21] BP. Statistical Review of World Energy June 2010. <http://bp.com/statistical>.
- [22] H.-G. Brocksiepe. Charcoal. In *Ullmanns Encyclopedia of Industrial Chemistry*. Wiley-VCH, Weinheim, 2005.
- [23] R. Buck, T. Bräuning, T. Denk, M. Pfänder, P. Schwarzbözl, and F. Tellez. Solar-hybrid gas turbine-based power tower systems (RE-FOS). *J. Sol. Energy Eng.*, 124:2–9, 2002.
- [24] C. Caliot, S. Abanades, A. Soufiani, and G. Flamant. Effects of non-gray thermal radiation on the heating of a methane laminar flow at high temperature. *Fuel*, 88:617–624, 2009.
- [25] W. C. Chueh and S. M. Haile. A thermochemical study of ceria: exploiting an old material for new modes of energy conversion and CO<sub>2</sub> mitigation. *Phil. Trans. R. Soc. A*, 368:3269–3294, 2010.
- [26] S. W. Churchill and H. H. S. Chu. Correlating equations for laminar and turbulent free convection from a vertical plate. *Int. J. Heat Mass Transfer*, 18:1323–1329, 1975.
- [27] A. F. Cunha, J. J. M. Órfão, and J. L. Figueiredo. Methane decomposition on Ni-Cu alloyed Raney-type catalysts. *Int J. Hydrogen Energy*, 34:4763–4772, 2009.
- [28] E. L. Cussler. *Diffusion: Mass Transfer in Fluid Systems*. Cambridge University Press, 2<sup>nd</sup> edition, 1997.
- [29] J. K. Dahl, K. J. Buechler, R. Finley, T. Stanislaus, A. W. Weimer, A. Lewandowski, C. Bingham, A. Smeets, and A. Schneider. Rapid solar-thermal dissociation of natural gas in an aerosol flow reactor. *Energy*, 29:715–725, 2004.

- 
- [30] J. K. Dahl, K. J. Buechler, A. W. Weimer, A. Lewandowski, and C. Bingham. Solar-thermal dissociation of methane in a fluid-wall aerosol flow reactor. *Int J. Hydrogen Energy*, 29:725–736, 2004.
- [31] J. K. Dahl, A. Weimer, A. Lewandowski, C. Bingham, F. Bruetsch, and A. Steinfeld. Dry reforming of methane using a solar-thermal aerosol flow reactor. *Ind. Eng. Chem. Res.*, 43:5489–5495, 2004.
- [32] W. H. Dalzell and A. F. Sarofim. Optical constants of soot and their application to heat-flux calculations. *J. Heat Transfer*, 91:614–618, 1968.
- [33] C. di Blasi. Heat, momentum and mass transport through a shrinking biomass particle exposed to thermal radiation. *Chemical Engineering Science*, 51:1121–1132, 1996.
- [34] A. L. Dicks. Hydrogen generation from natural gas for the fuel cell systems of tomorrow. *J. Power Sources*, 61:113–124, 1996.
- [35] L. A. Dombrovsky. *Radiation Heat Transfer in Disperse Systems*. Begell House, New York, 1996.
- [36] L. A. Dombrovsky, L. Schunk, W. Lipiński, and A. Steinfeld. An ablation model for the thermal decomposition of porous zinc oxide layer heated by concentrated solar radiation. *Int. J. Heat Mass Transfer*, 52:2444–2452, 2009.
- [37] A. Domínguez, B. Fidalgo, Y. Fernández, J. J. Pis, and J. A. Menéndez. Microwave-assisted catalytic decomposition of methane over activated carbon for CO<sub>2</sub>-free hydrogen production. *Int J. Hydrogen Energy*, 32:4792–4799, 2007.
- [38] A. M. Dunker, S. Kumar, and P. A. Mulawa. Production of hydrogen by thermal decomposition of methane in a fluidized-bed reactor - effects of catalyst, temperature, and residence time. *Int J. Hydrogen Energy*, 31:473–484, 2006.
- [39] M. A. Ermakova, D. Y. Ermakov, and G. G. Kuvshinov. Effective catalysts for direct cracking of methane to produce hydrogen and



- filamentous carbon: part I. Nickel catalysts. *Appl. Catal., A*, 201:61–70, 2008.
- [40] G. Evans, H. Houf, R. Greif, and C. Crowe. Gas-particle flow within a high-temperature solar cavity receiver including radiation heat transfer. *J. Sol. Energy Eng.*, 109:134–142, 1987.
- [41] J. T. Farmer and J. R. Howell. in: J.P. Hartnett and T.F. Irvine (eds.), Comparison of monte carlo strategies for radiative transfer in participating media. *Adv. Heat Transfer*, 31:333–429, 1998.
- [42] J. Ferziger and M. Perić. *Computational Methods for Fluid Dynamics*. Springer, Berlin, 3<sup>rd</sup> edition, 2002.
- [43] E. A. Fletcher. Solarthermal processing: A review. *J. Sol. Energy Eng.*, 123:63–74, 2001.
- [44] L. Fulcheri and Y. Schwob. From methane to hydrogen, carbon black and water. *Int J. Hydrogen Energy*, 20:197–202, 1995.
- [45] B. Gaudernack and S. Lynam. Hydrogen from natural gas without release of CO<sub>2</sub> to the atmosphere. *Int J. Hydrogen Energy*, 23:1087–1093, 1998.
- [46] D. Gregg, R. Taylor, J. Campbell, J. Taylor, and A. Cotton. Solar gasification of coal, activated carbon, coke and coal and biomass mixtures. *Sol. Energy*, 25(4):353 – 364, 1980.
- [47] D. W. Gregg, W. R. Aiman, H. H. Otsuki, and C. B. Thorsness. Solar coal gasification. *Sol. Energy*, 24:313–321, 1980.
- [48] M. Halmann, A. Frei, and A. Steinfeld. Carbothermal reduction of alumina: thermochemical equilibrium calculations and experimental investigation. *Energy*, 32:2420–2427, 2007.
- [49] P. Haueter, T. Seitz, and A. Steinfeld. A new high-flux solar furnace for high-temperature thermochemical research. *Ind. Eng. Chem. Res.*, 121:77–80, 1999.
- [50] Heraeus Quarzglas. [heraeus-quarzglas.de/en/quarzglas/opticalproperties/Optical-properties.aspx](http://heraeus-quarzglas.de/en/quarzglas/opticalproperties/Optical-properties.aspx), June 2010.

- 
- [51] C. Hirsch. *Numerical Computation of Internal and External Flows, Volume 1, Fundamentals of Numerical Discretization*. John Wiley & Sons, Chichester, 1997.
- [52] D. Hirsch. *Hydrogen Production by the Solar Thermal Decomposition of Natural Gas Using a Vortex-Flow Solar Reactor*. PhD thesis, Swiss Federal Institute of Technology, Zurich, 2003. Diss. ETH No. 15212.
- [53] D. Hirsch, M. Epstein, and A. Steinfeld. The solar thermal decarbonization of natural gas. *Int J. Hydrogen Energy*, 26:1023–1033, 2001.
- [54] D. Hirsch and A. Steinfeld. Radiative transfer in a solar chemical reactor for the co-production of hydrogen and carbon by thermal decomposition of methane. *Chemical Engineering Science*, 59:5771–5778, 2004.
- [55] D. Hirsch and A. Steinfeld. Solar hydrogen production by thermal decomposition of natural gas using a vortex-flow reactor. *Int J. Hydrogen Energy*, 29:47–55, 2004.
- [56] D. Hirsch, P. von Zedtwitz, T. Osinga, J. Kinamore, and A. Steinfeld. A new 75 kW high-flux solar simulator for high-temperature thermal and thermochemical research. *J. Sol. Energy Eng.*, 125:117–120, 2003.
- [57] A. Holmen, O. Olsvik, and O. A. Rokstad. Pyrolysis of natural gas: chemistry and process concepts. *Fuel Process. Technol.*, 42:249–267, 1995.
- [58] F. P. Incropera and D. P. DeWitt. *Fundamentals of Heat and Mass Transfer*. John Wiley & Sons, 5<sup>th</sup> edition, 2002.
- [59] International Energy Agency. Key World Energy Statistics 2009. <http://www.iea.org/statistics>.
- [60] J. Karni, A. Kribus, B. Ostrach, and E. Kochavi. A high-pressure window for volumetric solar receivers. *J. Sol. Energy Eng.*, 120:101–107, 1998.

- [61] J. Karni, A. Kribus, R. Rubin, and P. Doron. The 'porcupine': a novel high-flux absorber for volumetric solar receivers. *J. Sol. Energy Eng.*, 120:85–95, 1998.
- [62] M. Kaviany. *Principles of heat transfer in porous media*. Springer, New York, 2<sup>nd</sup> edition, 1995.
- [63] R. A. Kerr. Global warming is changing the world. *Science*, 316:188–190, 2007.
- [64] M. H. Kim, E. K. Lee, J. H. Jun, S. J. Kong, G. Y. Han, B. K. Lee, T.-J. Lee, and K. J. Yoon. Hydrogen production by catalytic decomposition of methane over activated carbons: kinetic study. *Int J. Hydrogen Energy*, 29:187–193, 2004.
- [65] H. H. Klein, J. Karni, R. Ben-Zvi, and R. Bertocchi. Heat transfer in a directly irradiated solar receiver/reactor for solid-gas reactions. *Sol. Energy*, 81:1227–1239, 2007.
- [66] T. Kodama. High-temperature solar chemistry for converting solar heat to chemical fuels. *Prog. Energy Combust. Sci.*, 29:567–597, 2003.
- [67] T. Kodama, Y. Kondoh, T. Tamagawa, A. Funatoh, K.-I. Shimizu, and Y. Kitayama. Fluidized bed coal gasification with CO<sub>2</sub> under direct irradiation with concentrated visible light. *Energy Fuels*, 16:1264–1270, 2002.
- [68] T. Kodama, T. Shimizu, M. Satoh, M. Nakata, and K.-I. Shimizu. Stepwise production of CO-rich syngas and hydrogen via solar methane reforming by using a Ni(II)-ferrite redox system. *Sol. Energy*, 73:363–374, 2002.
- [69] A. Kogan, M. Kogan, and S. Barak. Production of hydrogen and carbon by solar thermal methane splitting. III. Fluidization, entrainment and seeding powder particles into a volumetric solar receiver. *Int J. Hydrogen Energy*, 30:35–43, 2005.
- [70] A. Konieczna, K. Mondala, T. Wiltowska, and P. Dydo. Catalyst development for thermocatalytic decomposition of methane to hydrogen. *Int J. Hydrogen Energy*, 33:264–272, 2008.

- 
- [71] S. Kräupl and A. Steinfeld. Operational performance of a 5-kW solar chemical reactor for the co-production of zinc and syngas. *J. Sol. Energy Eng.*, 125:124–126, 2003.
- [72] S. Kräupl and A. Steinfeld. Monte Carlo radiative transfer modeling of a solar chemical reactor for the co-production of zinc and syngas. *J. Sol. Energy Eng.*, 127:102–108, 2005.
- [73] A. Kribus. Optical performance of conical windows for concentrated solar radiation. *J. Sol. Energy Eng.*, 116:47–52, 1994.
- [74] A. Kribus, M. Huleihil, A. Timinger, and R. Ben-Mair. Performance of a rectangular secondary concentrator with an asymmetric heliostat field. *Sol. Energy*, 69:139–151, 2000.
- [75] S. Krzyżyński and M. Kozłowski. Activated carbons as catalysts for hydrogen production via methane decomposition. *Int J. Hydrogen Energy*, 33:6172–6177, 2008.
- [76] G. G. Kuvshinov, Y. I. Mogilnykh, D. G. Kuvshinov, V. I. Zaikovskii, and L. B. Avdeeva. Peculiarities of filamentous carbon formation in methane decomposition on Ni-containing catalysts. *Carbon*, 36:87–97, 1998.
- [77] M. J. L’azaro, J. L. Pinilla, I. Suelves, and R. Moliner. Study of the deactivation mechanism of carbon blacks used in methane decomposition. *Int J. Hydrogen Energy*, 33:4104–4111, 2008.
- [78] J. Lédé. Solar thermochemical conversion of biomass. *Sol. Energy*, 65:3–13, 1999.
- [79] E. K. Lee, S. Y. Lee, B. Y. Han, B. K. Lee, T. J. Lee, J. H. Jun, and K. J. Yoon. Catalytic decomposition of methane over carbon blacks for CO<sub>2</sub>-free hydrogen production. *Carbon*, 42:2641–2648, 2004.
- [80] O. Levenspiel. *Chemical Reaction Engineering*. Wiley, New York, 3<sup>rd</sup> edition, 1999.
- [81] R. Levitan, H. Rosin, and M. Levy. Chemical reactions in a solar furnace - direct heating of the reactor in a tubular receiver. *Sol. Energy*, 42:267–272, 1989.

- 
- [82] S. Lin and E. Sparrow. Radiant interchange among curved specularly reflecting surfaces - application to cylindrical and conical cavities. *J. Heat Transfer*, 87:299–307, 1965.
- [83] W. Lipiński and A. Steinfeld. Heterogeneous thermochemical decomposition under direct irradiation. *Int. J. Heat Mass Transfer*, 47:1907–1916, 2004.
- [84] W. Lipiński and A. Steinfeld. Transient radiative heat transfer within a suspension of coal particles undergoing steam gasification. *Heat Mass Transfer*, 41:1021–1032, 2005.
- [85] W. Lipiński, A. Zraggen, and A. Steinfeld. Transient radiation heat transfer within a nongray nonisothermal absorbing-emitting-scattering suspension of reacting particles undergoing shrinkage. *Numer. Heat Transfer, Part B*, 47:443–475, 2005.
- [86] G. Maag, W. Lipiński, and A. Steinfeld. Particle-gas reacting flow under concentrated solar irradiation. *Int. J. Heat Mass Transfer*, 52:4997–5004, 2009.
- [87] G. Maag, S. Rodat, G. Flamant, and A. Steinfeld. Heat transfer model and scale-up of an entrained-flow solar reactor for the thermal decomposition of methane. *Int J. Hydrogen Energy*, 35:13232–13241, 2010.
- [88] G. Maag, G. Zanganeh, and A. Steinfeld. Solar thermal cracking of methane in a particle-flow reactor for the co-production of hydrogen and carbon. *Int J. Hydrogen Energy*, 34:7676–7685, 2009.
- [89] A. Malaika and M. Kozłowski. Influence of ethylene on carbon-catalysed decomposition of methane. *Int J. Hydrogen Energy*, 33:2600–2605, 2009.
- [90] J. Matsunami, S. Yoshida, O. Yokota, M. Nezuka, M. Tsuji, and Y. Tamaura. Gasification of waste tyre and plastic (pet) by solar thermochemical process for solar energy utilization. *Sol. Energy*, 65:21–23, 1999.

- 
- [91] T. Melchior, C. Perkins, P. Lichty, A. W. Weimer, and A. Steinfeld. Solar-driven biochar gasification in a particle-flow reactor. *Chem Eng. Process.*, 48:1279–1287, 2009.
- [92] T. Melchior, C. Perkins, A. W. Weimer, and A. Steinfeld. A cavity-receiver containing a tubular absorber for high-temperature thermochemical processing using concentrated solar energy. *Int. J. Therm. Sci.*, 47:1496–1503, 2008.
- [93] T. Melchior and A. Steinfeld. Radiative transfer within a cylindrical cavity with diffusely/specularly reflecting inner walls containing an array of tubular absorbers. *J. Sol. Energy Eng.*, 130:021013, 2008.
- [94] S. C. Mishra, M. Steven, S. Nemoda, P. Talukdar, D. Trimis, and F. Durst. Heat transfer analysis of a two-dimensional rectangular porous radiant burner. *Int. Comm. Heat Mass Transfer*, 33:467–474, 2005.
- [95] M. F. Modest, editor. *Radiative Heat Transfer*. Academic Press, New York, 2<sup>nd</sup> edition, 2003.
- [96] R. Moliner, I. Suelves, M. J. Lázaro, and O. Moreno. Thermocatalytic decomposition of methane over activated carbons: influence of textural properties and surface chemistry. *Int J. Hydrogen Energy*, 30:293–300, 2005.
- [97] B. Monnerat, L. Kiwi-Minsker, and A. Renken. Hydrogen production by catalytic cracking of methane over nickel gauze under periodic reactor operation. *Chemical Engineering Science*, 356:633–639, 2001.
- [98] R. Müller, W. Lipiński, and A. Steinfeld. Transient heat transfer in a directly irradiated solar chemical reactor for the thermal dissociation of ZnO. *Appl. Therm. Eng.*, 28:524–531, 2008.
- [99] R. Müller, P. von Zedtwitz, A. Wokaun, and A. Steinfeld. Kinetic investigation on steam gasification of charcoal under direct high-flux irradiation. *Chemical Engineering Science*, 58:5111–5119, 2003.
- [100] N. Muradov, Z. Chen, and F. Smith. Fossil hydrogen with reduced CO<sub>2</sub> emission: Modeling thermocatalytic decomposition of methane

- in a fluidized bed of carbon particles. *Int J. Hydrogen Energy*, 30:1149–1158, 2005.
- [101] N. Muradov, F. Smith, and A. T-Raissi. Catalytic activity of carbons for methane decomposition reaction. *Catal. Today*, 102-103:225–233, 2005.
- [102] N. Z. Muradov. How to produce hydrogen from fossil fuels without CO<sub>2</sub> emission. *Int J. Hydrogen Energy*, 18(3):211–215, 1993.
- [103] J. P. Murray and E. A. Fletcher. Reaction of steam with cellulose in a fluidized bed using concentrated sunlight. *Energy*, 19(10):1083 – 1098, 1994.
- [104] K. Nakagawa, M. Nishitani-Gamo, and T. Ando. hydrogen production from methane for fuel cell using oxidized diamond-supported catalysts. *Int J. Hydrogen Energy*, 30:201–207, 2005.
- [105] H. Netz. *Verbrennung und Gasgewinnung bei Festbrennstoffen*. Resch, Gräfeling/München, 1982.
- [106] T. Osinga, G. Olalde, and A. Steinfeld. Solar carbothermal reduction of ZnO: shrinking packed-bed reactor modeling and experimental validation. *Ind. Eng. Chem. Res.*, 43:7981–7988, 2004.
- [107] N. Ozalp, a Kogan, and M. Epstein. Solar decomposition of fossil fuels as an option for sustainability. *Int J. Hydrogen Energy*, 34:710–720, 2009.
- [108] S. V. Patankar. *Numerical Heat Transfer and Fluid Flow*. Hemisphere, 1980.
- [109] N. Piatkowski and A. Steinfeld. Solar-driven coal gasification in a thermally irradiated packed-bed reactor. *Energy Fuels*, 22:2043–2052, 2008.
- [110] N. Piatkowski, C. Wieckert, and A. Steinfeld. Experimental investigation of a packed-bed solar reactor for the steam-gasification of carbonaceous feedstocks. *Fuel Process. Technol.*, 90(3):360 – 366, 2009.

- 
- [111] J. L. Pinilla, R. Moliner, I. Suelves, M. J. Lázaro, Y. Echevoyen, and J. M. Palacios. Production of hydrogen and carbon nanofibers by thermal decomposition of methane using metal catalysts in a fluidized-bed reactor. *Int J. Hydrogen Energy*, 32:4821–4829, 2007.
- [112] T. Pregger, D. Graf, W. Krewitt, C. Sattler, M. Roeb, and S. Möller. Prospects of solar thermal hydrogen production processes. *Int J. Hydrogen Energy*, 034:4256–4267, 2009.
- [113] Quartz Scientific, Inc. [quartzscientific.thomasnet.com/viewitems/discs-and-plates/ground-polished-discs](http://quartzscientific.thomasnet.com/viewitems/discs-and-plates/ground-polished-discs), June 2010.
- [114] S. Rodat, S. Abanades, J. Couilé, and G. Flamant. Kinetic modelling of methane decomposition in a tubular solar reactor. *Chem. Eng. J.*, 146:120–127, 2009.
- [115] S. Rodat, S. Abanades, and G. Flamant. Experimental evaluation of indirect heating tubular reactors for solar methane pyrolysis. *Int. J. Chem. Reactor Eng.*, 8:A25, 2010.
- [116] S. Rodat, S. Abanades, J.-L. Sans, and G. Flamant. Hydrogen production from solar thermal dissociation of natural gas: development of a 10 kw solar chemical reactor prototype. *Sol. Energy*, 83:1599–1610, 2009.
- [117] M. Röger, M. Pfänder, and R. Buck. Multiple air-jet window cooling for high-temperature pressurized volumetric receivers: testing, evaluation, and modeling. *J. Sol. Energy Eng.*, 128:265–274, 2006.
- [118] M. Röger, C. Rickers, R. Uhlig, F. Neumann, and C. Polenzky. Infrared-reflective coating on fused silica for a solar high-temperature receiver. *J. Sol. Energy Eng.*, 131:021004, 2009.
- [119] J. M. Roscoe and M. J. Thompson. Thermal decomposition of methane: autocatalysis. *Int J. Chem. Kinet.*, 17:967–990, 1985.
- [120] D. P. Ross, H.-M. Yan, Z. Zhong, and D.-K. Zhang. A non-isothermal model of a bubbling fluidized-bed coal gasifier. *Fuel*, 84:1469–1481, 2005.



- [121] J. R. Rostrup-Nielsen. New aspects of syngas production and use. *Catal. Today*, 63:159–164, 2000.
- [122] L. S. Rothman, D. Jacquemart, A. Barbe, D. Chris Benner, M. Birk, L. R. Brown, M. R. Carleer, C. Chakerian, Jr., K. Chance, L. H. Coudert, V. Dana, V. M. Devi, J.-M. Flaud, R. R. Gamache, A. Goldman, J.-M. Hartmann, K. W. Jucks, A. G. Maki, J.-Y. mandin, S. T. Massie, J. Orphal, A. Perrin, C. P. Rinsland, M. A. H. Smith, J. Tennyson, R. N. Tolchenov, R. A. Toth, J. Vander Auwera, P. Varanasi, and G. Wagner. The HITRAN 2004 molecular spectroscopic database. *J. Quant. Spectrosc. Radiat. Transfer*, 96:139–204, 2005.
- [123] L. S. Rothman, C. P. Rinsland, A. Goldman, S. T. Massie, D. P. Edwards, J.-M. Flaud, A. Perrin, C. Camy-Peyret, V. Dana, J.-Y. Mandin, J. Schroeder, A. McCann, R. R. Gamache, R. B. Wattson, K. Yoshino, K. V. Chance, K. W. Jucks, L. R. Brown, V. Nemtchinov, and P. Varanasi. The HITRAN molecular spectroscopic database and HAWKS (HITRAN atmospheric workstation): 1996 edition. *J. Quant. Spectrosc. Radiat. Transfer*, 60(5):665–710, 1998.
- [124] B. H. Ryu, S. Y. Lee, D. H. Lee, G. Y. Han, T. J. Lee, and K. J. Yoon. Catalytic characteristics of various rubber-reinforcing carbon blacks in decomposition of methane for hydrogen production. *Catal. Today*, 123:303–309, 2007.
- [125] Saint-Gobain Crystals. Properties and benefits of sapphire: A quick reference guide, [www.photonic.saint-gobain.com/uploadedFiles/SGphotonic/Documents/sapphire-material-products-properties.pdf](http://www.photonic.saint-gobain.com/uploadedFiles/SGphotonic/Documents/sapphire-material-products-properties.pdf), June 2010.
- [126] L. O. Schunk, P. Haeberling, S. Wepf, D. Wuillemin, A. Meier, and A. Steinfeld. A receiver-reactor for the solar thermal dissociation of zinc oxide. *J. Sol. Energy Eng.*, 130:021009, 2008.
- [127] D. P. Serrano, J. A. Botas, and R. Guil-Lopez. H<sub>2</sub> production from methane pyrolysis over commercial carbon catalysts: kinetic and deactivation study. *Int J. Hydrogen Energy*, 34:4488–4494, 2009.

- 
- [128] N. Shah, D. Panjala, and G. P. Huffmann. Hydrogen production by catalytic decomposition of methane. *Energy Fuels*, 15:1528–1534, 2001.
- [129] R. K. Shah and A. L. London. *Laminar Flow Forced Convection in Ducts*. Academic Press, New York, 1987.
- [130] R. Siegel. Net radiation method for enclosure systems involving partially transparent walls. Technical Report TN D-7384, NASA, 1973.
- [131] R. Siegel and J. R. Howell. *Thermal Radiation Heat Transfer*. Hemisphere Publishing Corporation, Washington D.C., 3<sup>rd</sup> edition, 1992.
- [132] R. Siegel and J. R. Howell. *Thermal Radiation Heat Transfer*. Taylor & Francis, New York, 4<sup>th</sup> edition, 2002.
- [133] R. J. Silbey, R. A. Alberty, and M. G. Bawendi. *Physical Chemistry*. John Wiley & Sons, Hoboken, NJ, 4<sup>rd</sup> edition, 2005.
- [134] SOLHYCARB Project. Final Report (EU project, SESCT2006-19770), 2010.
- [135] B. C. H. Steele and A. Heinzl. Materials for fuel-cell technologies. *Nature*, 414:345–352, 2001.
- [136] M. Steinberg. Fossil fuel decarbonization technology for mitigating global warming. *Int J. Hydrogen Energy*, 24:771–777, 1999.
- [137] A. Steinfeld. Apparent absorptance for diffusely and specularly reflecting spherical cavities. *Int. J. Heat Mass Transfer*, 34:1895–1897, 1991.
- [138] A. Steinfeld. Solar hydrogen production via a two-step water-splitting thermochemical cycle based on zn/zno redox reactions. *Int J. Hydrogen Energy*, 27:611–619, 2002.
- [139] A. Steinfeld. Solar thermochemical production of hydrogen - a review. *Sol. Energy*, 78:603–615, 2005.
- [140] A. Steinfeld, P. Kuhn, A. Reller, R. Palumbo, J. Murray, and Y. Tamaura. Solar processed metals as clean energy carriers and water-splitters. *Int J. Hydrogen Energy*, 23:767–774, 1998.

- [141] A. Steinfeld and M. Schubnell. Optimum aperture size and operating temperature of a solar cavity-receiver. *Sol. Energy*, 50:19–25, 1993.
- [142] I. Suelves, M. J. Lázaro, R. Moliner, B. M. Corbella, and J. M. Palacios. Hydrogen production by thermo catalytic decomposition of methane on Ni-based catalysts: influence of operating conditions on catalyst deactivation and carbon characteristics. *Int J. Hydrogen Energy*, 30:1555–1567, 2005.
- [143] J. Taine and A. Soufiani. in: J.P. Hartnett and T.F. Irvine (eds.): Gas IR radiative properties: From spectroscopic data to approximate models. *Adv. Heat Transfer*, 33:295–414, 1999.
- [144] C. L. Tien and B. L. Drohler. Thermal radiation in particulate media with dependent and independent scattering. *Annu. Rev. Numer. Fluid Mech. Heat Transfer*, 1:1–32, 1987.
- [145] T. W. Tong, M. M. Abou-Ellail, and Y. Li. A discrete ordinate thermal radiation model for reacting flows in porous burners. In D. Lemonnier, N. Seluk, and P. Lybaert, editors, *Eurotherm Seminar 78 on Computational Thermal Radiation in Participating Media II*, pages 379–388, Poitiers, 2006.
- [146] Y. S. Touloukian and D. P. DeWitt. *Thermophysical Properties of Matter, Thermal Radiative Properties: Nonmetallic Solids*, volume 8. IFI Plenum, New York, Washington, 1972.
- [147] F. Trombe and A. L. P. Vinh. Thousand kW solar furnace, built by the national center of scientific research in Odeillo (France). *Sol. Energy*, 15:57–61, 1973.
- [148] D. Trommer, D. Hirsch, and A. Steinfeld. Kinetic investigation of the thermal decomposition of CH<sub>4</sub> by direct irradiation of a vortex-flow laden with carbon particles. *Int J. Hydrogen Energy*, 29:627–633, 2004.
- [149] J. A. Turner. A realizable renewable energy future. *Science*, 285:687–689, 1999.

- [150] A. Venugopal, S. Naveen Kumar, J. Ashok, D. Hari Prasad, V. Durga Kumari, and K. B. S. Prasad. Hydrogen production by catalytic decomposition of methane over Ni/SiO<sub>2</sub>. *Int J. Hydrogen Energy*, 32:1782–1788, 2007.
- [151] P. von Zedtwitz, W. Lipiński, and A. Steinfeld. Numerical and experimental study of gasparticle radiative heat exchange in a fluidized-bed reactor for steam-gasification of coal. *Chemical Engineering Science*, 62:599–607, 2007.
- [152] P. von Zedtwitz and A. Steinfeld. The solar thermal gasification of coal – energy conversion efficiency and CO<sub>2</sub> mitigation potential. *Energy*, 28:441–456, 2003.
- [153] W. Haldenwanger Technische Keramik GmbH & Co.KG. HALSIC-R/-RX/-I/-S/ silicon carbide special materials catalogue, www.haldenwanger.de, 2007.
- [154] H. Watanabe and M. Otaka. Numerical simulation of coal gasification in entrained flow coal gasifier. *Fuel*, 85:1935–1943, 2006.
- [155] W. T. Welford and R. Winston. *High Collection Nonimaging Optics*. Academic Press, San Diego, 1989.
- [156] R. V. Wheeler and W. L. Wood. The pyrolysis of methane. *Fuel*, 7:535–539, 1928.
- [157] C. Wieckert, A. Meier, and A. Steinfeld. Indirectly irradiated solar receiver-reactors for high-temperature thermochemical processes. *J. Sol. Energy Eng.*, 125:120–123, 2003.
- [158] D. J. Wilhelm, D. R. Simbeck, A. D. Karp, and R. L. Dickenson. Syngas production for gas-to-liquids applications: technologies, issues and outlook. *Fuel Process. Technol.*, 71:139, 2001.
- [159] A. Wörner and R. Tamme. CO<sub>2</sub> reforming of methane in a solar driven volumetric receiver-reactor. *Catal. Today*, 46:165–174, 1998.
- [160] I. G. Wright and T. B. Gibbons. Recent developments in gas turbine materials and technology and their implications for syngas firing. *Int J. Hydrogen Energy*, 32:3610–3621, 2007.

- 
- [161] M. Wullenkord. Personal communication, July 2009.
- [162] W.-J. Yang, H. Taniguchi, and K. Kudo. *in: J.P. Hartnett and T.F. Irvine (Eds.): Radiative Heat Transfer by the Monte Carlo Method*, volume 27, pages 3–215. Academic Press, San Diego, 1995.
- [163] A. Z'Graggen, P. Haueter, G. Maag, A. Vidal, M. Romero, and A. Steinfeld. Hydrogen production by steam-gasification of petroleum coke using concentrated solar power - III Reactor experimentation with slurry feeding. *Int J. Hydrogen Energy*, 32:992–996, 2007.
- [164] A. Z'Graggen, P. Haueter, D. Trommer, M. Romero, J. C. de Jesus, and A. Steinfeld. Hydrogen production by steam-gasification of petroleum coke using concentrated solar power - II Reactor design, testing, and modeling. *Int J. Hydrogen Energy*, 31:797–811, 2006.
- [165] A. Z'Graggen and A. Steinfeld. Radiative exchange within a two-cavity configuration with a spectrally selective window. *J. Sol. Energy Eng.*, 126(2):819–822, 2004.
- [166] A. Z'Graggen and A. Steinfeld. A two-phase reactor model for the steam-gasification of carbonaceous materials under concentrated thermal radiation. *Chem Eng. Process.*, 47:655–662, 2008.
- [167] T. Zhang and M. D. Amiridis. Hydrogen production via the direct cracking of methane over silica-supported nickel catalysts. *Appl. Catal., A*, 167:161–172, 1998.



# Curriculum vitae

Name: Gilles Maag

Nationality: Swiss

Citizen of: Herrliberg (ZH)

Date of birth: September 16, 1981

Place of birth: Glarus

2006-2010      Doctoral studies at the Professorship in Renewable Energy Carriers, ETH Zurich; supervision: Prof. Dr. Aldo Steinfeld

2001-2006      Diploma studies in Mechanical Engineering at ETH Zurich (Dipl.-Ing. ETH); majors in Renewable Energy Carriers and Internal Combustion Engines

1997-2001      Maturità Federale (indirizzo scientifico), Liceo Cantonale Lugano 1, Lugano (TI)

## List of publications

### Refereed journal papers

G. Maag, C. Falter, and A. Steinfeld. Temperature of a quartz/sapphire window in a solar cavity-receiver. *J. Sol. Energy Eng.*, 133:014501-1, 2011.

G. Maag, A. Steinfeld. Design of a 10 MW particle-flow reactor for syngas production by steam-gasification of carbonaceous feedstock using concentrated solar energy. *Energy Fuels*, 24:6540-6547, 2010.

G. Maag, S. Rodat, G. Flamant, and A. Steinfeld. Heat transfer model and scale-up of an entrained-flow solar reactor for the thermal decomposition of methane. *Int. J. Hydrogen Energy*, 35:13232-13241, 2010.

G. Maag, G. Zanganeh, and A. Steinfeld. Solar thermal cracking of methane in a particle-flow reactor for the co-production of hydrogen and carbon. *Int. J. Hydrogen Energy*, 34:7676-7685, 2009.

G. Maag, W. Lipiński, and A. Steinfeld. Particle-gas reacting flow under concentrated solar irradiation. *Int. J. Heat Mass Transfer*, 52:4997-5004, 2009.

A. Z'Graggen, P. Haueter, G. Maag, M. Romero, and A. Steinfeld. Hydrogen production by steam-gasification of petroleum coke using concentrated solar power - IV Reactor experimentation with vacuum residue. *Int. J. Hydrogen Energy*, 33:679-684, 2008.

A. Z'Graggen, P. Haueter, G. Maag, A. Vidal, M. Romero, and A. Steinfeld. Hydrogen production by steam-gasification of petroleum coke using concentrated solar power - III Reactor experimentation with slurry feeding. *Int. J. Hydrogen Energy*, 32:992-996, 2007.



**Refereed conference proceedings papers**

G. Maag, F. J. Gutiérrez, and A. Steinfeld. Effect of laden particles on the thermal decomposition of methane using a particle-flow solar reactor. In *Proceedings of the 14<sup>th</sup> biennial CSP SolarPaces conference*, Las Vegas, NV, USA, Mar 2008.

G. Maag, F. J. Gutiérrez, W. Lipiński, and A. Steinfeld. Thermal dissociation of CH<sub>4</sub> using a particle-flow chemical reactor exposed to concentrated solar radiation. In *Proceedings of the 2008 ASME International Mechanical Engineers Congress and Exhibition (IMECE)*, Boston, MA, USA, Oct-Nov 2008.